

---

# Absolute phase control of intense few-cycle pulses and steering the atomic-scale motion of electrons

Aart Verhoef

---



München 2006



---

# **Absolute phase control of intense few-cycle pulses and steering the atomic-scale motion of electrons**

**Aart Verhoef**

---

Dissertation  
an der Fakultät für Physik  
der Ludwig–Maximilians–Universität  
München

vorgelegt von  
Aart Verhoef  
aus Amsterdam

München, den 21 Dezember 2006

Erstgutachter: Prof. Dr. F. Krausz

Zweitgutachter: Prof. Dr. D. Habs

Tag der mündlichen Prüfung: 22 März 2007



*We often discover what will do,  
by finding out what will not do.  
– Samuel Smiley –*



# Abstract

In the past few years, ultrafast laser technology has developed to such a degree that the phase of a pulse under its envelope is now a meaningful measurable quantity. Many experiments now require the use of pulses with a fixed phase. The reliable production of such pulses, over extended periods of time, is of key importance to many areas of science.

The central theme of this thesis is the generation of intense phase-controlled few-cycle optical pulses and their applications. This thesis reports on substantial improvements made in the generation of carrier-envelope phase-controlled pulses. Measurements performed show the accuracy to which absolute phase can be controlled has been improved to an unprecedented level. Also, the period of time over which such high accuracy measurements could be performed was extended by more than a factor of five, such that carrier-envelope phase-sensitive measurements that take longer than 24 hours without any breaks are now possible.

With these tools at hand, physical processes that take place on sub-femtosecond time scales can be precisely measured, and control over the motion of bound electrons is possible. In this thesis, a report on the first demonstration of the latter is presented: In the dissociation of the  $D_2^+$ -ion, control over the localisation of the remaining electron is demonstrated.



# Zusammenfassung

In den letzten Jahren ist die ultraschnelle Lasertechnologie so weit voran getreten, daß die Phase eines Pulses unter seiner Einhüllende eine bedeutende meßbare Größe geworden ist. Viele Experimenten haben die Verfügbarkeit von Pulsen mit festgestellter Phase als Voraussetzung. Die verlässliche Erzeugung solcher Pulsen über längere Zeitspannen ist deshalb sehr wichtig für viele wissenschaftliche Anwendungen.

Das zentrale Leitmotiv in dieser Dissertation ist die Erzeugung und Anwendung leistungsstarker phasen-kontrollierte Lichtpulsen mit einer Pulsdauer von nur einigen optische Zyklen. In dieser Dissertation wird berichtet über wesentliche Verbesserungen die gemacht wurden an bestehenden Methoden zur reproduzierbare Erzeugung phasenkontrollierter Pulsen. Einerseits leiteten die dazu, daß die Genauigkeit womit der absolute Phase eingestellt werden kann besser als bisher wurde. Andererseits wurde auch die Zeitdauer über die so dies möglich ist mehr als fünf mal verlängert. Erstmals ist es möglich phasen-empfindliche Experimente die eine Meßzeit über 24 Stunden am Stück erfordern.

Mit diesem Werkzeug ist es möglich physikalische Prozesse die stattfinden auf einer Zeitskala kürzer als eine Femtosekunde zu untersuchen, sowohl auch die Bewegung von gebundene Elektronen zu kontrollieren. In dieser Dissertation wird auch darüber berichtet; es wird Kontrolle über die Lokalisierung des verbleibende Elektron bei der Dissoziation des  $D_2^+$ -ions demonstriert.



# Contents

**Abstract** vii

**Introduction** 1

## **1 High power pulse compression into the few-cycle regime** 5

- 1.1 Spectral broadening in a bulk material 5
- 1.2 Spectral broadening in a rare gas filled hollow waveguide 7
  - 1.2.1 Laser system providing 2-mJ, 15-fs pulses 7
  - 1.2.2 Generating 1-mJ, 5-fs pulses 9
  - 1.2.3 Generating 400- $\mu$ J, sub-5-fs pulses 11
- 1.3 Temporal characterisation of few-cycle pulses 13
  - 1.3.1 Second order autocorrelation 13
  - 1.3.2 Third order interferometric autocorrelation 15
  - 1.3.3 High dynamic range third order correlation 16
  - 1.3.4 SPIDER 17
  - 1.3.5 Frequency resolved optical gating – FROG 19
- 1.4 Spatial beam-characterisation 20

## **2 Carrier-envelope phase stabilisation of ultrashort pulses** 23

- 2.1 Carrier-envelope phase stabilisation of oscillators 23
  - 2.1.1 The frequency comb 23
  - 2.1.2 The f-to-2f technique 23
  - 2.1.3 The f-to-zero technique 25
  - 2.1.4 Comparison of the two techniques 25
- 2.2 Carrier-envelope phase of amplified pulses 26
  - 2.2.1 Measurement of the carrier-envelope phase after amplification 26
  - 2.2.2 Compensation of the carrier-envelope phase drift 28
- 2.3 Mini stereo ATI – Absolute phase control 30
  - 2.3.1 Improving the control over the carrier-envelope phase 30
  - 2.3.2 Above-threshold-ionisation 31
  - 2.3.3 The mini stereo ATI apparatus 31
  - 2.3.4 Carrier-envelope phase retrieval 32
  - 2.3.5 Carrier-envelope phase control with the mini stereo ATI 33

## **3 High-harmonic generation with ultrashort pulses** 39

- 3.1 Upscaling the energy of coherent extreme ultraviolet radiation 39

---

3.1.1	Motivation for upscaling the energy of extreme ultraviolet radiation	39
3.1.2	Theoretical considerations	39
3.1.3	Experimental considerations	40
3.1.4	Calibrating and measuring soft-x-ray photon energies	43
3.2	Generation of single attosecond soft-x-ray pulses	44
3.2.1	The optics for single attosecond soft-x-ray pulses	44
3.3	Attosecond time resolved ionisation spectroscopy	45
3.3.1	Auger decay	46
3.3.2	Experimental setup	48
3.3.3	Experimental results and discussion	49
3.3.4	Conclusion	53
<b>4</b>	<b>Angular resolved ionisation with ultrashort pulses</b>	<b>55</b>
4.1	Velocity-map imaging spectroscopy	55
4.1.1	The velocity-map imaging technique	55
4.1.2	The velocity-map imaging spectrometer	56
4.2	Above-threshold-ionisation with few-cycle pulses	56
4.3	Carrier-envelope phase-dependence of ATI	62
4.3.1	Asymmetry maps	63
4.3.2	Simple asymmetry plots	69
4.4	Control of electron localisation in molecular dissociation	70
4.4.1	Experiment	70
4.4.2	Theoretical model	73
	<b>Conclusions and future prospects</b>	<b>79</b>
<b>A</b>	<b>How to stabilise the carrier envelope phase of a laser</b>	<b>81</b>
A.1	Oscillator	81
A.2	Amplifier slow drift compensation	81
A.2.1	The phase stabilisation program	81
A.3	Carrier-envelope phase control with the mini stereo ATI	82
<b>B</b>	<b>Short manual of a Femtopower Compact Pro</b>	<b>85</b>
B.1	Switch on procedure	85
B.1.1	First warm-up phase	85
B.1.2	Second warm-up phase	85
B.2	Shut-down procedure	86
	<b>Acknowledgements</b>	<b>87</b>
	<b>Bibliography</b>	<b>89</b>
	<b>Curriculum Vitae</b>	<b>101</b>



# List of Figures

1	History of laser peak power since the introduction of the laser	2
1.1	Spectral broadening in a bulk medium with 1-mJ, 25-fs pulses	6
1.2	Schematic of 3 stage amplifier system	8
1.3	Focused beam profile of 3 stage amplifier	9
1.4	Spectrum and autocorrelation of 1-mJ, 5-fs pulses	10
1.5	Schematic of 3-kHz 5-fs laser system	12
1.6	Spectrum and autocorrelation of 400- $\mu$ J, sub-5-fs pulses	13
1.7	2nd order autocorrelation of a 4.8-fs Gaussian pulse	14
1.8	Third order interferometric autocorrelation	15
1.9	Third-order high-dynamic-range correlation of 1-mJ, 5-fs pulses	16
1.10	SPIDER interferogram	17
1.11	SPIDER reconstruction	18
1.12	Measured and calculated FROG traces	19
1.13	$M^2$ measurement of 1-mJ, 5-fs beam	21
2.1	Frequency comb and pulse train	24
2.2	F-to-2f interferometer for oscillator phase stabilisation	25
2.3	The f-to-zero technique	26
2.4	Collinear f-to-2f interferometer for carrier-envelope phase detection	27
2.5	Carrier-envelope phase drift after amplification	28
2.6	The two methods for compensating the phase drift compared	29
2.7	Carrier-envelope phase stabilisation of multi-stage amplifiers	30
2.8	Schematic of the mini stereo ATI apparatus	32
2.9	Slow phase drift measured with the mini stereo ATI	33
2.10	Stereo ATI phase measurement of phase-stabilised amplifier	34
2.11	Direct feedback on the amplifier with the mini stereo ATI	35
2.12	Feedback with both f-to-2f interferometer and mini stereo ATI	36
3.1	The three step model	41
3.2	Photograph of a target for harmonic generation	42
3.3	Generated coherent x-rays up to 1.3 keV	43
3.4	Generation of a single attosecond soft-x-ray pulse	44
3.5	X-ray multilayer reflectivities	45
3.6	A single attosecond pulse is reflected off the multilayer mirror	46
3.7	Overview of attosecond pump-probe experiments	47
3.8	The vacuum system for attosecond pump-probe experiments	48
3.9	Detail photographs of the experimental setup	49
3.10	Schematic level diagram for the xenon ionisation experiment	50

---

3.11	Measurement of xenon ionisation dynamics	52
4.1	Graphic representation of the Abel transformation	56
4.2	Experimental setup for the VMI measurements	57
4.3	Argon VMI ATI images	59
4.4	Krypton VMI ATI images	60
4.5	Xenon VMI ATI images	61
4.6	VMI ATI images at $\phi = 0$ and $\pi$	62
4.7	Xenon phase-energy asymmetry maps at different angles	64
4.8	Xenon phase-angle asymmetry maps in different energy ranges	65
4.9	Argon phase-angle asymmetry maps at $3 \times 10^{13} \text{ W/cm}^2$	66
4.10	Argon phase-angle asymmetry maps at $2 \times 10^{14} \text{ W/cm}^2$	67
4.11	Krypton phase-angle asymmetry maps at $1.7 \times 10^{14} \text{ W/cm}^2$	68
4.12	Cuts through the asymmetry maps in argon at $3 \times 10^{13} \text{ W/cm}^2$	69
4.13	Cuts through the asymmetry maps in argon at $2 \times 10^{14} \text{ W/cm}^2$	69
4.14	Potential energy curves involved in the $D_2$ experiment	71
4.15	Ion fragment kinetic energy spectra of $D_2$	72
4.16	2-D momentum distribution image for $D_2$ dissociation	74
4.17	Phase-energy asymmetry map for the $D_2$ ion fragment emission	75
4.18	Modelled electron localisation in the dissociation of $D_2^+$	77
4.19	Measurement of the CE-phase directly at the HHG target	80

# Introduction

Nowadays, it is impossible to imagine life without semiconductor and laser technology. The first theoretical foundation for the laser, or even prediction of the laser with the coefficients for absorption and stimulated emission, was laid by Albert Einstein in 1917 [1]. Since the first demonstration of a laser almost half a century ago [2], laser technology gradually invaded our everyday life. New developments in laser technology are being achieved continuously. Mode-locked lasers can deliver powerful light pulses with a duration of only a few optical cycles [3], making it possible to investigate physical processes on timescales shorter than a femtosecond ( $1 \text{ fs} = 10^{-15} \text{ s}$ ).

The output (peak) power of mode-locked oscillators is generally not enough to study many interesting processes. Therefore, much effort is put into increasing the peak power of ultrashort pulses. The simplest approach is to amplify the output pulses from an oscillator in one or more amplification stages. However, since the peak powers of femtosecond pulses are so high, the damage threshold of the optical materials used is quickly reached. This technological problem was responsible for stagnation in the development of laser peak power until the discovery of chirped pulse amplification (CPA) in 1985 [4, 6, 7] solved this problem, as is clearly visible in figure 1. Higher peak powers can be reached at the cost of pulse repetition rate. Whereas mode-locked oscillators generally work at repetition rates around 100 MHz, reaching peak powers of a few megawatt, amplifier laser systems at kilohertz repetition rates can reach terawatt peak powers [8–21]. At even lower repetition rates of tens of hertz, peak powers from hundreds of terawatts up to more than a petawatt are feasible [22–25].

A drawback of the CPA technique however is the amplification bandwidth. Gain narrowing limits the duration of the amplified pulses to more than 10 fs, and requires the use of carefully designed special optical components. Therefore more recently, development has concentrated on the design of amplifier systems based on optical parametric amplification. The bandwidth of such amplifier systems, in which chirped pulses are amplified parametrically, supports pulses with a duration significantly below 10 fs [26–33].

Another approach is to increase the output peak power of mode-locked oscillators directly, by decreasing the oscillator repetition rate. For this, the oscillator cavity is enlarged. With this, pulse energies of several hundreds of nanojoules, and peak-powers of more than 10 MW have been achieved [34, 35].

Very recently, a third approach to increase the peak power of pulses from a femtosecond oscillator was demonstrated. This approach makes use of a passive cavity of high finesse, which is locked to the femtosecond oscillator [36, 37]. By this means, pulse energies of several microjoules at a repetition rate of 76 MHz were reached [38].

In order to achieve powerful pulses with a duration of just a few optical cycles, several methods have been demonstrated. All methods exploit self phase modulation to spectrally broaden the pulses substantially, and use a dispersive delay setup to temporally compress the pulses afterwards. The first method proposed for pulses at relatively high peak powers, up to about 100 GW, uses a hollow waveguide filled with a noble gas [8, 39–41]. A variation to

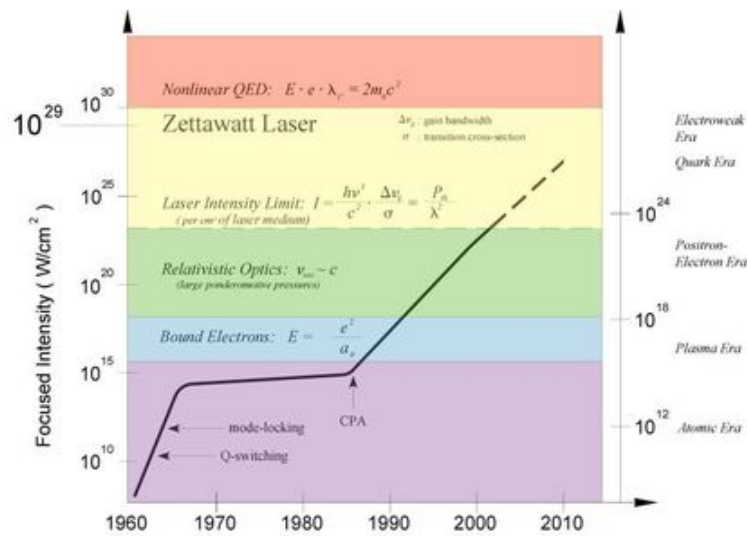


Figure 1: Development of laser peak power since the introduction of the laser in 1960. After a steep increase in laser peak power in the first years after the introduction of the laser, a stagnation of the development over the next 20 years can be observed. The technological problem of damage to the gain material and the optics was the main reason for this stagnation. After the invention of chirped pulse amplification [4] in 1985 the slope of the laser peak power development steepened significantly again. Image taken from [5].

this approach was implemented to compress pulses with even higher peak power in a rare gas filled hollow fibre in which a pressure gradient was maintained [25].

A second approach, which potentially can be scaled to even higher peak powers, into the terawatt regime, spectrally broadens the input pulses in a bulk material, and subsequently spatially filters the beam [42]. The maximum throughput of this method is 50 %.

Recently, successful compression of high peak power pulses through filamentation in a noble gas at low pressure was demonstrated [43, 44]. This method potentially gives a higher throughput than the other methods, and may also be applied to pulses with higher peak powers.

In the framework of this thesis, spectral broadening in a gas-filled hollow waveguide has been applied to successfully compress 15 fs pulses down to 5 fs at an energy loss of 50 %, yielding a peak power of 0.2 TW [21]. This is the highest peak power at 5-fs pulse duration achieved until now.

As optical pulses with durations of just a few optical cycles became available, the relative phase between the electric field and the pulse envelope, the carrier-envelope phase, became a significant variable. Control of this variable allows the investigation of many interesting processes. Work on controlling the carrier-envelope phase, or the phase difference between two subsequent pulses from a femtosecond oscillator [45–47] was rewarded with the Nobel Prize in 2005. Recently, control of the carrier-envelope phase difference between two subsequent pulses from a femtosecond oscillator was improved to an even higher degree of stability [48–50], which is of particular interest for applications that require stability over long periods of time.

With the energies available from femtosecond oscillators, several experiments have been carried out, demonstrating carrier-envelope phase-dependent phenomena. Photo-emission from

a solid surface [51, 52], and injection currents in semiconductors [53] were demonstrated to be carrier-envelope phase sensitive.

Some applications require more powerful pulses with a controlled carrier-envelope phase. However, since the carrier-envelope phase of a pulse is highly sensitive to many parameters, it is not enough to simply seed an amplifier using a carrier-envelope phase-stabilised oscillator. After amplification and recompression, a slow drift of the carrier-envelope phase can be noticed, and must be compensated for [54–57].

With carrier-envelope phase-controlled intense few-cycle pulses available, several studies have been carried out on photo-ionisation [58–64] and terahertz emission from a laser induced plasma [65]. Recently, control of electronic motion in molecules with the carrier-envelope phase of a few-cycle pulse was demonstrated for the very first time [66]. This work is presented in the last chapter of this thesis.

Combination of carrier-envelope phase-stable pulses with high-order harmonic generation lead to the generation of isolated burst of soft-x-ray radiation with sub-femtosecond duration, allowing for pump-probe experiments with attosecond-scale time resolution [67]. The attosecond streak camera technique allowed measuring the temporal characteristics (amplitude and phase) of the single attosecond burst [68] and to directly measure the electric field of an optical pulse for the first time ever [69]. More recently, the generated single attosecond pulses were used to probe the dynamics of strong field ionisation, that is, to resolve the temporal structure of both tunneling ionisation and multiphoton ionisation by a 5 fs infrared pulse [70].

The studies on carrier-envelope phase-dependent photo-ionisation allowed the development of an additional method to control the carrier-envelope phase of few-cycle pulses [71]. This allowed not only the control and measurement of the absolute phase of a few-cycle pulse, but also allowed experimental conditions to be exactly reproduced even after realignment of the laser system. In the framework of this thesis, substantial experimental improvements of this method were achieved [72].

In this thesis, the generation and application of carrier-envelope phase-controlled intense few-cycle light pulses are the central themes. In the first and second chapter, the generation of such pulses is presented, and in the third and fourth chapter the main current applications of these pulses are presented.

In the first chapter of this thesis the generation and characterisation of powerful few-cycle pulses is described. Several methods to characterise the pulse shape on a short time scale are presented. For powerful pulses, not only is the pulse shape on a short time scale important, but it is also important on longer time scales. Therefore a pulse characterisation method for longer time scales, with a larger dynamic response is presented. Finally, a beam quality measurement, which is of crucial importance for experiments that require very high focused intensities. In the first chapter, the complete temporal and spatial characterisation of the most intense 5 fs pulses achieved to date is presented.

In chapter 2 the advances made in the framework of this thesis on the control over the carrier-envelope phase of intense few-cycle pulses are presented. To this end, two different methods and approaches to stabilise the pulse-to-pulse phase-shift in oscillators are compared. The efforts made to improve the stabilisation and control of the carrier-envelope phase in amplifier systems are presented in chapter 2.2. Decoupling of the stabilisation of the amplifier and oscillator improved both the phase noise of the amplified pulses and the time over which it was possible to deliver phase stable pulses.

In the final section of chapter 2 an experiment is presented in which the carrier-envelope phase of intense few-cycle pulses was measured directly. The outcome of this experiment was that direct control of the carrier-envelope phase was achieved.

The generation of isolated attosecond pulses is treated in chapter 3. In the last section of this chapter a recent experiment is presented in which attosecond pulses were employed for a time-resolved measurement of ionisation processes.

With carrier-envelope phase stable pulses it is possible to control the outcome of various physical and chemical processes. In chapter 4 ionisation by intense few-cycle pulses is investigated, in which the full 3-dimensional momentum distribution of the electronic or ionic products was measured. The measurements presented in this chapter are the first of this kind presented with intense few-cycle pulses, and the results give a greater insight into the mechanisms involved in ionisation. The final experiment described in chapter 4.4 demonstrates control of electron localisation in molecular dissociation with the carrier-envelope phase of a few-cycle pulse.

As it is a good tradition in our group, all data on which this thesis is based is archived on our groups data-archive-server, where it is accessible for all co-workers in the group. Together with the raw data, a description is given on how this raw data is used to derive the presented results (as far as this is not obvious, or not presented in the text of the thesis).

## List of publications

### *Peer reviewed*

1. M. Uiberacker, Th. Uphues, M. Schultze, A. J. Verhoef, V. Yakovlev, M. Kling, J. Rauschenberger, N. M. Kabachnik, H. Schröder, M. Lezius, M. Vrakking, S. Hendel, U. Kleineberg, U. Heinzmann, M. Drescher and F. Krausz, *Attosecond real-time observation of electron tunneling and multi-electron dynamics in atoms*, **Nature**, submitted.
2. A. J. Verhoef, A. Fernández, M. Lezius, K. O’Keeffe, M. Uiberacker, F. Krausz, *Few-cycle carrier envelope phase-dependent stereo detection of electrons*, **Opt. Lett.** **31**, 3520 (2006).
3. M. F. Kling, Ch. Siedschlag, A. J. Verhoef, J. I. Khan, M. Schultze, Th. Uphues, Y. Ni, M. Uiberacker, M. Drescher, F. Krausz and M. J. J. Vrakking, *Control of Electron Localization in Molecular Dissociation*, **Science** **312**, 246 (2006).
4. A. J. Verhoef, J. Seres, K. Schmid, Y. Nomura, G. Tempea, L. Veisz and F. Krausz, *Compression of the pulses of a Ti:sapphire laser system to 5 femtoseconds at 0.2 terawatt level*, **Appl. Phys. B** **82**, 513 (2006).
5. J. Seres, E. Seres, A. J. Verhoef, P. Wobrauschek, Ch. Strelt, V. Yakovlev, Ch. Spielmann and F. Krausz, *Source of coherent kiloelectronvolt X-rays*, **Nature** **433**, 596 (2005).

### *Conference Proceedings*

1. J. Rauschenberger, A. J. Verhoef, T. Fuji, M. Hentschel, T. Udem, C. Gohle, T. W. Hänsch and F. Krausz, *Carrier-envelope phase-stabilized amplifier system*, **Cleo Europe/EQEC 2005**, Munich, Germany, (2005).
2. J. Seres, E. Seres, A. J. Verhoef, G. Tempea, Ch. Spielmann, F. Krausz, *A 6-femtosecond Sub-Terawatt All-Solid-State Ti:sapphire Laser System*, **Advanced Solid State Photonics (ASSP)**, Vienna, Austria, TuA2 (2005).

## Chapter 1

# High power pulse compression into the few-cycle regime

In this chapter the compression of powerful 15 to 25 fs pulses into the few-cycle regime will be described. In the first experiment 1-mJ, 25-fs pulses were spectrally broadened in bulk material. In the second experiment, 2-mJ, 15-fs pulses were spectrally broadened in a Neon-filled hollow waveguide, and subsequently compressed to 5 fs [21]. For the experiments described in Section 3.2 and Chapter 4 1-mJ, 25-fs pulses were broadened in a Neon-filled hollow waveguide to less than 5 fs.

For all experiments, the temporal and spatial characterisation is routine, though crucial, therefore several methods of pulse characterisation and a measurement of beam quality will be presented in this chapter as well.

### 1.1 Spectral broadening in a bulk material

Spectral broadening of ultrashort pulses is always achieved by using self phase modulation in one way or another. Since self phase modulation is strongly correlated to the peak intensity of the pulses, in order to achieve strong spectral broadening pulses are normally focused onto the medium wherein the self phase modulation is accomplished. For very energetic pulses, this gives rise to technical difficulties that can not be easily dealt with. Upscaling of the methods available for lower energy pulses yield impractical sizes for the setup needed, or the medium may get damaged because of the high pulse energy. Several methods have been proposed, for example spectral broadening in a hollow waveguide with a pressure gradient [25] or spectral broadening in multiple filament stages [43, 44]. Another proposal with promising prospects is to focus powerful pulses and to put a bulk material at an appropriate position before the focus [42]. In the focus a pinhole is placed to spatially filter the beam. The spatial filter ensures that the output beam is spatially homogeneous, and has a throughput of roughly 50 percent.

Pulses with a duration of 25 fs with 1 mJ of pulse energy from a 10-pass Ti:sapphire CPA were used to achieve broadening in a 3 mm thick sapphire plate. For this, the beam was focused using a spherical mirror with a focal length of 1 m, and in the focus a pinhole was placed. The sapphire plate was placed at a variable distance before the focus. When the sapphire plate is moved closer to the focus, the broadening gets larger, until at a certain point the transmitted beam gets inhomogeneous because the beam splits in several filaments inside the sapphire plate. Pinholes with different sizes were used in order to investigate the effect of the spatial filtering. With a smaller pinhole the throughput was less, but the transmitted spectrum smoother. In figure 1.1 spectra for different positions of the sapphire plate and for different pinhole diameters are shown. With the smallest pinholes the throughput was about

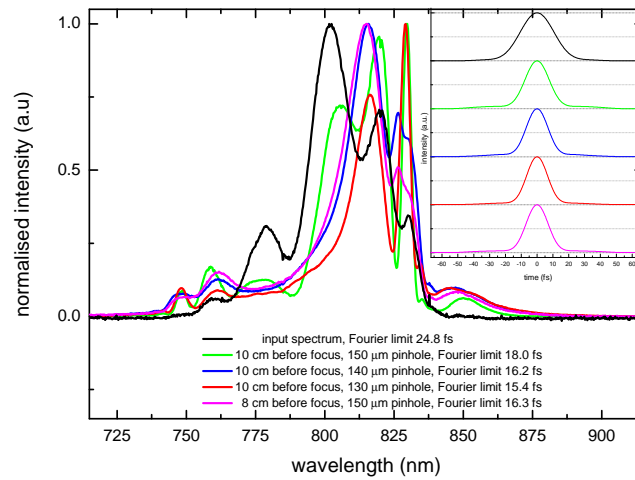


Figure 1.1: Spectral broadening in a 3 mm thick sapphire plate with 1-mJ, 25-fs pulses for different spatial filtering conditions and different intensities on the sapphire plate. Inset: the respective Fourier transform limited intensity profiles.

30 percent, with the biggest the expected 50 percent throughput was reached. The fourier transform limited duration of the spectrally broadened pulse when the most tight spatial filter was used was 15.4 fs.

From figure 1.1 it is clear that the results of the proof-of-principle experiment by Mével *et al.* [42] could not be reproduced in this experiment. The modulation on the input spectrum suggests that already before the bulk medium self phase modulation has shaped the pulses, and that the input pulses are most likely not Fourier limited. This self phase modulation is most likely accumulated in the prism-compressor of the laser, since the compressor pre-compensates a couple of meters pathlength through air, and a few millimeters of glass. In other words, this means that intense pulses as short as 25 fs travelled through several millimetres of glass, and because of the high intensity accumulated substantial self phase modulation. In this case, the self phase modulation did not cause substantial spectral broadening of the pulse, but it did introduce a substantial amount of higher order chirp on the pulse. In later experiments, the beam size at the output of the prism compressor was therefore substantially enlarged to suppress this self phase modulation, but this experiment was not repeated.

In addition, the input beam was clearly visible spatially modulated, which may have caused stronger inhomogeneous broadening along the beam profile than for a beam with a Gaussian profile. Although the spatial filtering homogenises the beam, the energy throughput is decreased. Part of the spatial inhomogeneities can be caused by non-linear effects in the prism compressor, and be solved by enlarging the beam that goes through the compressor. Some inhomogeneities may have been solved by cleaning optics in the beam path, and replacing slightly damaged optics. Later experiences have taught that these simple tasks could have solved most of the above problems, which would probably have lead to a better confirmation of the results in [42].



## 1.2 Spectral broadening in a rare gas filled hollow waveguide

### 1.2.1 Laser system providing 2-mJ, 15-fs pulses

Before discussing the spectral broadening and compression of the 2-mJ, 15-fs pulses to 5 fs, the laser system providing the input pulses is described. The results for the compression depend strongly on the correct alignment and configuration of the laser [21]. A schematic of the laser system is shown in Fig. 1.2. The amplifier system consists of three stages, and it is seeded by the pulses from a Ti:sapphire oscillator. The 9-fs pulses from the oscillator are stretched to about 10 ps with SF57 glass blocks and specially designed multilayer mirrors, which also serve for the pre-compensation of third-order dispersion (TOD).

The first stage of the amplifier consists of nine passes through the Ti:sapphire amplifier crystal, pumped with 50% of the output of a 20-mJ Q-switched, frequency-doubled Nd:YLF laser at a repetition rate of 1 kHz (Thomson CSF 621D). The Pockels cell was incorporated after the fourth pass, not only to separate pulses at 1 kHz from the 80 MHz pulse train of the oscillator, but also to suppress the amplified spontaneous emission (ASE) coming from the first four passes efficiently. The remaining energy of 10 mJ is used for pumping the second amplifier stage. The output pulses of approximately 1 mJ from the first stage are compressed in a LAK16A double-prism compressor to about 20 fs [17].

In order to overcome the loss of spectral width caused by gain-narrowing in the first amplifier stage, the pulses are focused into a fused silica hollow-core fibre (diameter: 150  $\mu\text{m}$ , length: 0.5 m, filled with Ar gas at a pressure of 0.6 bar). Here, the spectrum is broadened to have a full width at half maximum (FWHM) bandwidth of 120 nm. This ensures an output bandwidth after final amplification sufficient for approximately 10 fs pulses [18]. In order to achieve this short pulse duration, in addition to the spectral broadening in the hollow-core fibre, the spectral amplitude and phase over a wavelength range as broad as 350 nm are shaped with an acousto-optic programmable dispersive filter (AOPDF, DAZZLER) [19, 73], which is inserted after the hollow-core fibre. The beam pointing before the fibre is actively stabilised by two motorised mounts and a small split-off from the beam monitored on a CCD camera.

The DAZZLER is programmed to pre-compensate the large negative TOD and fourth order dispersion (FOD) of the final prism compressor together with specially designed chirped mirrors, so called TOD-mirrors. 44 reflections on the mirrors introduced a TOD and an FOD of about  $+26400 \text{ fs}^3$  and  $+79200 \text{ fs}^4$ , respectively. The DAZZLER is set to apply a group velocity dispersion (GVD) of  $-2000 \text{ fs}^2$  to ensure higher diffraction efficiency [19], and a TOD of  $+1700 \text{ fs}^3$  and an FOD of  $+16000 \text{ fs}^4$  to compensate the remaining high order dispersion. These values were fine-tuned experimentally, and agree well to the values calculated for the dispersion of the different parts of the system. The higher order dispersion affects the shape of the spectrum and the side wings of the pulses after the final hollow fibre. Secondly, the spectral shaping ability of the DAZZLER was used also to compensate partly the gain narrowing effect in the second and third amplifier stage and to get a smoother spectrum at the output of the third stage.

The second, six-pass amplifier stage compensates for the losses introduced by the hollow-core fibre and the DAZZLER. Before the DAZZLER the pulses are stretched to approximately 10 ps in an SF57 glass stretcher. The third and final stage incorporates three passes through a Ti:sapphire crystal cooled to 150 K by a closed loop cryostat, and pumped by 25-mJ pulses at 1 kHz from a Q-switched, frequency doubled Nd:YLF laser. The cryostatic cooling is necessary for minimising thermal aberrations in the amplifier crystal. In order to prevent

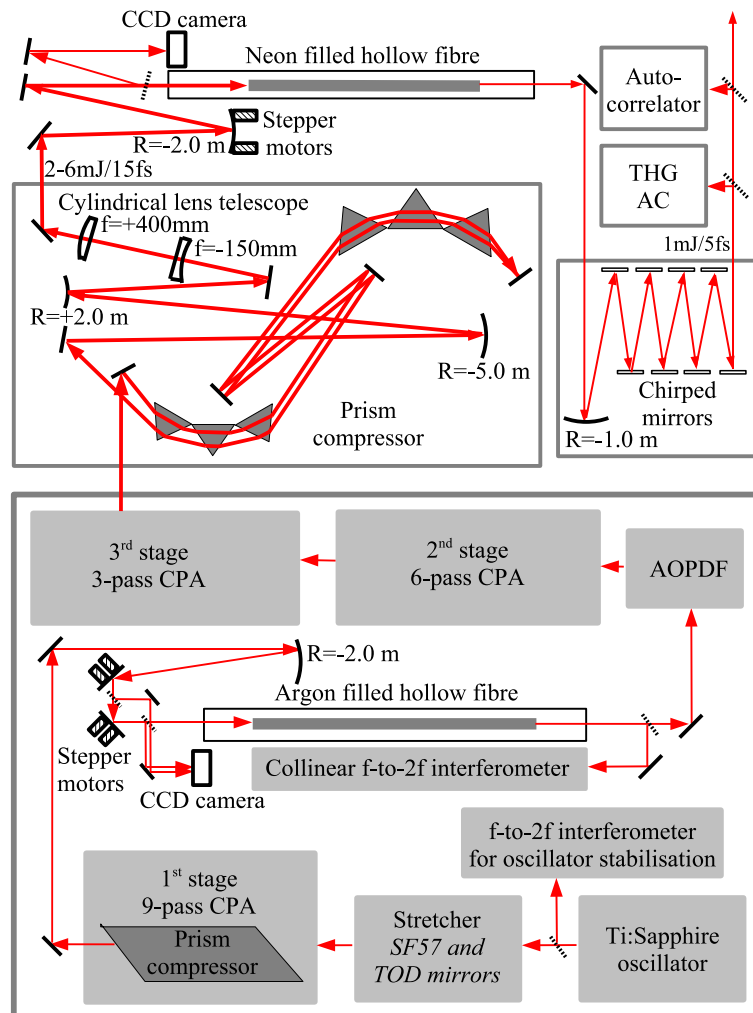


Figure 1.2: Schematic drawing of the amplifier system. After the first hollow fibre the pulses are shaped by means of an acousto-optic programmable dispersive filter (AOPDF). After the final prism compressor the beam is shaped with a spherical mirror telescope and a cylindrical lens telescope in order to achieve good focusing into the second hollow fibre. A small portion of the output energy is used to measure the autocorrelation trace and a third-order high-dynamic-range correlation (THG AC). The carrier envelope phase of the output pulses from the first amplifier stage can be stabilised, which will be discussed in chapter 2

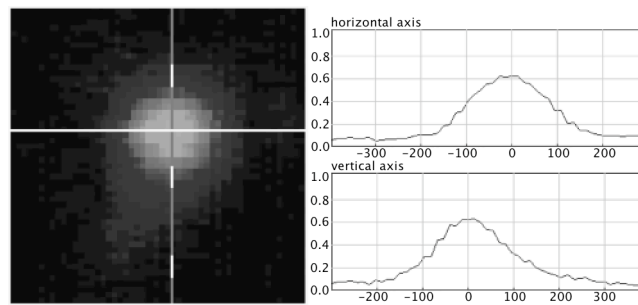


Figure 1.3: Beam profile at the entrance of the hollow-core fibre. The horizontal axes of the graphs are in micrometres.

damage to the crystal and mirrors, strongly divergent beams are led into the passes, and the crystal is out of the focuses. The 2-mJ pulses after the final amplification stage are compressed to 15 fs in a prism compressor consisting of two sets of fused-silica triple-prisms. The beam through the prism compressor is slightly divergent, to minimise the self-phase modulation and even to prevent damage of the prisms because of the high peak power of the pulses.

### 1.2.2 Generating 1-mJ, 5-fs pulses

In order to generate few-cycle pulses, the 15-fs 2-mJ pulses obtained from the final prism compressor are focused in a second hollow-core fibre. To achieve a good beam profile in the focus, the output beam of the final prism compressor is recollimated and resized to fit on our folding optics with a spherical mirror telescope. Additionally, a cylindrical lens telescope is used to compensate for the elliptical profile of the beam originating from the third amplifier stage, and for the residual astigmatism of the beam. The beam is focused into the fibre using a  $-2\text{-m}$  radius of curvature focusing mirror rather than a lens, in order to avoid self-phase modulation. In Fig. 1.3 the beam focal spot is shown, as it appears at the entrance of the hollow-core fibre, yielding a  $1/e$  waist of  $110 \pm 10 \mu\text{m}$ . The focusing mirror is fixed in a motorised mirror mount, which allows active beam pointing stabilisation by monitoring a small split-off from the beam on a CCD camera.

At the input and output of the fibre cell thin (0.5 mm) fused-silica windows at the Brewster angle were used. This has several benefits, ranging from decreasing the intensity on the windows to minimising the reflection losses without needing to use an antireflection coating that would reduce the damage threshold of the windows. These issues are particularly critical, given the high power of the incident pulses. The fibre was filled with neon at a pressure of 1.5 bar. The length of the fibre is 1 m and the core diameter is 0.3 mm. The measured beam  $1/e$  waist of  $110 \mu\text{m}$  of the focused beam matches the expected value for optimal throughput.

Pulses at the output of the fibre are compressed by means of ultra-broadband chirped mirrors [74], complementary pairs with almost constant negative GVD. For fine tuning of the dispersion and hence pulse duration a pair of moveable thin wedges is introduced in between the fibre and the chirped mirror compressor. The pulses exiting from the fibre cell propagate in vacuum to avoid lengthening due to the GVD of air. A small fraction of the energy is used to measure the pulse duration. Both second-order interferometric autocorrelation and third-order high dynamic range correlation were used for characterising the pulses.

Figure 1.4b illustrates the spectral broadening from 90 nm FWHM to 150 nm FWHM achieved in the final hollow-core fibre. If the spectrum is strongly modulated, the pulses will

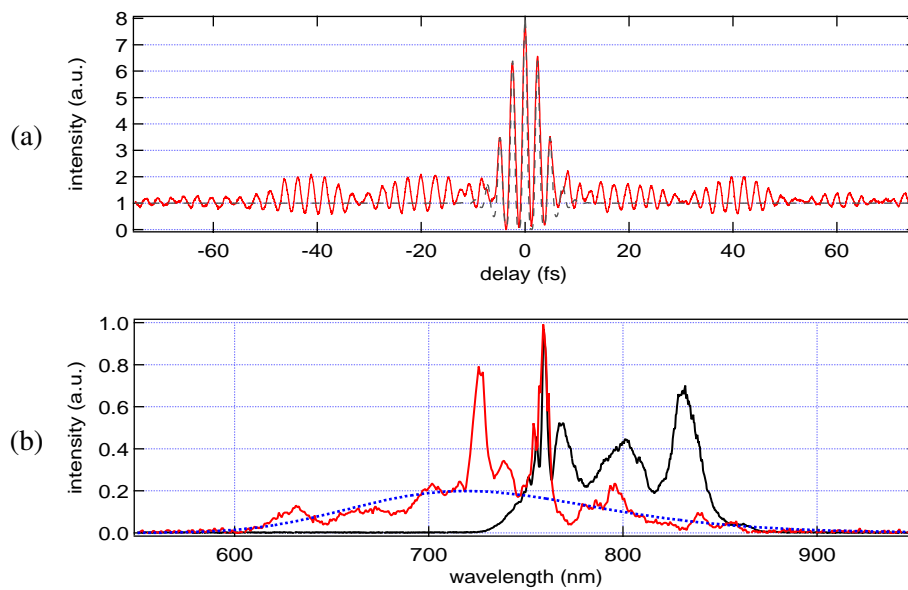


Figure 1.4: Spectrum and autocorrelation of the 1-mJ, 5-fs pulses.

(a) Autocorrelation of the compressed pulses (red) after the fibre with a fit (dotted black) on the assumption of a Gaussian pulse shape with central wavelength of 730 nm. The pulse duration is fitted to be 5.15 fs.

(b) Spectrum of the compressed pulses (red). The black curve is the input spectrum to the hollow core fibre. The dotted blue curve presents the fitted Gaussian spectrum corresponding to a pulse duration of 5.15 fs. The central wavelength and bandwidth (FWHM) of the input pulses are about 780 nm and 90 nm, while those of the output pulses are around 730 nm and 150 nm, respectively.

inherently exhibit large satellites (i.e. pre- or post-pulses with intensities possibly as large as 10 to 30 per cent of the main pulse intensity) even if the spectral chirp is mainly compensated. The modulations in the input spectrum (thick grey line) originate from self-phase modulation in the first hollow-core fibre. In order to minimise the energy contained by satellites, it is imperative to control the input spectrum of the second fibre carefully and hence control the output spectrum of the first fibre. Too high input energy at the entrance of the second fibre also gives rise to strong spectral modulation and consequently large satellites, which are promptly indicated by the autocorrelation measurement.

A blue-shift of the spectrum is clearly visible, the central wavelength being shifted from 780 to 730 nm. This blue-shift might be partially caused by multi-photon ionisation of the gas in the fibre (along with self-steepening). The good compression of the pulses with mirrors designed to compensate quadratic chirp (complementary pairs of mirrors providing almost constant negative GVD), indicates that the spectral phase of the pulses exiting from the fibre is well-behaved and that the spectral broadening is caused dominantly by self-phase modulation.

In Fig. 1.4a we show a typical autocorrelation curve of the compressed pulses. From the central wavelength of 730 nm and a fit to the autocorrelation curve assuming a Gaussian pulse shape (Fig. 1.4b, dotted black), the pulse duration is calculated as 5.1-5.2 fs. Increasing the input power to the fibre leads to higher losses, which are caused by multi-photon ionisation of the gas and/or by increased coupling to higher-order (lossy) fibre modes [40].

Higher-order (mainly third and fourth order) terms of the spectral phase carried by the pulses exiting from the fibre are the most likely reason why it was not possible to compress the pulses to the Fourier transform limit of 4.8 fs, since our chirped-mirror compressor was designed for compensating exclusively the quadratic phase term (i.e. the GVD).

### 1.2.3 Generating 400- $\mu$ J, sub-5-fs pulses

For this experiment the pulses from a 9-pass CPA (Femtolasers Femtopower Compact Pro), delivering 20-fs, 900- $\mu$ J pulses were used. The amplifier was seeded with an ultrabroadband Ti:Sapphire oscillator, delivering 6-fs pulses with a repetition rate of 78 MHz and an average output power of 350 mW. The pulses from the oscillator are focused into a periodically poled magnesium-oxide doped lithium niobate (PP-MgO:LN) crystal for spectral broadening and difference frequency generation (DFG) for phase stabilisation [49]. This will be discussed in more detail in chapter 2.1. The main part of the oscillator spectrum is sent into our pulse stretcher and stretched to 15 ps. The pulses are then amplified to 1 mJ pulse energy at a repetition rate of 3 kHz and subsequently recompressed to 20 fs in a prism compressor. That the pulses can not be compressed to the original duration of 6 fs is due to the spectral throughput of the stretcher and gain narrowing during amplification. A small fraction of the compressed pulses is sent into a collinear f-to-2f interferometer (discussed in chapter 2.2) that can be used for monitoring the carrier envelope phase and to stabilise it. The 900- $\mu$ J, 20-fs pulses were focused into a hollow fibre filled with Neon at approximately 2 bar for spectral broadening in order to be able to compress them into the few-cycle regime. A schematic of this setup is shown in figure 1.5. After the hollow fibre, we compress the pulses using chirped mirrors, which (pre-)compensate the beampath through air and all glass components until the experiment. The pulse duration is monitored with a second order interferometric autocorrelator by using a small split-off from the 400 $\mu$ J pulses. A typical spectrum and autocorrelation of our pulses is shown in figure 1.6.

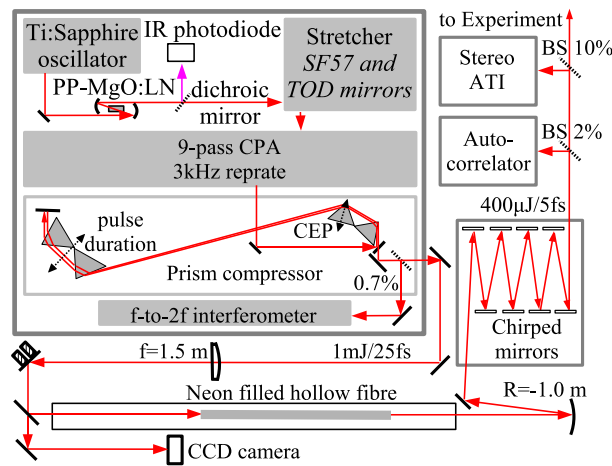


Figure 1.5: Schematic of our laser system. The Ti:Sapphire oscillator delivers 6 fs pulses with 350 mW of average power at a repetition rate of 78 MHz. The main part of the oscillator spectrum is sent into our pulse stretcher and stretched to 15 ps. The pulses are then amplified to 1 mJ pulse energy at a repetition rate of 3 kHz and subsequently recompressed to 20 fs in a prism compressor. A small fraction of the compressed pulses is sent into a collinear f-to-2f interferometer (discussed in chapter 2.2) that can be used for monitoring the carrier envelope phase and to stabilise it. Our 20 fs pulses are focused into a neon filled hollow fibre for spectral broadening and subsequently compressed to 5 fs in a chirped mirror compressor. We send a small split-off to a second order interferometric autocorrelator to monitor our pulse duration. A ten percent split-off from the main beam is used for the measurements with the stereo ATI that will be discussed in chapter 2.3.

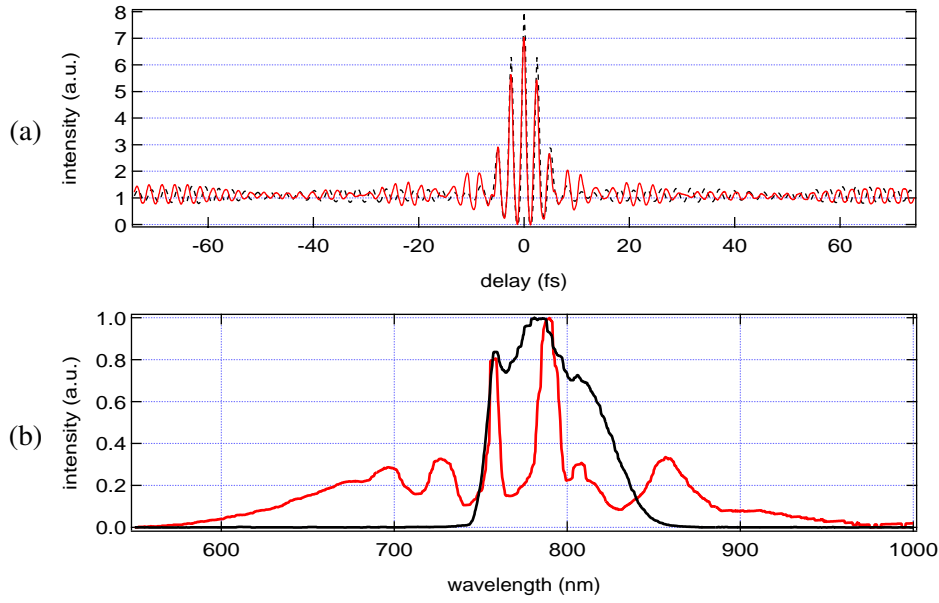


Figure 1.6: Second order autocorrelation and spectrum of the 400- $\mu$ J, sub-5-fs pulses. (a) The measured autocorrelation (red) agrees very well with the calculated autocorrelation from the spectrum assuming flat phase (dotted black curve). (b) The Fourier limited pulse duration of the broadened spectrum (red) is 4.8 fs. The input spectrum to the hollow fibre is shown in black.

## 1.3 Temporal characterisation of few-cycle pulses

### 1.3.1 Second order autocorrelation

One of the most widely used methods for temporal characterisation of ultrashort pulses is the second order autocorrelation. For the experiments described in this thesis, the second order interferometric autocorrelation was used for everyday pulse characterisation and monitoring. For an autocorrelation, the pulse under investigation is spatially and temporally overlapped with a copy of itself, and the response of a certain medium is measured. For the second order interferometric autocorrelation, both pulses are overlapped interferometrically, one time delayed from the other, and the second harmonic yield as a function of delay is measured.

In mathematical sense, the second order interferometric autocorrelation signal  $I_2(\tau)$  of a pulse with electric field  $\mathbf{E}(t)$  can be written as follows [75]:

$$I_2(\tau) = \int_{-\infty}^{+\infty} \left| [\mathbf{E}(t) + \mathbf{E}(t - \tau)]^2 \right|^2 dt \quad (1.1)$$

The pulse electric field can generally be written as

$$\mathbf{E}(t) = E(t)e^{i[\omega t + \Phi(t)]} \quad (1.2)$$

with  $E(t)$  the pulse envelope,  $\omega$  the carrier frequency and  $\Phi(t)$  the temporal phase shift of the

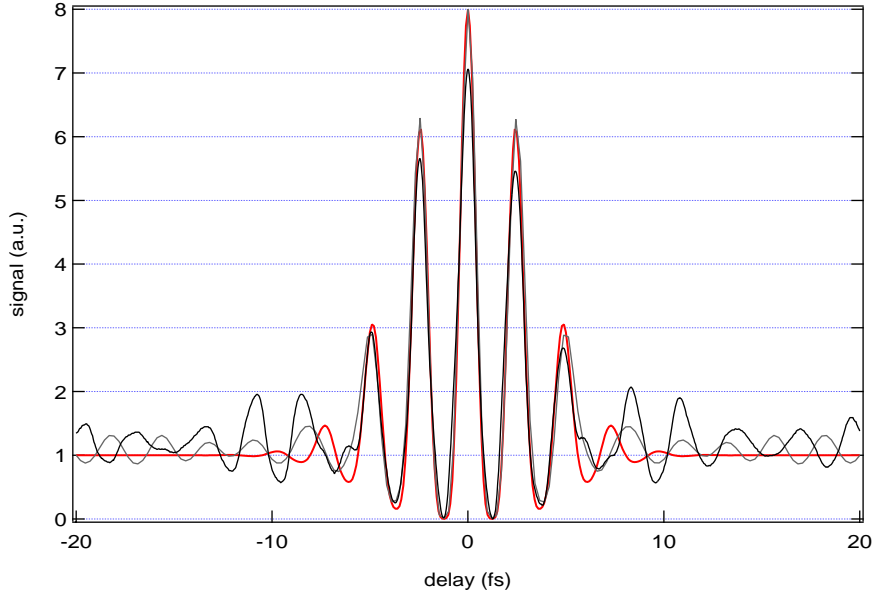


Figure 1.7: Second order autocorrelation of a 4.8 fs intensity FWHM Gaussian pulse with central wavelength 740 nm, calculated using eq. 1.6 (red curve), with a measured autocorrelation (black curve) and a calculated autocorrelation (gray curve) from the pulse spectrum as in fig. 1.6.

pulse (allowing for chirp on the pulse). Combining (1.1) and (1.2) yields

$$\begin{aligned}
 I_2(\tau) = \int_{-\infty}^{+\infty} & |2E^4(t) + 4E^2(t)E^2(t - \tau) \\
 & + 4E(t)E(t - \tau)[E^2(t) + E^2(t - \tau)] \cos[\omega\tau + \Phi(t) - \Phi(t - \tau)] \\
 & + 2E^2(t)E^2(t - \tau) \cos[2(\omega\tau + \Phi(t) - \Phi(t - \tau))]| dt
 \end{aligned} \quad (1.3)$$

Now for zero delay the signal is given as

$$I_2(\tau = 0) = 16 \int_{-\infty}^{+\infty} \mathbf{E}^4(t) dt \quad (1.4)$$

and for a delay far from overlap, the signal is given as

$$I_2(\tau \rightarrow \infty) = 2 \int_{-\infty}^{+\infty} \mathbf{E}^4(t) dt \quad (1.5)$$

giving a contrast for the second order autocorrelation of 8:1, as can be seen in figure 1.7 for a 5 fs intensity FWHM Gaussian pulse. The integral of equation 1.3 reduces for a gaussian pulse with FWHM  $T$  and center wavelength  $\lambda$  to the following expression:

$$\begin{aligned}
 I_2(\tau) = & 1 + 2e^{-2 \ln 2 \tau^2 / T^2} \\
 & + 4e^{-3/2 \ln 2 \tau^2 / T^2} \cos \left[ 2\pi \cdot \frac{c}{\lambda} \tau \right] \\
 & + e^{-2 \ln 2 \tau^2 / T^2} \cos \left[ 2\pi \cdot 2 \frac{c}{\lambda} \tau \right]
 \end{aligned} \quad (1.6)$$



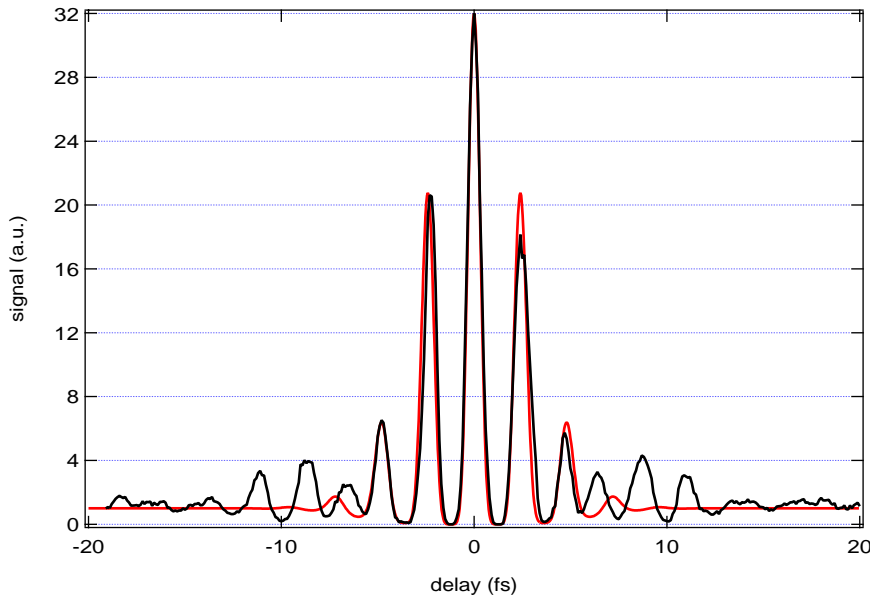


Figure 1.8: Third order interferometric autocorrelation trace, calculated for a 4.8-fs FWHM Gaussian pulse with central wavelength of 740 nm (red curve), and a measured trace (black curve) with a small split-off from the 400- $\mu$ J, sub-5-fs pulses.

Now it is possible to quickly calculate an autocorrelation for a pulse with given duration and central wavelength, and compare this with a measured autocorrelation trace. From the comparison it is then possible to estimate the pulse duration.

### 1.3.2 Third order interferometric autocorrelation

The second order interferometric autocorrelation of few-cycle pulses, or more general ultra-broadband pulses is generally believed to yield not the right result. The main cause of this, is that the second harmonic is generated in a crystal with finite thickness, and therefore not the entire bandwidth of the pulses is phase-matched. When instead of the second harmonic crystal, a glass surface is put in the focus, the third harmonic can be generated. This process, third harmonic generation on a surface, circumvents the phase matching problem. With appropriate filtering and using an appropriate detector, an interferometric autocorrelation of the third order can be measured [76, 77]. The signal  $I_3(\tau)$  measured can be written as

$$I_3(\tau) = \int_{-\infty}^{+\infty} \left| [\mathbf{E}(t) + \mathbf{E}(t - \tau)]^2 \right|^3 dt \quad (1.7)$$

with the same conventions as for the second order autocorrelation. Analogous to the second order autocorrelation, one can easily see that the contrast of the third order autocorrelation is 1:32. For a Gaussian pulse with central wavelength  $\lambda$  and a FWHM  $T$ , the third order

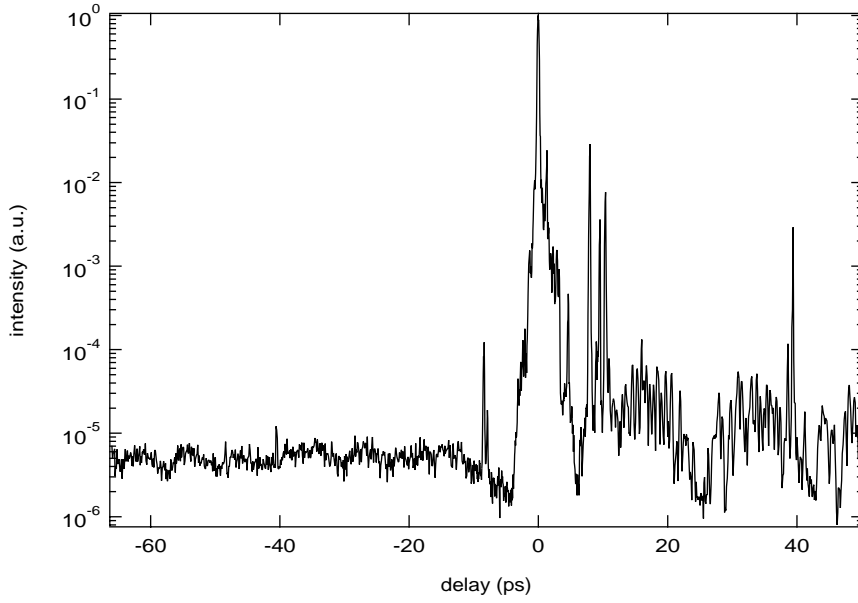


Figure 1.9: Third-order high-dynamic-range correlation curve of the compressed pulses from the system discussed in section 1.2.2. The measurement shows no pre-pulses. After the main pulse the measurement shows some periodic structure which most probably arises from spurious reflections inside the fibre cell.

interferometric autocorrelation can be expressed as

$$\begin{aligned}
 I_3(\tau) = & 1 + 9e^{-8/3 \ln 2\tau^2/T^2} \\
 & + \left(9e^{-3 \ln 2\tau^2/T^2} + 6e^{-5/3 \ln 2\tau^2/T^2}\right) \cos \left[2\pi \cdot \frac{c}{\lambda} \tau\right] \\
 & + 6e^{-8/3 \ln 2\tau^2/T^2} \cos \left[2\pi \cdot 2 \frac{c}{\lambda} \tau\right] \\
 & + e^{-3 \ln 2\tau^2/T^2} \cos \left[2\pi \cdot 3 \frac{c}{\lambda} \tau\right] \quad (1.8)
 \end{aligned}$$

With a setup as described above, a third order interferometric autocorrelation was measured of a small split-off from the 400- $\mu$ J, sub-5-fs pulses, the result of which is shown in figure 1.8, together with a calculated third order autocorrelation for a 4.8-fs FWHM Gaussian pulse with central wavelength of 740 nm.

### 1.3.3 High dynamic range third order correlation

Figure 1.9 shows the results of an (intensity) contrast ratio measurement of the pulse as recorded with a high dynamic range third-order correlator [22, 27, 78]. In a third-order correlation a pre-pulse with a contrast  $\alpha$  with respect to the main pulse at a time  $\tau$  before it generates a ‘ghost’ at  $-\tau$  after the main pulse with a contrast of  $\alpha^2$ . In the measured trace the absence of pre-pulses is obvious, the peaks at -8 ps and -40 ps with contrast ratios of  $10^{-4}$  and  $10^{-5}$  are only ‘ghosts’ of the post-pulses measured at 8 ps and 40 ps with contrast ratios of  $10^{-2}$  and  $10^{-2.5}$ . The pulse-to-pedestal contrast which originates from the several-ns-long ASE [20] is more than five orders of magnitude.

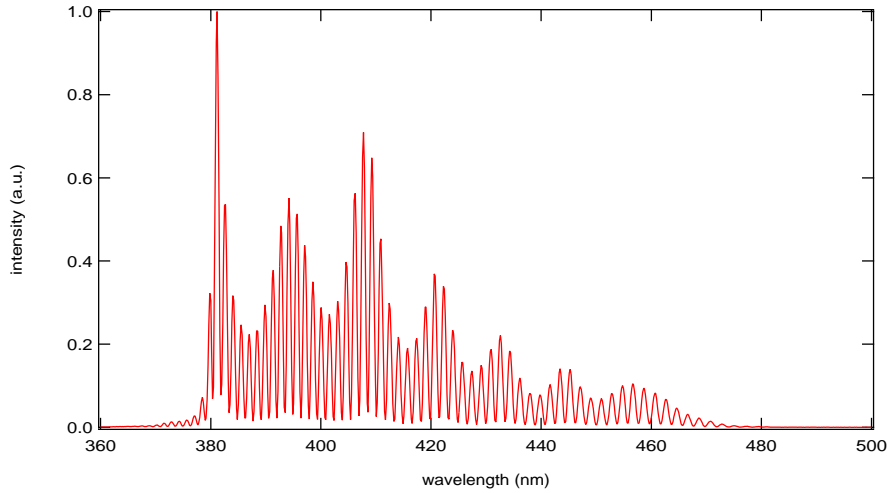


Figure 1.10: Measured SPIDER interferogram from a similar oscillator as used for seeding the amplifier in fig. 1.5

The drop, which appears before the main pulse, is the result of the saturation of amplification during the stretched ( $\sim 10$  ps) pulse. After the pulse some periodic signal with a period of approximately 20 ps is visible, an effect that is only visible after the fibre. This signal thus arises from some reflections inside the fibre compressor. The measured pulse-to-pedestal contrast is good, less than  $10^{-5}$ , which satisfies by far the requirements of the high-harmonic and single attosecond pulse generation, and the pulses are usable for a branch of non-relativistic plasma experiments. However, relativistic and  $\lambda^3$  experiments require further enhancement of this ratio [20].

### 1.3.4 SPIDER

For a typical SPIDER (Spectral Phase Interferometry for Direct Electric field Reconstruction, [79]) measurement one creates two identical copies of an input pulse, does a nonlinear conversion (sum frequency generation) with each of these two pulses and measures the resulting spectrum. The nonlinear conversion is done with another, stretched, copy of the pulse. So the first pulse is mixed with another frequency as the second. When the two ‘upconverted’ copies of the pulse are overlapped interferometrically, one can measure a spectral interferogram. From this interferogram (as can be seen in figure 1.10), the spectral phase can be derived, which together with a measured spectrum enables reconstruction of the relative temporal phase of the pulse, and thus the pulse duration.

The SPIDER interferogram  $D(\omega)$  can be written as follows:

$$\begin{aligned}
 D(\omega) = & |E(\omega)|^2 + |E(\omega - \Omega)|^2 \\
 & + 2|E(\omega)||E(\omega - \Omega)| \\
 & \cdot \cos(\phi(\omega) - \phi(\omega - \Omega) + \omega\tau)
 \end{aligned} \tag{1.9}$$

Inverse Fourier transforming  $D(\omega)$  yields a component around  $T = 0$  and components around  $T = \pm\tau$ . Filtering the components around  $T = \tau$  and  $T = 0$ , and Fourier transform-

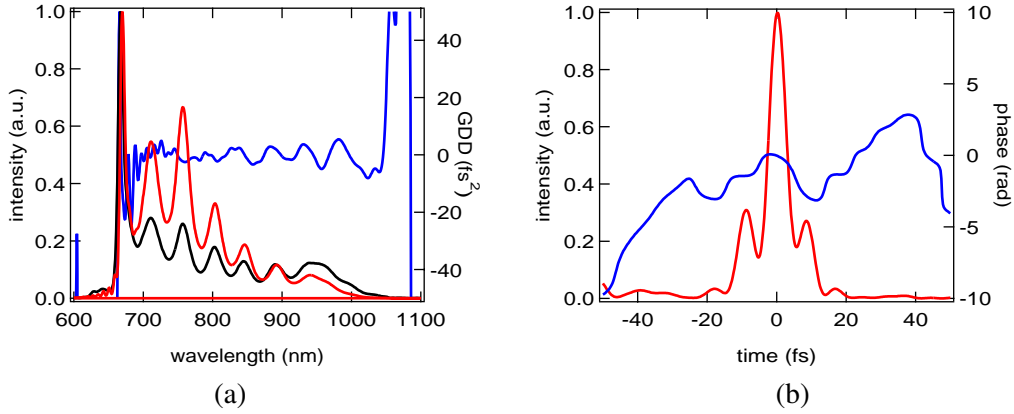


Figure 1.11: SPIDER reconstruction from fig. 1.10.

(a) Reconstructed spectrum (red) and group velocity dispersion (blue). The reconstructed spectrum is close to the measured spectrum (black), indicating that the results of the SPIDER reconstruction can be expected to be accurate.

(b) Reconstructed temporal intensity (red) and phase (blue). The intensity FWHM is 5.8 fs.

ing the results yield respectively:

$$D^{(T=+\tau)}(\omega) = |E(\omega)||E(\omega - \Omega)| \cdot \exp [i(\phi(\omega) - \phi(\omega - \Omega) + \omega\tau)] \quad (1.10)$$

$$D^{(T=0)}(\omega) = |E(\omega)|^2 + |E(\omega - \Omega)|^2 \quad (1.11)$$

To find both the spectral phase and the spectral amplitude, the following formula is used:

$$\overline{F(x)}^A = \frac{1}{A} \int_{-\infty}^x [F(\xi) - F(\xi - A)] d\xi \quad (1.12)$$

The overline represents the gliding average over a span of length  $A$ . The phase is retrieved by applying eq. (1.12) to the argument of  $D^{(T=+\tau)}(\omega)$  minus  $\omega\tau$ , with  $A = \Omega$ .

To find the spectral amplitude the following procedure is used. Combine  $D^{(T=0)}(\omega)$  and  $|D^{(T=+\tau)}(\omega)|$  to get  $|E(\omega)| + |E(\omega - \Omega)|$ . By shifting the resulting array by  $\Omega$  and subtracting the result from the original, one gets  $|E(\omega)| - |E(\omega - 2\Omega)|$ , to which (1.12) can be applied, with  $A = 2\Omega$ . This reconstruction of the spectral amplitude can be compared with a measured spectrum of the pulses, and is very useful for calibrating the computer reconstruction code.

Since now both the spectral phase and the spectral amplitude are known, the temporal evolution of the phase and intensity of the pulse can also be found, by simply inverse Fourier transforming the pulse in the frequency domain. However, one the phase may still be offset by a constant value, so the absolute phase of the pulse is not determined. In figure 1.11a and b respectively the reconstructed spectral phase and temporal phase and intensity are shown.

The SPIDER apparatus needs to be calibrated very precisely in order to give good results, the two variables that are most critical are  $\tau$  (or the slope  $\nu\tau$ ) and  $\Omega$ . The first can be determined quite well, but at good values of  $\tau$ , it is very difficult to determine  $\Omega$  with enough precision.

For ultrabroadband pulses it is extremely difficult to do a reliable SPIDER measurement, two of the main reasons for this are originating from the huge spectral width of few-cycle

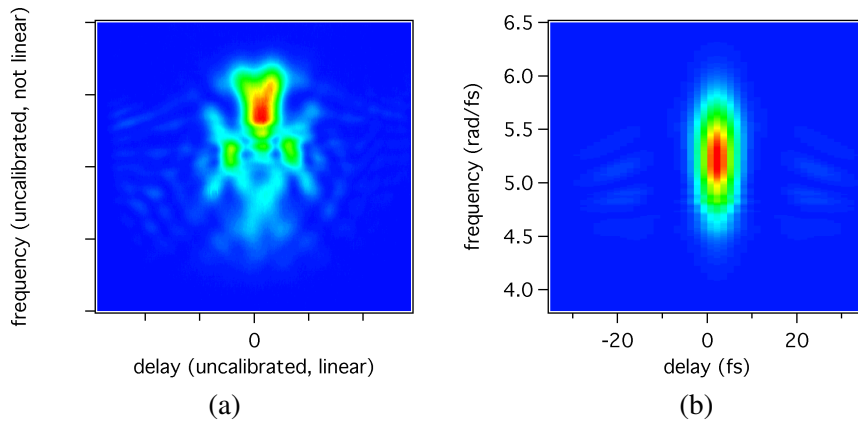


Figure 1.12: (a) Measured FROG trace. The frog device was not calibrated at the time of this writing, it is still in testing. It should be stressed that the frequency axis is by no means linear, which allows only for very qualitative remarks at this point.

(b) Calculated FROG trace for pulses with the same spectrum as in (a), on the assumption of a flat phase. Some general features at larger delays can be seen in both the measured and calculated trace, while the complicated structure at smaller delays in the measured trace hint at a more complicated spectral phase. This is most likely due to the dispersion-oscillations introduced by the chirped mirrors, although they were designed to introduce as little oscillations as possible.

pulses. The first complication is a technical one, since the SPIDER signal is quite weak, and therefore a lot of the strong fundamental light can give a background which can not be separated from the signal so easily. The second complication is simply that phase matching is limited, and therefore the weak signal in the wings of the spectrum is attenuated to be even weaker.

### 1.3.5 Frequency resolved optical gating – FROG

Another method able to retrieve the full temporal information of a pulse is frequency resolved optical gating (FROG) [80, 81]. This method has been successfully applied to few-cycle pulses [82], but is like SPIDER still far from routine for this kind of pulses. A second-harmonic-generation (SHG) FROG trace was measured with a small split-off from the 400- $\mu$ J, sub-5-fs beam.

A SHG-FROG trace of a pulse is a so called spectrogram of the autocorrelation of the pulse. So, what is measured, is the spectrum of the second harmonic as a function of delay. Mathematically, the SHG FROG signal is written as

$$I_{FROG}^{SHG}(\omega, \tau) = \left| \int_{-\infty}^{+\infty} E(t)E(t - \tau)dt \right|^2 \quad (1.13)$$

with  $E(t)$  the pulse electric field. Through an iterative deconvolution algorithm, the pulse electric field can be reconstructed. For a SHG FROG measurements, there are however a few ambiguities left over for the reconstruction. The first, like with SPIDER, is the absolute phase of the pulse. The second, as with any other method where the pulse measures itself is the absolute timing. The third can be seen easily as well, the SHG FROG is insensitive to

time inversion, which this method has of course in common with its not spectrally resolved equivalent, the second order autocorrelation. Except for these three ambiguities, the SHG FROG allows to fully retrieve all phase information of the pulse.

Figure 1.12 shows an uncalibrated measured FROG trace at the output of the laser system in figure 1.5, together with a calculated trace for the same pulses assuming flat phase. The measured trace is not calibrated, since the device used is still in development, and especially the frequency calibration can not be done as straightforward as for commercially available FROG devices. The main reason for this is that the large bandwidth requires to spectrally disperse the trace with a prism instead of a grating. However, a few qualitative remarks can be made. First of all, at larger delays, in both the calculated and measured trace some weak common features can be seen, allowing to make some estimates about the timing, and it seems that the pulse is reasonably compressed. In the measured trace, a more complicated structure is visible around the zero delay. This hints at a more complicated phase-evolution, which most likely is caused by the unavoidable dispersion oscillations introduced by the chirped mirror compressor. The chirped mirrors used are designed to have as small oscillations as possible, for the mirror combination used, but of course these oscillations can not be entirely suppressed for the large bandwidth of the pulses.

## 1.4 Spatial beam-characterisation

The spatial quality of the 1-mJ 5-fs laser beam was characterised by measuring the  $M^2$  parameter. The  $M^2$  value was obtained by focusing the beam and retrieving the beam size as a function of the position, with at least one measurement in the focus. The size of the beam is obtained by the knife-edge-method. The focal position and size were accurately determined and measured with a microscope objective and a CCD camera.

The  $M^2$  can be found by fitting the diameter of the beam as a function of the position to the formula describing the size of a Gaussian beam as a function of position, which yields the Raleigh length,  $z_R$ . Using

$$M^2 = \pi w_0 \theta / \lambda \quad (1.14)$$

where  $\lambda$  is the laser central wavelength,  $w_0$  is the measured  $1/e^2$  radius of the focus and

$$\theta = w_0 / z_R \quad (1.15)$$

the  $M^2$  of the cylindrically symmetric beam is measured to be  $1.8 \pm 0.1$ , as shown in Fig. 1.13, which indicates good focusability of the beam after the fibre.

The beam profile after the fibre was Bessel-like, as expected from hollow-core fibres. It should be noted that an ideal Bessel-like profile inherently gives an  $M^2 > 1$ . The small  $M^2$  value is not surprising, since the fibre acts as a spatial filter, which in our case substantially improved the quality of the beam. Improving the  $M^2$  value of a beam is highly beneficial, since upon fixed focusing the peak intensity scales as  $M^4$ , as the focused beam waist scales with  $M^2$ . Especially for experiments where very tight focusing is required this may be a crucial figure of merit. The maximum intensity that can be reached upon tight focusing is around  $10^{18} \text{W/cm}^2$  for the pulse parameters discussed. In a laser-plasma experiment more than  $10^{17} \text{W/cm}^2$  has been routinely reached [83].

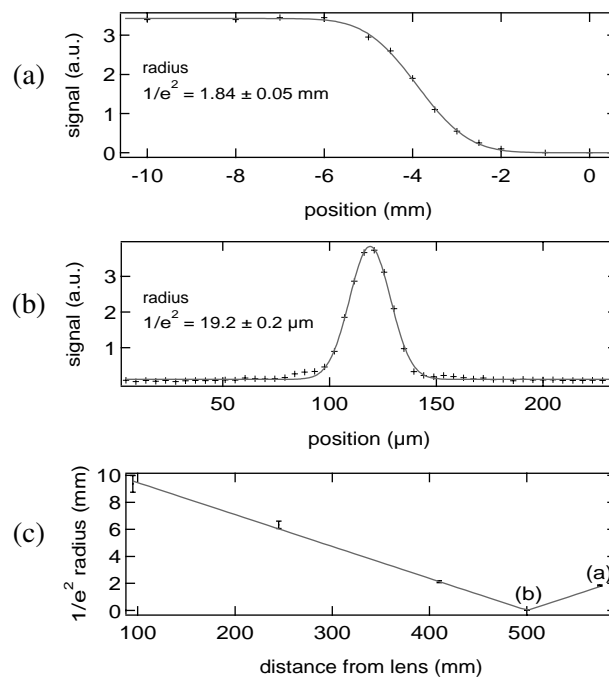


Figure 1.13:  $M^2$  measurement of the 1-mJ, 5-fs beam.

(a) Measurement of the beam profile, 75 mm after the focus (knife edge method), and a fit on the assumption of a Gaussian beam profile.

(b) Beam profile in the focus (measured with a CCD camera) and a fit on the assumption of a Gaussian beam profile.

(c) Measurement of the beam size evolution along the propagation direction together with a fit, which yields an  $M^2$  of  $1.8 \pm 0.1$





## Chapter 2

# Carrier-envelope phase stabilisation of ultrashort pulses

In this chapter the carrier-envelope phase stabilisation of oscillators and amplifiers will be discussed. Until now, two approaches are available to stabilise the phase of oscillators. Both will be described in the first section of this chapter. In the second section of this chapter two methods to stabilise the carrier-envelope phase of amplifiers will be discussed. The measurement and control of the absolute phase of intense few-cycle pulses is discussed in the third section of this chapter.

## 2.1 Carrier-envelope phase stabilisation of oscillators

### 2.1.1 The frequency comb

Two different approaches for stabilising the carrier-envelope phase of femtosecond oscillators have been demonstrated. The first is called the f-to-2f technique, the second on f-to-zero. Both approaches require broadening of the oscillator spectrum to cover an entire optical octave. Both approaches can be easily explained as follows: In any resonator, only those modes can exist, which fulfill the simple condition that an integer number of oscillations fit in one roundtrip [84]. So for a laser, only those wavelenghts  $\lambda$  for which  $n\lambda = l$  with  $l$  the cavity length, can exist in the resonator, and therefore be emitted through the output coupler. In the frequency domain, all modes (with optical frequency  $\nu$ ) resonant in the laser are integer multiples of  $f_{\text{rep}} = 1/T$  when  $T$  is the cavity roundtrip time, and hence  $f_{\text{rep}}$  the repetition rate.

Now, ideally, in case of a mode-locked laser, this would ensure that all pulses emitted from the laser would have the same carrier-envelope phase, but this is not the case. The intracavity dispersion shifts the resonant modes such that they are no longer an integer multiple of the oscillator repetition rate  $f_{\text{rep}}$ , but they are offset by a certain amount  $f_{\text{offset}}$ , as is graphically shown in fig. 2.1. This offset is directly linked to the phase-shift  $\Delta\phi$  between two subsequent pulses emitted from the oscillator, such that:

$$\Delta\phi = 2\pi f_{\text{offset}}/f_{\text{rep}} \quad (2.1)$$

### 2.1.2 The f-to-2f technique

For oscillators seeding an amplifier, a substantial fraction of the oscillator output is split-off for the super-continuum generation, while the remaining part is seeded for amplification. The spectral broadening is generally accomplished by self-phase modulation in a so called photonic crystal fibre (also called micro-structured fibre or holey fibre) [45–48]. In figure 2.2 a

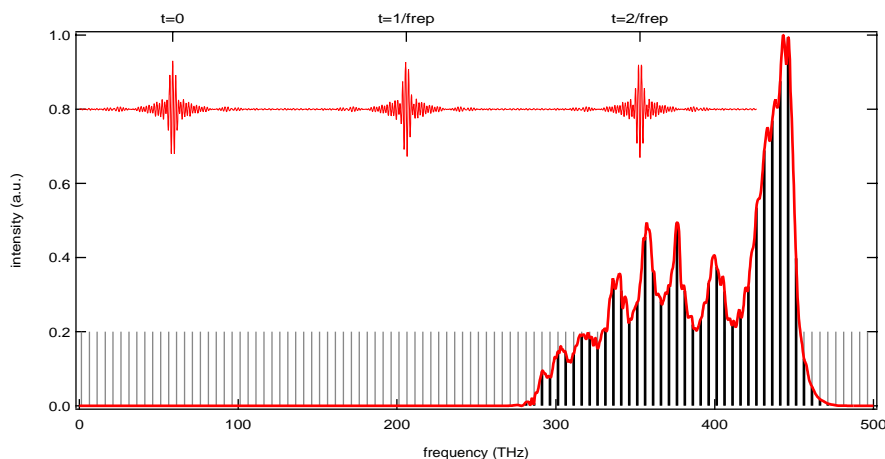


Figure 2.1: Spectrum of a femtosecond oscillator, with in black a corresponding frequency comb. In gray the frequency comb is extrapolated, to make the comb offset from zero visible. The inset shows the pulse train corresponding to the frequency comb, which shows a clear  $\pi/2$  phase shift between each pulse.

schematic of a typical setup for this technique is shown. A dichroic mirror is used to split off the long wavelength part of the supercontinuum from the short wavelength part. The short wavelength part of interest is around the second harmonic of the long wavelength part of interest. The long wavelength part of interest is frequency-doubled, and this frequency-doubled light is recombined interferometrically with the short wavelength part. The resulting signal is measured with a so called avalanche photodiode. When the frequency-spectrum of the electric signal from the photodiode is analysed, sidebands to the oscillator repetition rate are visible. This is the so-called beat-signal. This signal is visible as well as sidebands to zero-frequency.

The origin of the beat signal can be shown as follows, reducing the wavelength parts of interest to single modes from the oscillator (or the spectrally broadened pulse train): The mode of interest with the long wavelength has optical frequency  $n f_{\text{rep}} + f_{\text{offset}}$  and the mode of interest with the short wavelength has optical frequency  $m f_{\text{rep}} + f_{\text{offset}} = 2n f_{\text{rep}} + f_{\text{offset}}$ , with  $n$  and  $m$  integers. When now the long wavelength mode is frequency-doubled, this will be a signal at optical frequency  $2n f_{\text{rep}} + 2f_{\text{offset}}$ . When the original short wavelength part and the frequency-doubled long wavelength part interfere, this will be an addition of two sine-waves with a frequency difference of  $f_{\text{offset}}$ . And it is well known that two sine-waves with different frequencies added result in a carrier at the sum frequency, and a beat at the difference frequency, which is in our case exactly the frequency offset of the comb. When looking at the electric signal from a photodiode, one can easily understand that only this beat is detected.

The oscillator is now phase-stabilised by stabilising this beat frequency, ensuring a constant phase shift between two subsequently emitted pulses from the oscillator. When one stabilises the beat frequency to a quarter of the oscillator repetition rate, one can see from equation 2.1 that the phase difference between two neighbouring pulses will be  $\pi/2$ , and thus that every fourth pulse will have the same carrier-envelope phase.

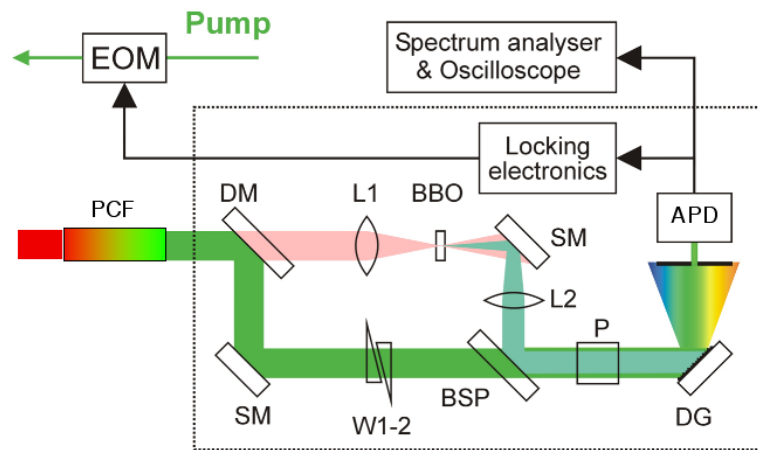


Figure 2.2: A typical setup of an  $f$ -to- $2f$  interferometer used for phase stabilisation of a mod-locked oscillator. The oscillator spectrum is broadened to a full octave in the PCF (photonic crystal fibre), and a beating is detected between the second harmonic of the infrared part and the fundamental blue part. An error signal is generated from this to stabilise the oscillator by modulating the pump laser intensity.

### 2.1.3 The $f$ -to-zero technique

For the  $f$ -to-zero technique, not the second harmonic of a long wavelength mode is used, but the difference frequency of two (sets of) modes in the oscillator is generated and overlapped with a long wavelength mode [85]. Mathematically, two modes  $m f_{\text{rep}} + f_{\text{offset}}$  and  $k f_{\text{rep}} + f_{\text{offset}}$  are combined to  $(m - k) f_{\text{rep}}$  and overlapped with  $n f_{\text{rep}} + f_{\text{offset}}$ , with  $m$ ,  $k$  and  $n$  integers and  $m - k = n$ . One now easily sees that this produces as well a beat at  $f_{\text{offset}}$ , as is shown in figure 2.3, and this can be stabilised as in the  $f$ -to- $2f$  case.

This technique is implemented easily for ultra-broadband oscillators, that provide an almost octave spanning output spectrum [49]. The output pulses are focused into a crystal optimised for difference frequency mixing with a resulting output close to the long wavelength part of the oscillator spectrum. And due to self phase modulation in the same crystal, the spectrum is broadened to include the same long wavelength. Consequently, at this long wavelength a beat signal is generated. One can easily detect a beat signal behind a longpass filter, and thus still use almost the full energy of the oscillator for further experiments or amplification. A filter that transmits only the beat signal and reflects the main part of the spectrum is easily found, for example a chirped mirror for compressing the output pulses from the oscillator, or even a broadband high reflector will do. In the schematic in figure 1.5 on page 12 this implementation is included.

### 2.1.4 Comparison of the two techniques

In principle, both techniques are equivalent, however, the implementation is what makes the difference. The implementation of the  $f$ -to- $2f$  technique relies on an interferometer, and on a fibre with a small core diameter, making the device very alignment sensitive. This makes it more difficult to maintain operation over long periods of time. The implementation of the  $f$ -to-zero technique, can in principle be adjusted to function in an  $f$ -to- $2f$  mode [50], but the  $f$ -to-zero still has some advantages, most prominent of which is that its detection wavelength

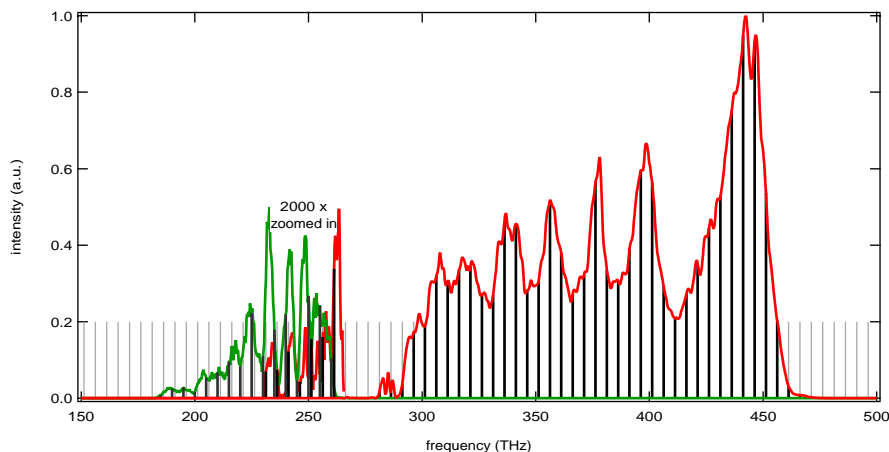


Figure 2.3: The spectrum (red) of an ultrabroadband oscillator and the DFG signal (green) it generated, with a frequency comb represented under it. The low frequency (long wavelength) part is blown up, to make it visible.

is far from any other wavelengths used in the system, and therefore subject to less noise. The presented implementation of the f-to-zero technique is superior to the presented implementation of the f-to-2f technique, because it requires no interferometric setup, and it is therefore much less sensitive to alignment.

## 2.2 Carrier-envelope phase of amplified pulses

### 2.2.1 Measurement of the carrier-envelope phase after amplification

After stabilising the phase (actually the pulse-to-pulse phase shift) of the oscillator with one of the methods described in the previous section, it is possible to select only pulses for amplification that have the same carrier-envelope phase [54, 55], by dividing the oscillator repetition rate by an integer multiple of 4. Because the repetition rate of amplifier systems is so much lower than that of the seed oscillator, this imposes practically no limitations on the amplifier repetition rate. Although the carrier-envelope phase of the pulses picked for amplification is the same, it is not said that after amplification this is still the case. This can be only verified with a measurement that can determine the carrier-envelope phase of a single laser pulse. It is possible to use the same concept for this as for stabilising the phase of an oscillator, to broaden the spectrum of the amplified pulses to cover a full octave, and measure a beating between the second harmonic of the long wavelength part, and the short wavelength part of the broadened spectrum. To measure the beating in the time domain would not allow for a single shot measurement. However a measurement in the frequency domain can reveal the carrier-envelope phase in a single shot measurement. When the fundamental pulse  $E_{\text{fund}}(t)$  with spectrum  $I_{\text{fund}}(\omega)$  and spectral phase  $\varphi_{\text{fund}}(\omega)$ , and second harmonic pulse  $E_{\text{SH}}(t)$  with spectrum  $I_{\text{SH}}(\omega)$  and spectral phase  $\varphi_{\text{fund}}(\omega)$  delayed in time (with delay  $\tau$ ) are spatially overlapped, fringes in the spectral domain will be visible. The phase of the fringe pattern  $S(\omega)$  will be depending on the carrier-envelope phase  $\phi$  of the fundamental pulse. This is

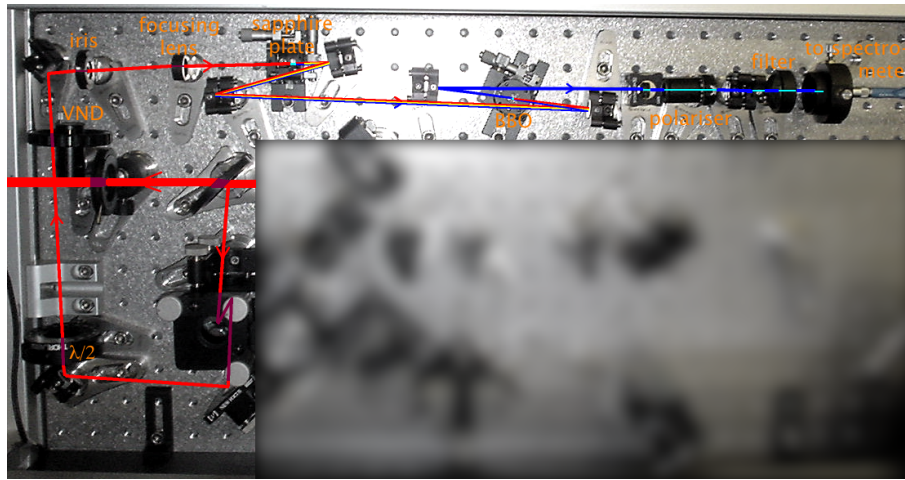


Figure 2.4: Photograph of the collinear f-to-2f interferometer used for measurement and compensation of carrier-envelope phase drifts in the amplifier. The variable neutral density filter (VND) is used to tune the input energy to the interferometer. The  $\lambda/2$  plate is used to optimise the second harmonic yield in the BBO crystal. The iris before the interferometer is used to optimise the beam parameters for better measurement quality. The pulses are spectrally broadened in a 2 mm thick sapphire plate. The polariser cube is used to overlap and balance the fundamental and second harmonic polarisation, allowing to maximise the fringe visibility. The blue filter is used to suppress the wavelength components far outside the wavelength range of interest.

easily seen mathematically:

$$E_{\text{fund}}(t) = \frac{1}{2\pi} \int_{-\infty}^{+\infty} \sqrt{I_{\text{fund}}(\omega)} \exp[i(\varphi_{\text{fund}}(\omega) - \omega t + \phi)] d\omega + cc \quad (2.2)$$

$$E_{\text{SH}}(t) = \frac{1}{2\pi} \int_{-\infty}^{+\infty} \sqrt{I_{\text{SH}}(\omega)} \exp[i(\varphi_{\text{SH}}(\omega) - \omega(t + \tau) + 2\phi)] d\omega + cc \quad (2.3)$$

$$S(\omega) = I_{\text{fund}}(\omega) + I_{\text{SH}}(\omega) + 2\sqrt{I_{\text{fund}}(\omega)I_{\text{SH}}(\omega)} \cos(\varphi_{\text{SH}}(\omega) - \varphi_{\text{fund}}(\omega) + \omega\tau + \phi) \quad (2.4)$$

In figure 2.4 a photograph of the collinear f-to-2f interferometer for measuring the carrier-envelope phase after amplification is shown. The beam path has been drawn in the figure for illustrative purposes. The spectral broadening of the pulses is very sensitive to the intensity of the input pulses, and can be varied with a neutral density filter. The quality of the measurement can be improved by changing the focusing parameters of the input beam, therefore an iris is placed before the interferometer. The second harmonic of the long wavelength part of the spectrum is frequency doubled in a type-I BBO crystal, therefore the second harmonic signal polarisation is perpendicular to the polarisation of the fundamental spectrum. In order to see spectral fringes, the second harmonic and the fundamental need to be in the same polarisation, therefore a rotatable polariser is put after the second harmonic crystal. This can be used to balance the fundamental and second harmonic fields as well, allowing to maximise the contrast of the fringes. A blue filter is placed in front of the spectrometer, in order to suppress the energy far outside of the wavelength range of interest.

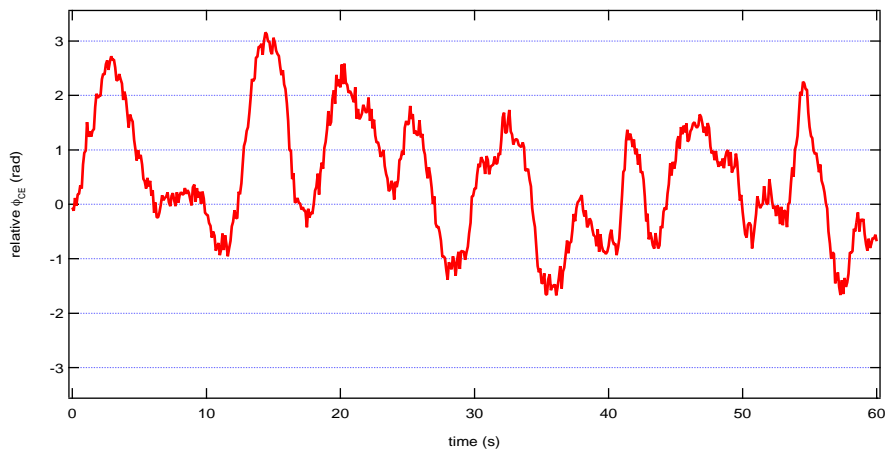


Figure 2.5: Measurement of the carrier-envelope phase drift after amplification. As can be clearly seen, the carrier envelope phase drift from pulse to pulse is very small, the phase drifts over a few radians in several seconds, thus over several thousands of laser pulses.

The carrier-envelope phase stability of the pulses is preserved during amplification and re-compression. However, a small, slow phase drift can be observed, as can be seen in figure 2.5. This phase drift can be compensated for with two different approaches. The first approach is to force the phase stabilisation of the oscillator to change the carrier-envelope phase of the pulses seeded into the amplifier. This can be done by changing an offset signal-value in the locking electronics. This in fact causes a controlled phase-slipping of the oscillator pulses. The second approach is based on the phase shift introduced by dispersive material (or simply dispersion) in the beam path. For example by simply changing the amount of glass in the beam path by a few micrometers, the carrier-envelope phase can be changed significantly.

## 2.2.2 Compensation of the carrier-envelope phase drift

As mentioned, the phase drifts over a few radians in several thousands of laser pulses, and can therefore be considered as just a slow drift of the phase. This slow drift originates from different sources, the most prominent of which are energy fluctuations of the pump laser and the seed oscillator, and beam pointing fluctuations. Minimising these fluctuations helps minimising the carrier-envelope phase drift [57]. Normally the drift of the carrier-envelope phase is slow enough that it is possible to compensate for it by means of a slow feedback loop. In appendix A the computer program for the feedback is discussed in more detail. Here a comparison of the two aforementioned approaches to implement this feedback will be discussed.

As already mentioned, the first approach makes use of a feature of the electronics for stabilising the phase drift of the seed oscillator. The phase drift of the oscillator is stabilised to be exactly  $\pi/2$  between two pulses, ensuring that every fourth pulse coming from the oscillator to have the same phase. This is done by locking the beat signal to a quarter of the oscillator repetition rate. A frequency can be locked to another frequency with a fast 'up-down' counter, by letting the counter increment with every period of the reference frequency, and decrement with every period of the frequency to be stabilised. When the output value of the counter is filtered with a low-pass filter, an error signal is generated by comparing this value with a reference value. By changing the reference value, a controlled phase shift,

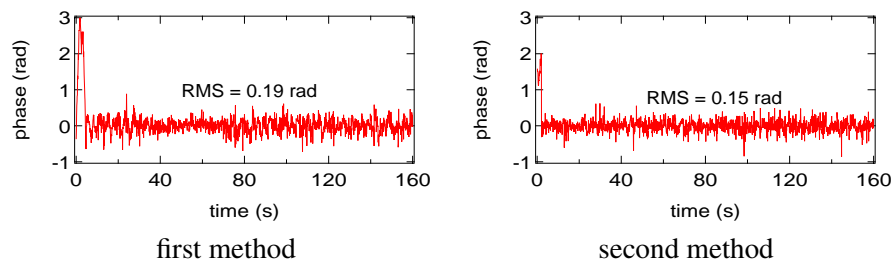


Figure 2.6: Comparison of the two methods to compensate for the slow drift. The two traces were recorded within a very short period of time, ensuring that all other experimental conditions have not changed. One can clearly see that the second method results in a smaller RMS phase noise. The reason for this is that the feedback with the first method could not be made stronger without influencing the oscillator stability.

proportional to the change of the reference value is introduced. The main advantage of this approach is that no additional degree of freedom needs to be added to the amplifier in order to compensate for the carrier-envelope phase drift observed. However, this method exploits an additional degree of freedom of the oscillator phase lock electronics, potentially decreasing the quality of the lock. This decrease in quality of the lock can in fact be observed, and eventually causes the lock to break earlier than in the undisturbed case.

The second approach makes use of the carrier-envelope phase shift caused by material dispersion. In figure 1.5 on page 12 the implementation of this approach in a chirped-pulse amplifier system is shown. In the case of fused silica as a dispersive material and pulses with a central wavelength of 800 nm, as is the case for the Ti:sapphire laser system used, addition of approximately  $50\mu\text{m}$  of material, introduces a carrier-envelope phase shift of  $2\pi$ , without noticeably lengthening the pulse. This approach can be implemented by several ways, for example by introducing a pair of Brewster-prisms in the pulse stretcher before amplification, or by transversally shifting one of the prisms in the prism compressor. The latter implementation is of course the most elegant, since no additional optical components need to be introduced, and strictly taken, not even a degree of freedom is added to the amplifier, since the material dispersion in the prism compressor is already used for optimising the pulse duration. Transversally shifting one of the prisms over a few micrometers will not affect the pulse duration, but it strongly modifies the carrier-envelope phase. In case of grating compressors and stretchers, the grating separation can be used for tuning the dispersion, so putting one of the gratings on a piezo-actuated translation stage [86] would allow changing the carrier-envelope phase the same way it does when changing the prism-insertion.

In figure 2.6 the compensation of the slow drift with the two methods is compared. The two traces were recorded both within a short period of time, ensuring that all other experimental conditions have not changed significantly. The second method features a smaller RMS phase noise, 0.15 rad versus 0.19 rad for the first method. The reason that the phase noise in the conventional case is larger originates from the fact that the feedback could not be made stronger without degrading the oscillator stability significantly.

Another important advantage of the new method is, because it operates independent of any other feedback, that it can be applied multiple times in one system. Since it does not necessarily need to be implemented in the compressor, this approach can be easily adopted to amplifier chains. In fact this new method is the only possible way to implement carrier-envelope phase



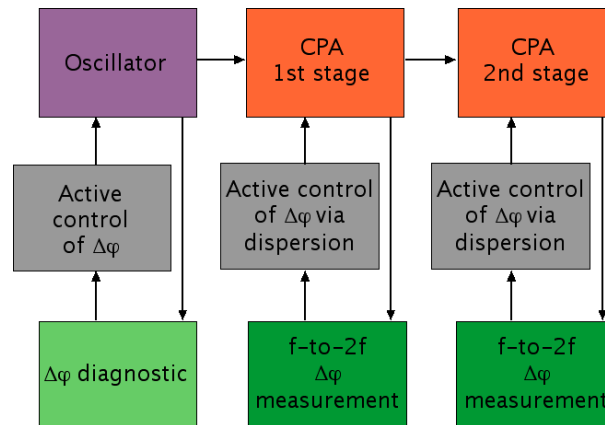


Figure 2.7: Schematic of the implementation of the second carrier-envelope phase stabilisation method for a multiple-stage chirped-pulse amplifier system. A fast feedback loop is applied to stabilise the phase of the oscillator. Independent slow feedback loops are implemented to phase-stabilise subsequent amplification stages. Usually, pulses are not compressed in between different amplification stages, but it is enough to compress only a small fraction of the output to allow the f-to-2f measurement of the phase drift, for example with chirped mirrors.

stabilisation for systems consisting of an amplifier chain. In figure 2.7 this is drawn schematically. This approach therefore allows to scale the control of the carrier-envelope phase to ultrashort pulses to the petawatt regime.

## 2.3 Mini stereo ATI – Absolute phase control

### 2.3.1 Improving the control over the carrier-envelope phase

Though the f-to-2f interferometer can be used for compensating the carrier-envelope phase drift in the amplifier, it does not measure the carrier-envelope phase itself. From eq. 2.4 on page 27 it can be seen that there are still two unknown parameters, that give rise to an unknown offset to the phase measured with the f-to-2f interferometer. As long as one does not need to do any alignment tasks on the laser, the success of experiments like the atomic transient recorder [68], the direct measurement of light waves [69] and the control of electron localisation in dissociation of  $D_2^+$  with the carrier-envelope phase of few cycle pulses [66] show that this unknown parameters are kept constant. In general it needs not be the case that these parameters stay constant over long periods of time, when there are slow intensity and beam pointing drifts, and more important, after alignment of the system, these parameters are very likely to have changed [62]. For experiments that need carrier-envelope phase stable pulses over a long period of time, a method that reproducibly measures the carrier-envelope phase is of great importance, allowing one to exactly reproduce the carrier-envelope phase at the experiment even after alignment of the laser system. A method that is very suitable for this, is based upon above-threshold-ionisation. A more detailed study of above threshold ionisation will be described in chapter 4. A first demonstration of this method was done with spectrally resolved detection of electrons in two directions in the plane of laser polarisation [59, 71, 87]. Here a simplification of this implementation will be described, based on [62],



in which the number of electrons flying in two opposing directions in the plane of the laser polarisation is used to measure the carrier-envelope phase.

### 2.3.2 Above-threshold-ionisation

At high intensities, above-threshold-ionisation is a prominent effect in photoionisation [88]. More photons than necessary for ionisation can be absorbed, and accordingly, photoelectrons with a kinetic energy of many times the photon energy can be observed. In the strong-field limit [89], this can be explained in the same way as high-order harmonic generation (see Chapter 3) and non-sequential double ionisation, with a simple semi-classical model. The so-called three step model explains the mechanism as follows: With a strong laser field present, at some time  $\tau_0$ , an electron can tunnel through the barrier created by the combination of the laser field and the coulomb potential, and is subsequently accelerated away from its parent ion by the laser field. When the field changes its sign, the electron can be driven back to its parent ion, where it may scatter elastically or inelastically. And again the electron can be accelerated further by the laser field.

The rescattering mechanism creates a plateau like structure in the electron kinetic energy spectra, breaking the nearly exponential decrease in number of electrons with kinetic energy at low kinetic energies. Classical calculations yield a maximum kinetic energy for direct (non-scattered) electrons of  $2U_p$ , and  $10U_p$  for the elastically rescattered electrons. The ponderomotive potential or energy  $U_p = e^2 E^2 / 4m\omega_0^2$  with  $e$  and  $m$  the electron charge and mass respectively,  $E$  the maximum electric field amplitude of the laser in V/m and  $\omega_0$  the driving laser frequency. Because of the high nonlinearity of above-threshold-ionisation, the electron kinetic energy distribution, and even the spatial distribution of the electrons, is expected to be very sensitive to the carrier-envelope phase of a few-cycle pulse [87].

### 2.3.3 The mini stereo ATI apparatus

The mini stereo ATI operates with about 30- $\mu$ J pulses, corresponding to less than 10% of the available pulse energy from the 400- $\mu$ J sub-5-fs laser system shown in figure 1.5 on page 12. This makes the device suitable for monitoring and/or controlling the carrier-envelope phase during experiments. With a variable aperture iris the focal intensity inside the apparatus can be controlled. The mini stereo ATI itself (shown in fig 2.8) consists of two compartments, an inner interaction chamber, and a surrounding detection chamber. The arrangement fits into a standard CF63 cube, which shrinks the device to about 10% of the size of the original apparatus used in [59] and [71]. Only one small turbomolecular pump and a membrane pump are necessary for the vacuum system.

The detection and interaction chamber are differentially pumped using the sealing gas connection (or Hohlweck-port) of the turbo pump (Pfeiffer TMU 071 P) for the relatively high pressure ( $10^{-3}$  mBar) interaction chamber, while maintaining a pressure of  $5 \cdot 10^{-6}$  mbar in the detection chamber with the turbo pump, which is necessary to safely operate the multi channel plates.  $\sim 30$ - $\mu$ J horizontally polarised pulses are focused with a spherical mirror of 15 cm focal length into the interaction region. At 2 mm to the left and right of the focus, 0.5 mm holes allow electrons resulting from strong field ionisation to leave the interaction chamber and to enter the detector chamber. An adjustable blocking potential (0 – –35 V) can be applied within these holes, in order to select only the higher energy rescattered electrons, which show a stronger phase dependence compared to low energy electrons [59]. In this experiment, a blocking potential of –25 V was applied to detect only electrons with a kinetic

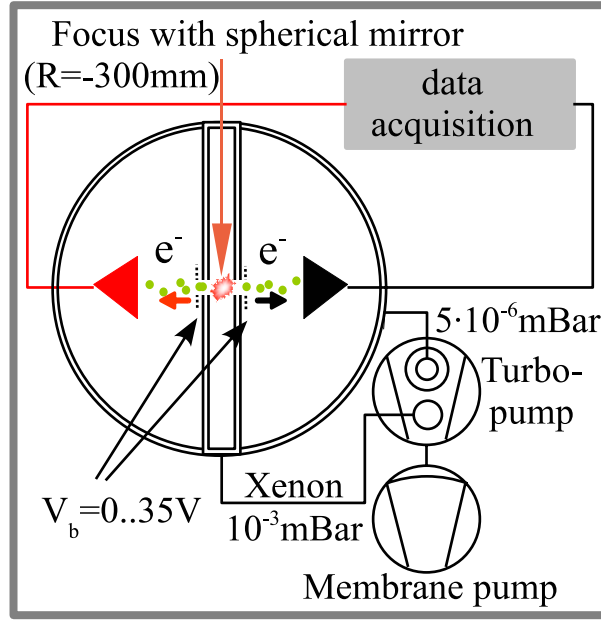


Figure 2.8: Schematic of the mini stereo ATI apparatus.

energy of  $> 25\text{ eV}$ . At 2 cm from each exit hole a commercial dual micro channel plate detector (Hamamatsu F4655) is placed so that it faces the other one. These detectors are operated in reversed bias mode to allow for electron detection.

The voltage divider and the coupling capacitors for the detectors are placed inside the vacuum system on printed circuit boards, electrostatically well shielded from the electron drift region. The signals from the microchannel plates are measured shot by shot with an 8 channel sample and hold card (Becker&Hickl SHM180) that is connected to a computer and online evaluated with a LabVIEW program. The features of this program are described in appendix A.

### 2.3.4 Carrier-envelope phase retrieval

Previous measurements concentrated of the carrier-envelope phase based on the principle of above threshold ionisation on measuring the spatio-spectral distribution of the emitted electrons [59, 60]. The experimental data by Paulus *et al.* [59] and the theoretical treatment by Chelkowski *et al.* [90] show that the asymmetry as a function of the carrier-envelope phase in the number of electrons emitted can be described with a sin-function. The spectral information is necessary in order to unambiguously derive the carrier-envelope phase from a single measurement, though a series of measurements with a known phase-shift lifts the ambiguity when only the number of electrons is measured. No asymmetry is expected for pulses with a carrier-envelope phase  $\phi_0 \approx -0.3\pi$ . Maximal asymmetry is expected for pulses with a carrier-envelope phase of  $\phi_M \approx 0.2\pi$ . With the signals from the mini stereo ATI the carrier-envelope phase  $\phi$  is found as:

$$\phi = \arcsin \left( A \frac{N_{\text{left}} - N_{\text{right}}}{N_{\text{left}} + N_{\text{right}}} \right) + \phi_0 \quad (2.5)$$

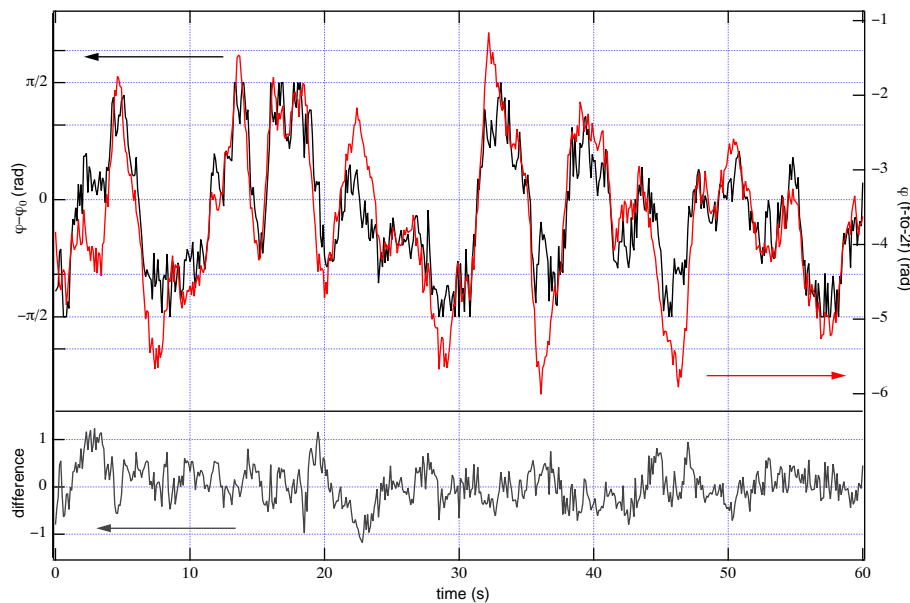


Figure 2.9: Comparison of the slow phase drift measured with the f-to-2f interferometer (red) and the stereo ATI (black). The difference between the two measurements is shown in the lower panel. Most of the time both measurements agree. Disagreement of both measurements can be explained by intensity fluctuations and beam pointing instabilities. Baluška *et al.* [55] measured the phase noise added in the hollow fibre and estimated it to be between 0.08 and 0.14 rad depending on the pressure in the hollow fibre.

with  $N_{\text{left}}$  the number of electrons flying to the left,  $N_{\text{right}}$  the number of electrons flying to the right and  $A$  a correction factor that is to be chosen such that the argument of the arcsin-function is 1 or  $-1$  at the maximal asymmetry. From [90], it can be clearly seen that  $A$  strongly depends on the pulse duration and the pulse intensity. The asymmetry gets stronger for shorter pulses, and gets weaker for more intense pulses. However, weaker pulses do not guarantee a better measurement, since the total number of measured electrons gets smaller as well, decreasing the quality of the measurement. According to [59] the asymmetry can be enhanced by selecting only electrons with higher kinetic energies. Of course, here as well a trade-off needs to be made between the decrease in the number of detected electrons and the increase of the asymmetry.

### 2.3.5 Carrier-envelope phase control with the mini stereo ATI

First of all, for calibration a comparison needs to be made between the phase retrieved with the mini stereo ATI device and the phase-drift measured with the normal f-to-2f interferometer. For this the carrier-envelope phase stabilisation of the oscillator is activated, but no slow feedback is applied. As a result of this, both the f-to-2f interferometer and the mini stereo ATI should measure a slow drifting phase. From equation 2.5 one can understand that the phase retrieved with the mini stereo ATI will always be a value between  $\pm\pi/2 + \phi_0$ .

In figure 2.9 the phase drift measured with the f-to-2f interferometer is compared with the phase retrieved with the mini stereo ATI. The mini stereo ATI accumulated data over 300 laser shots (100 ms) for each point. In the lower panel the difference of two measured

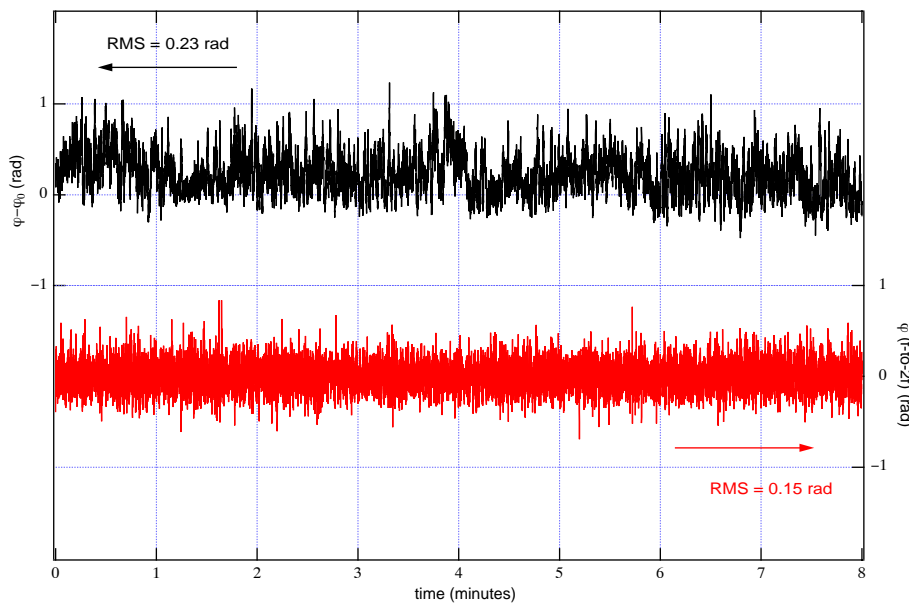


Figure 2.10: Out-of-loop phase measurement with the mini stereo ATI (black). The in-loop measured phase with the f-to-2f interferometer is shown in red, with an RMS of 0.15 rad. The out of loop measured RMS is 0.23 rad.

traces is shown, where the phase measured with the f-to-2f interferometer is being shifted by a constant phase-offset and then restricted between  $\pm\pi/2$  just as the mini stereo ATI restricts the retrieved phase value. The two phase measurements agree quite well in most cases. On a few occasions there is a disagreement between the two measurements. This disagreement can be explained with amplitude-to-phase noise in the f-to-2f interferometer and/or hollow fibre, and with beam pointing instabilities to the hollow fibre, which leads to fluctuations of the beam profile and pulse duration after the hollow fibre. To confirm the origin of the disagreement of the two phase measurements, a series of measurements may be carried out, including out-of-loop measurements with a second f-to-2f interferometer. Phase noise added by the hollow fibre was measured by Baltuška *et al.* [55] using linear interferometry, and estimated to be between 0.08 and 0.14 rad depending on the pressure in the hollow fibre.

When the carrier-envelope phase of the amplifier is stabilised with a slow feedback from the f-to-2f interferometer, a phase measurement with the mini stereo ATI can be used as an out-of-loop measurement to determine the quality of the phase-lock of the amplifier. In figure 2.10 the result of this measurement can be seen. The RMS phase noise measured in-loop with the f-to-2f interferometer was 0.15 rad, while the RMS phase noise measured out-of-loop with the mini stereo ATI was 0.23 rad.

Since the time needed to collect data for one point with the mini stereo ATI is just 3 times longer than the response time of the f-to-2f interferometer, it may be possible to use the mini stereo ATI directly to stabilise the phase of the laser. This has been tried, and the result can be seen in figure 2.11. After 8 minutes, the error signal was inverted to verify that the mini stereo ATI can really control the absolute phase. The inversion of the error signal should result in a  $\pi$  phase shift, since the feedback quickly pushes the phase away from the point where it locked, and then locks again at the next zero crossing of the asymmetry. This was confirmed by the out-of-loop phase measurement with the f-to-2f interferometer. The RMS of the in-

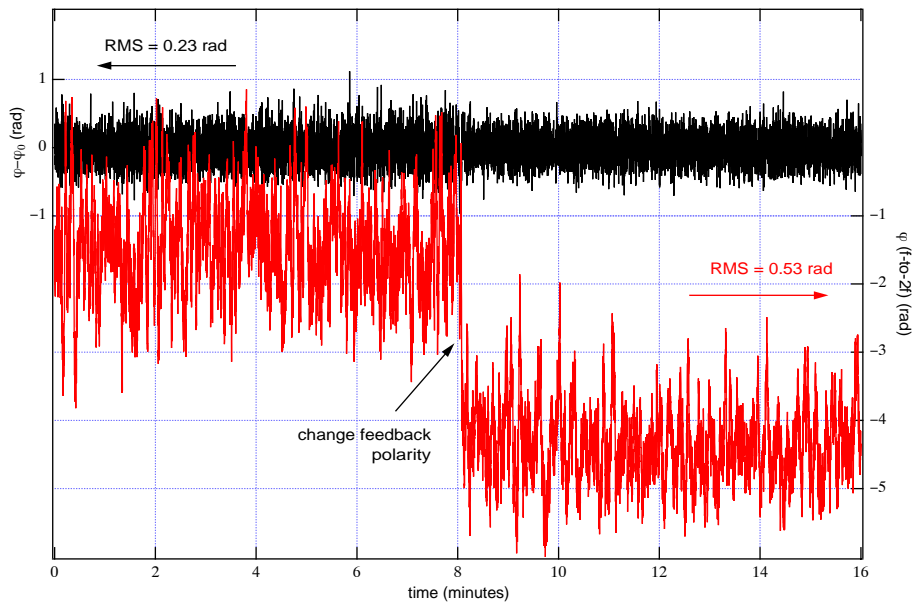


Figure 2.11: Measurement of the phase evolution while the slow feedback was provided by the mini stereo ATI. The retrieved phase with the mini stereo ATI is shown in black. After 8 minutes the error signal was inverted, yielding a  $\pi$  phase shift, as can be seen in the out-of-loop measurement with the f-to-2f interferometer (red). The RMS of the ATI measurement after the inversion of the error signal was 0.23 rad, and the RMS of the out-of-loop measured phase with the f-to-2f interferometer was 0.53 rad.

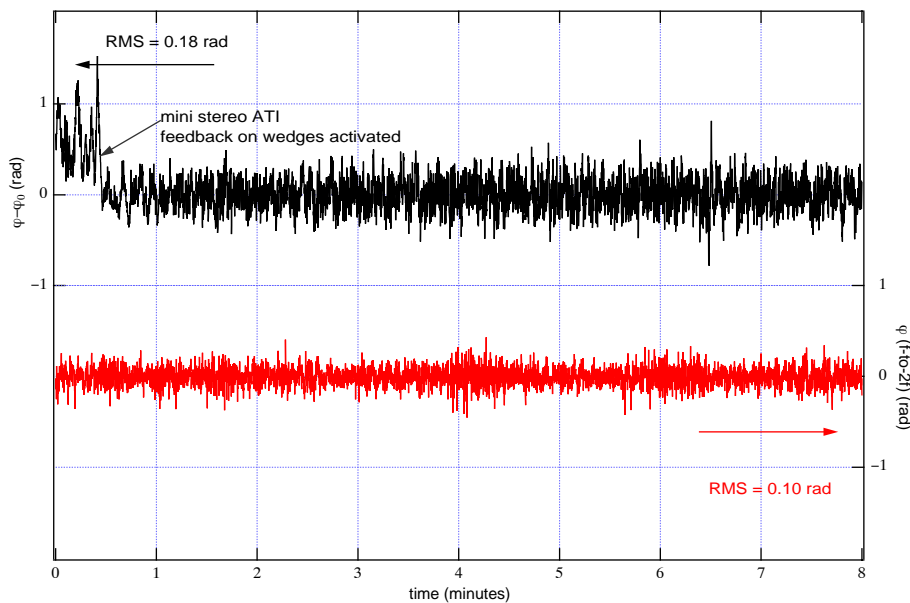


Figure 2.12: Measurement of the phase evolution while the f-to-2f interferometer (phase shown in red) was used for active feedback on the amplifier, and the mini stereo ATI (phase shown in black) was used to control the phase by means of a pair of wedges after the hollow fibre. Both phase measurements are now in-loop. The RMS of the phase measured with the mini stereo ATI was 0.18 rad, and the RMS of the phase measured with the f-to-2f interferometer was 0.10 rad.

loop measured phase was 0.23 rad, and the out-of-loop measured RMS after the inversion of the error signal was 0.53 rad.

Though the mini stereo ATI could directly stabilise the phase of the laser system, the RMS of the out-of-loop measured phase in figure 2.11 and 2.10 suggests that the quality of the lock was better when the f-to-2f interferometer was used for active feedback. The reason for this is mainly that the signal-to-noise ratio of the f-to-2f measurement is much better. The signal to noise ratio of the mini stereo ATI measurement can of course be reduced by increasing the number of laser shots accumulated for one point, but then the mini stereo ATI can not be used for direct feedback any more. A more useful approach to control the phase at an experiment with the mini stereo ATI would be to stabilise the phase of the amplifier with the f-to-2f interferometer, and provide an additional feedback based on the mini stereo ATI measurement on a pair of wedges.

Stabilising the carrier-envelope phase of the amplifier with the f-to-2f interferometer and then using the measurement with the mini stereo ATI to control a pair of wedges is of course expected to yield an even better controlled phase than in any of the two cases discussed before. This is confirmed by the measurement shown in figure 2.12. The RMS of the in-loop measured phase with the mini stereo ATI was 0.18 rad, and the RMS of the in-loop measured phase with the f-to-2f interferometer was 0.10 rad. Summarising, when the phase of the amplifier is locked with the f-to-2f interferometer only, the RMS phase noise is measured to be 0.23 rad. When in addition to this the mini stereo ATI is used to control the carrier-envelope phase by means of a pair of wedges, the RMS phase noise is reduced to 0.18 rad. Previous measurements on the phase stability after compression estimated the phase noise

to be smaller than  $\pi/10$  [59, 69, 71], which is confirmed by this measurement over a larger bandwidth.





## Chapter 3

# High-harmonic generation with ultrashort pulses

In this chapter one of the main motivators for the work presented in the two previous chapters will be shortly discussed. A more thorough discussion of the respective experiments can be found in the (future) theses by other colleagues that worked on those experiments [91, 92].

### 3.1 Upscaling the energy of coherent extreme ultraviolet radiation

#### 3.1.1 Motivation for upscaling the energy of extreme ultraviolet radiation

For many applications, coherent extreme ultraviolet (XUV) or x-ray radiation with a high repetition rate is of great interest. Of particular interest is radiation in the water window, that is, in the wavelength range between 2.33 nm (Oxygen K-absorption-edge) and 4.37 nm (Carbon K-absorption-edge) [93, 94]. In this wavelength range, carbon (and thus carbon-containing biological objects) absorbs radiation efficiently, and water is relatively transparent. Extension of the photon energies beyond the water window is of interest as well, since it will allow generating shorter x-ray pulses. Most recent advances have been made with lasers at kilohertz repetition rates [95, 96]. At 100 kHz repetition rate Ti:Sapphire laser amplifier system operating at 800 nm XUV radiation up to the 41st harmonic (wavelength slightly below 20 nm) was reported [97].

Recently a method for generating harmonic radiation at even higher ( $\sim 100$  megahertz) has been demonstrated [36, 37, 98, 99], allowing for high resolution spectroscopy with XUV radiation in the frequency domain. The shortest wavelengths reported up to now with this method are longer than 50 nm, far away from the water window.

#### 3.1.2 Theoretical considerations

Several papers have treated the generation and scaling of high harmonic radiation with ultrashort pulses [89, 100–107]. All theoretical treatments agree with the phenomenological law for the scaling of the highest photon energy  $\hbar\omega_{max}$  achievable

$$\hbar\omega_{max} = I_p + 3.17U_p \quad (3.1)$$

with  $I_p$  the ionisation potential of the medium used for harmonic generation and  $U_p$  the ponderomotive potential or quiver energy of a free electron in a given laser field. Generally the

ponderomotive potential is given as follows [93]:

$$U_p = e^2 E^2 / 4m\omega_0^2 \quad (3.2)$$

with  $e$  and  $m$  respectively the charge and mass of the electron,  $E$  the (maximum) amplitude of the electric field, and  $\omega_0$  the driving laser frequency. Thus, one can easily see that the highest photon energy increases linearly with the laser peak intensity, and quadratic with the wavelength of the driver laser.

A different expression for the ponderomotive potential gives some additional insight for the choice of the medium to be used for the generation of the highest photon energies [94]:

$$U_p = 9.33 \times 10^{14} I_s \lambda^2 \quad (3.3)$$

$$\hbar\omega_{max} = I_p + \frac{0.5 I_p^{3.5} \lambda^2}{\{\ln(1.72\tau 3^{2n^*-1} G_{lm} I_p) / [-\ln(1-p)]\}^2} \quad (3.4)$$

with all energies in eV.  $I_s$  is the saturation intensity for ionisation in W/cm<sup>2</sup>,  $\lambda$  the driver laser wavelength in  $\mu\text{m}$  and  $\tau$  the pulse FWHM in fs.  $p$  is the ionisation probability for defining the saturation intensity (chosen to be 0.98 in [94]),  $n^*$  is the effective principle quantum number, varying between 0.74 for helium and 1 for xenon.  $G_{lm} = (2l+1)(l+|m|)!/6^{|m|}|m|!(l-|m|)!$ , where  $l$  and  $m$  are the orbital and magnetic quantum numbers of the outermost electron.  $G_{lm} = 1$  for helium, and 3 for all other noble gases.

From equation 3.3 and 3.4 it can be seen that using a gas with higher ionisation potential as a nonlinear medium will allow producing higher photon energies. It can be seen also, that shorter pulse durations allow for higher photon energies.

This can be qualitatively explained with the so called three-step-model in mind [3, 89, 105]. Near a field maximum, the barrier formed by the combination of the coulomb potential of the atom and the laser field is suppressed so much that the least bound electron can easily tunnel through this barrier, and subsequently be accelerated by the laser field. After about three quarter of an optical period, the electron can recombine with its parent ion, under emission of an energetic photon. This is shown graphically in figure 3.1.

Gases that ionise more difficult, need higher field strengths to ionise, and therefore from the beginning of the process, electrons will be accelerated more, yielding higher photon energies. The high-harmonic radiation is emitted at the moment that the electron that was removed from the atom recombines with its parent ion (or is scattered on its parent ion). The moment of recombination is roughly at a zero crossing of the optical electric field, yielding harmonic bursts separated by half a period of the driver field. Since the probability of recombination is quite small, the highest photon energy achievable is determined by the electric field in the half-cycle immediately after the electron starts moving away from its parent ion. The same arguments show why shorter pulses can generate the highest photon energies with the highest photon flux, since the pulse envelope varies faster, a smaller fraction of the atoms is ionised before the strongest field strength is reached, thus increasing the number of atoms taking part in the process when the field strength is highest.

### 3.1.3 Experimental considerations

For generating high harmonics phase matching, or avoiding phase-mismatch, plays a key role. In addition to that, absorption of the high-harmonic radiation by the generating medium plays a major role as well [103]. In [108] an extensive study on the influence of the experimental

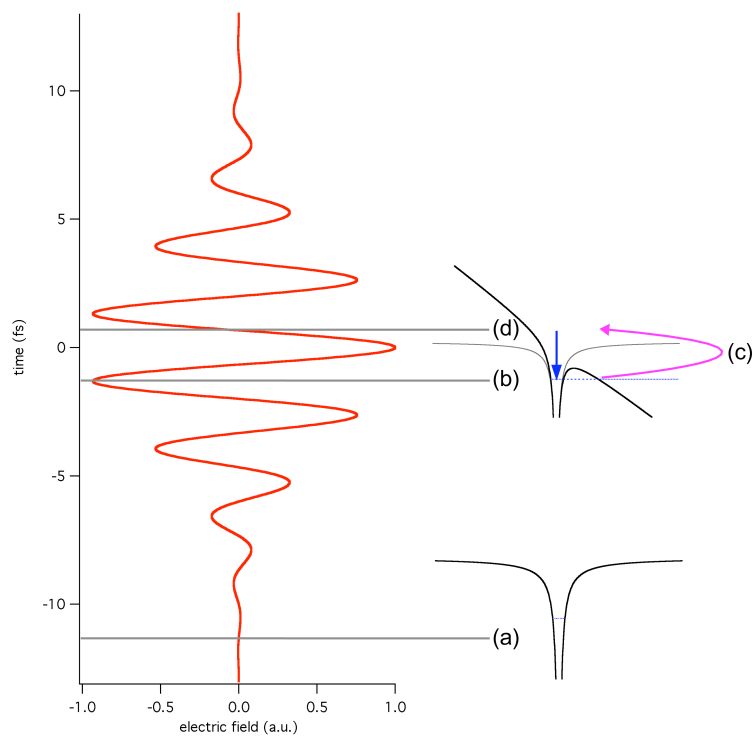


Figure 3.1: Graphic representation of the the three step model [3, 89, 105].

(a) The atomic potential unperturbed.

(b) Near an electric field maximum the coulomb potential is suppressed so much that an electron can fly away, and (c) subsequently be accelerated in the optical electric field.

(d) When the electron recombines with its parent ion, an energetic photon will be emitted.

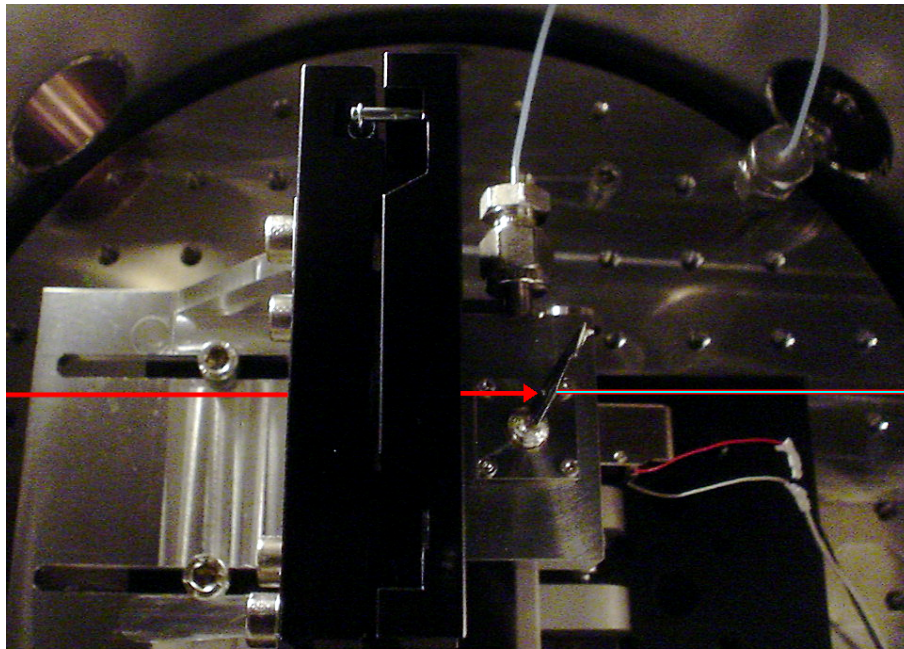


Figure 3.2: Photograph of a the target for harmonic generation at the AS1 beamline at MPQ in Garching. A hole on both sides of the tube is drilled in the target by the laser itself. This ensures a minimal gas flow from the target, and at the same time highest intensity in the gas medium. For clarity the laser beam path was drawn in.

conditions on the harmonic yield is presented. By tuning the pressure of the target gas, the de-phasing length, and thus the phase matching, and the absorption length can be matched. By carefully designing the harmonic generation target, one can take advantage of this mechanism.

In figure 3.2 a photograph of the harmonic target at the AS1 beamline at MPQ in Garching is shown. On both sides of the tube a hole is drilled by the driver laser itself, thus ensuring optimal size of the holes. The gas flow from the target stays small, and the laser intensity in the interaction region is high. Because of the small gas flow, a good background pressure ( $10^{-2}$  mbar or better) can be maintained, minimising absorption of the harmonic radiation in the background gas.

In addition to tuning the pressure to match the de-phasing and absorption length, the best phase matching is achieved when the harmonic target is slightly behind the focus. This takes optimal advantage of the geometrical phase shift of the driver laser beam [95]. Taking all those considerations into account, the highest laser driven coherent x-rays generated had maximum photon energies up to 1.3 keV [96].

Another important issue are the geometric properties of the emitted harmonic radiation. The spatial profile of the emitted radiation is strongly dependent on the position of the harmonic generation target relative to the driver lasers focus [102, 109]. Just as the harmonic yield improves when the target is behind, the spatial profile improves as well. Since typically the laser beam is focused relatively loose, in the region where the harmonic radiation is produced the driver field is close to a plain wave. As a result of this, the divergence of the harmonic radiation will be determined by simple diffraction properties [96, 110], and is much smaller than the divergence of the driver laser beam.

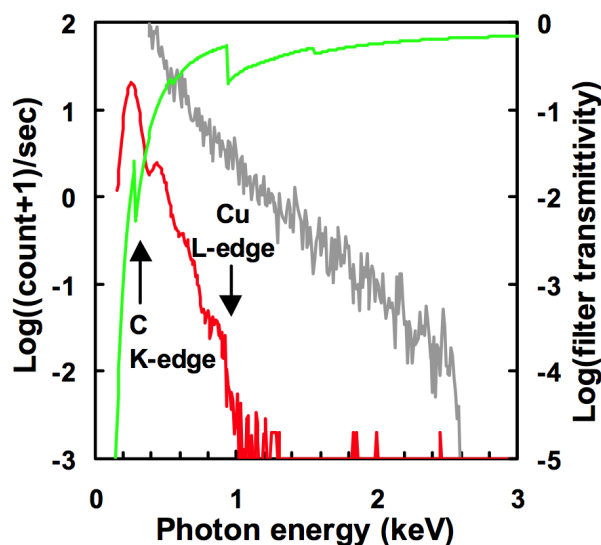


Figure 3.3: Measurement of the harmonic radiation generated with 1-mJ, 5-fs pulses focused loosely in a helium gas jet. The spectrum (red) is calibrated using a set of filters containing a 300 nm thick carbon-containing filter, a 100 nm thick aluminium filter and a 100 nm thick copper filter. The overall filter transmission is shown in green. The gray line represents a theoretical calculation of radiation emitted by individual He atoms exposed to 5-fs pulses with an intensity of  $1.4 \times 10^{16} \text{ W/cm}^2$ . Image taken from Seres *et al.* [96].

### 3.1.4 Calibrating and measuring soft-x-ray photon energies

For the detection of generated harmonic radiation spectrum it is necessary to calibrate the device used for this purpose. Generally a spectrometer consisting of a reflecting grating with a CCD camera sensitive in the spectral region of interest, a multi channel plate detector with a phosphor screen or a photo-multiplier with a narrow entrance slit is used. Since for the highest photon energies the diffraction angle is very small, it is very important to efficiently block the low frequency radiation, ie. the fundamental and low harmonics, such that the zeroth order of this radiation does not cause too much background. Another consequence of the very small diffraction angle for the highest photon energies is that the uncertainty when calculating the photon energy from this angle gets unacceptable. So, another method for calibrating the wavelength or energy scale must be used. For harmonics generated with many cycle driver fields, one can count the harmonic peaks in order to determine the energy, but again for very high photon energies the individual peaks may not be resolvable. For harmonics generated with few cycle driver fields, the highest photon energies may even not coincide with odd harmonics of the driver central frequency.

For the calibration of the spectrometers wavelength scale, it is possible to use absorption features of different materials. For many materials these features are well known, making the calibration very accurate [93–96, 108]. In figure 3.3 a measured spectrum showing photon energies extending up to 1.3 keV is shown. The energy axis is clearly calibrated using a set of filters [111].

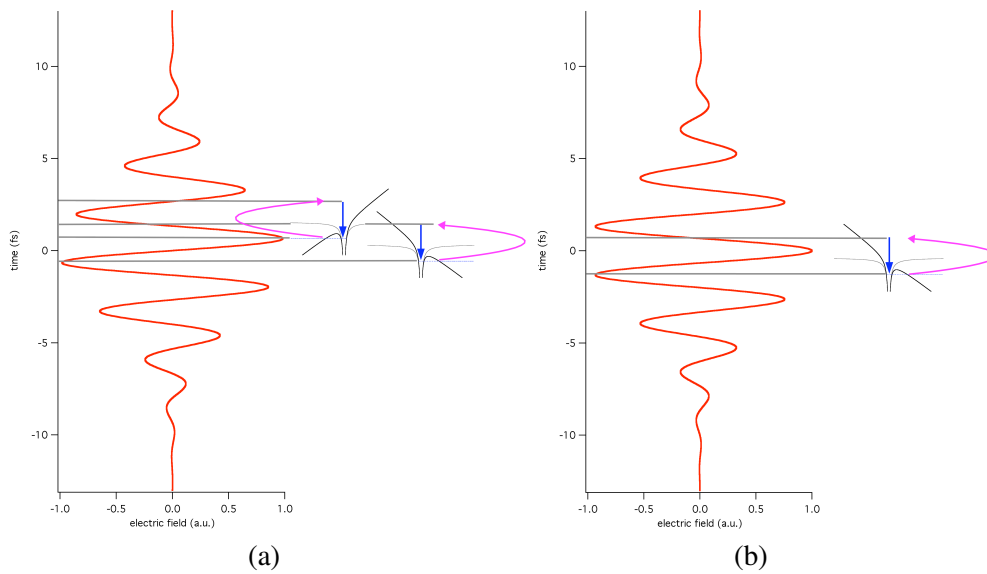


Figure 3.4: Graphic representation of the three-step-model and single attosecond pulse generation.

(a) In the case of a sine-like driver pulse, two half-cycles produce the highest photon energy, so two attosecond photon bursts with the same photon energy are emitted.

(b) In the case of a cosine-like driver pulse, only one half-cycle produces the highest photon energy, and only one attosecond burst with this photon energy is emitted.

## 3.2 Generation of single attosecond soft-x-ray pulses

As mentioned in the beginning of the previous section, one of the motivators for upscaling the photon energy of harmonic radiation is the generation of ever shorter isolated attosecond (soft)-x-ray pulses. At the moment state-of-the-art single attosecond pulses have photon energies of roughly 91 eV [68, 69, 112, 113]. This number clearly is not the highest photon energy available, but it is simply set by the availability of good x-ray optics.

To generate soft-x-rays at 91 eV photon energy, it is clear that few-cycle pulses are no prerequisite since this has been achieved with much longer pulses [114, 115]. However, to generate an isolated pulse with this energy, driver pulses shorter than 5 fs are an absolute requirement. More than that, it is imperative that of this sub-5-fs pulse only one half-cycle can generate such photon energies, as can be easily understood when considering the simple picture of the three-step-model and the graphic representation in figure 3.4. So, control over the carrier-envelope phase, as discussed in Chapter 2 is the second technical prerequisite for single attosecond pulses besides having few-cycle driver pulses [68, 69].

### 3.2.1 The optics for single attosecond soft-x-ray pulses

As mentioned, state-of-the-art single attosecond pulses have a photon energy of roughly 91 eV, set by the availability of x-ray optics. More precise, by the availability of good x-ray mirrors to be used at near-normal incidence. Molybdenum-silicon (Mo/Si) multilayer mirrors are state-of-the-art soft-x-ray optics [116, 117], with the highest reflectivity reported to date 71.05 % at 12.73 nm [118] for reflection at near-normal incidence. However, the reflective

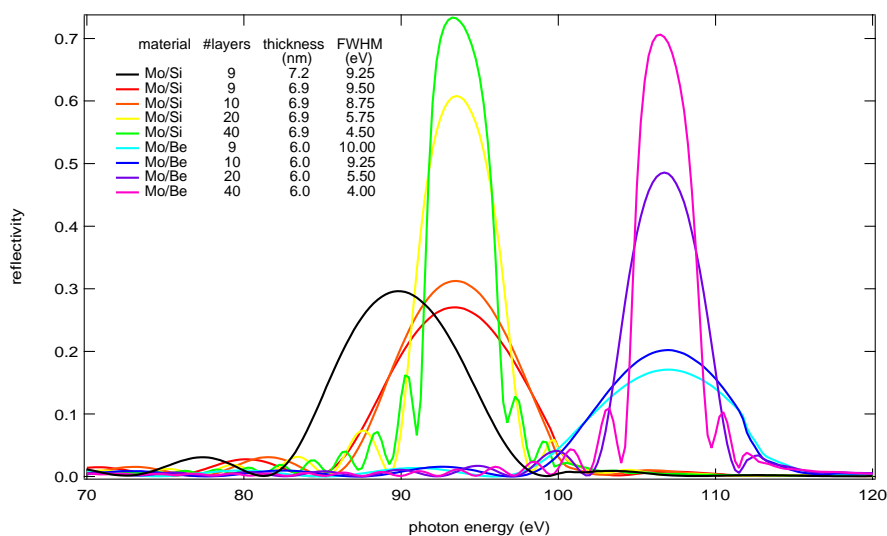


Figure 3.5: Calculated [119] reflectivity for different multilayer mirrors at a 10 degree angle of incidence. The highest reflectivity of Mo/Si multilayer mirrors and Mo/Be multilayer mirrors is about 70 %. To increase the reflectivity bandwidth of such mirrors, the amount of layers is decreased which decreases the overall reflectivity as well. The double-layer thickness can be used to tune the peak of the reflectivity.

bandwidth of such multilayer mirror decreases with reflectivity. For a multilayer mirror with a FWHM bandwidth of 9 eV, the reflectivity drops to less than 30 %.

The curves in figure 3.5 have been calculated [119] for constant layer thicknesses, but it is possible to make chirped soft-x-ray multilayer mirrors as well by varying the layer thickness. This allows for compensating a limited amount of chirp of the single attosecond pulses, in order to minimise the attosecond pulse duration. In figure 3.6 the role the mirror plays in the generation of single attosecond soft-x-ray pulses is made clear. The limited reflectivity bandwidth of the mirror can be chosen such that only the highest photon energies, which are released in one single burst, are reflected.

### 3.3 Attosecond time resolved ionisation spectroscopy

The availability of phase-controlled intense few-cycle pulses [54] made a new class of experiments possible, namely time-resolved measurements with an attosecond time resolution [68, 69]. A cartoon representing this class of experiments and the possible ways of observation is shown in figure 3.7. The first demonstration [68, 69] of an attosecond pump-probe measurement with an isolated pulse is depicted in part (a): A valence electron is released by the soft-x-ray pulse and a variation in the final kinetic energy of the electron as a function of delay between soft-x-ray pulse and infrared pulse is observed. The same is possible with the electrons excited from inner shells (part (b) and (d)) or even with secondary electrons from an Auger decay (part (c)).

When an electron is not released, but left in an excited state (either through an Auger decay or through shake-up), the infrared pulse can further ionise the ion with different probability as a function of delay, and a variation of the final charge state can be observed as a

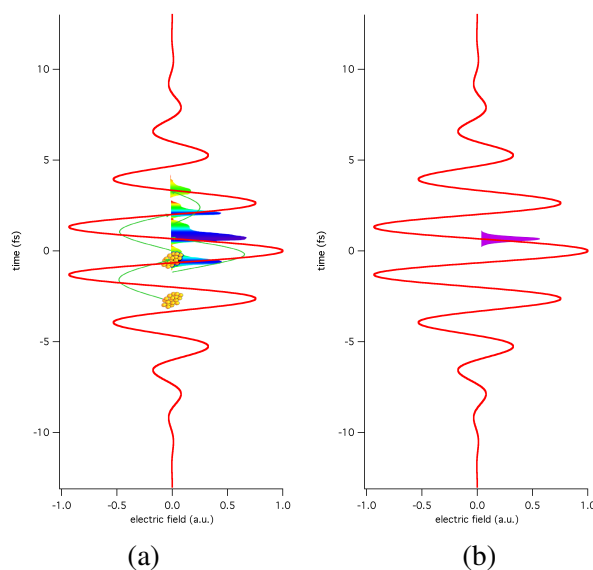


Figure 3.6: Graphic representation of the role played by the multilayer mirror in the generation of a single attosecond pulse

(a) Before the mirror there is a train of attosecond pulses, with varying spectra.

(b) After reflection off the multilayer mirror. Only the highest photon energies are reflected, if the reflectivity bandwidth is chosen correctly, thus resulting in a single attosecond soft-x-ray pulse.

function of time (part (d) and (e)). In this section, an experiment will be presented in which the dynamics of the Auger decay in Xenon induced by irradiation with 90 eV pulses is studied.

### 3.3.1 Auger decay

When a xenon atom absorbs a soft-x-ray photon, the probability that an electron from an orbit close to the atomic core is ejected is bigger than for an outer shell electron [120–123]. Since the emission of a photoelectron from a so called inner shell leaves the ion behind in a highly excited state, this excited state will decay, and in this process one (or more than one) more electrons can be emitted. This process is called Auger decay. Although the Auger decay is a very well understood process [124–128], the decay time of a number of decay channels could not be determined until now with frequency resolved measurements.

Time resolved XUV-pump-IR-probe measurements have already proven to be able to measure with relevant Auger-decay times with electron time-of-flight spectroscopy [129]. However, these time resolved measurements can only be applied to determine the decay time of a simple single Auger decay. In xenon however, a small portion of the atoms decays through a cascaded or double Auger decay [127]. The decay time of this channel can be determined with a XUV-pump-IR-probe measurement that employs ion time-of-flight spectroscopy. Depending on the decay time of the process under investigation, a single attosecond soft-x-ray pulse may be strictly required or not. In the following experiment, single attosecond pulses were not strictly required, powerful few-cycle pulses are required though.



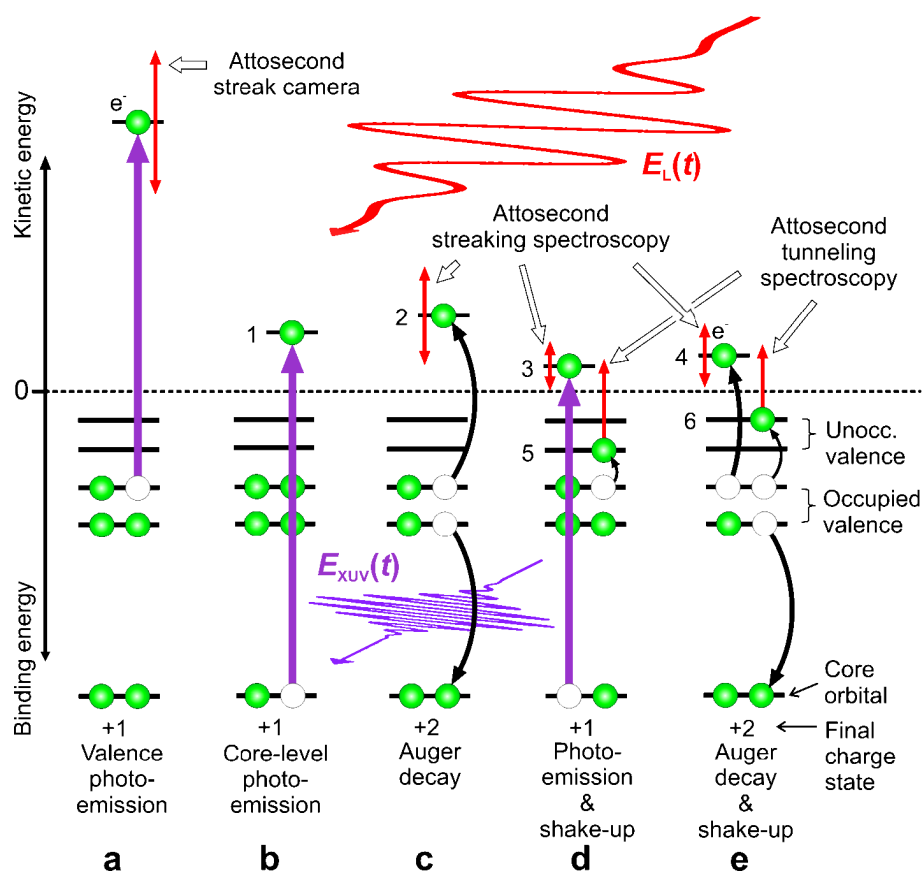


Figure 3.7: Different types of attosecond pump-probe experiments. An ultrashort sub-femtosecond soft-x-ray pulse triggers electron dynamics like valence (a) or core (b) photoelectron emission in the presence of a strong laser field. The temporal evolution of photoelectron emission can be probed by the attosecond streak camera technique to gain information about duration and chirp of the soft-x-ray pulse or to resolve the laser electric field in time. Core photo-electron emission can lead to secondary (Auger) electron emission (c). Auger electron emission provides information about the lifetimes of inner-shell vacancies inside the atom. By applying the streaking technique to these electrons, the Auger processes can be analysed in the time domain (attosecond streaking spectroscopy). Photoemission as well as Auger emission can be accompanied by shake-up of another electron to a previously unoccupied level (d and e). A reduced kinetic energy (labelled 3 and 4 in part d and e, respectively) will be measured for the photoelectron compared to the case without shake-up where the kinetic energy was higher (1 and 2). The difference in energy is used for the shake-up (curved black arrows to level 5 and 6). For sufficiently high laser intensities the shake-up electrons can be liberated by tunneling ionisation. The temporal evolution of the tunneling current will provide information about the duration of the process that populated the levels on a sub-femtosecond time scale (attosecond tunneling spectroscopy).

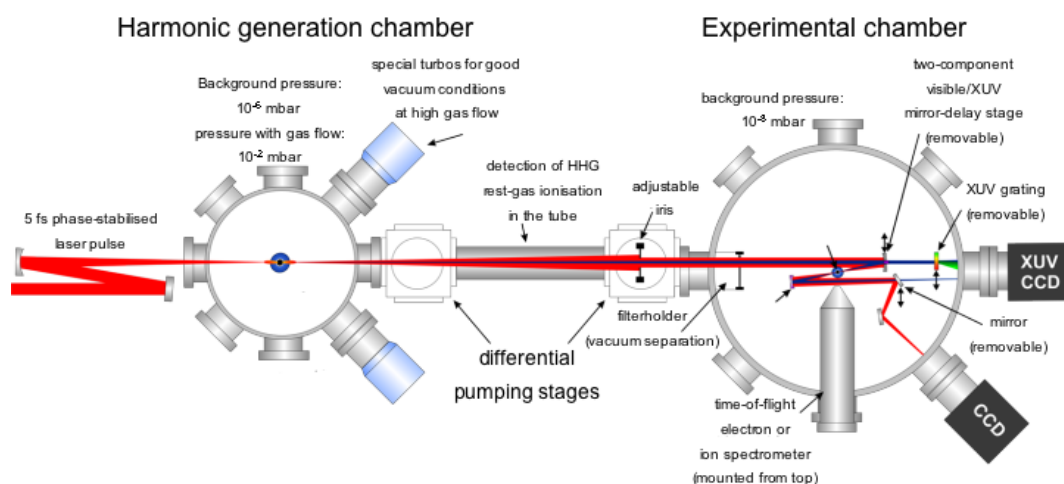


Figure 3.8: Schematic drawing of the vacuum system used for the attosecond time resolved ionisation spectroscopy experiments

### 3.3.2 Experimental setup

The laser system used for the experiment is shown in figure 1.5 on page 12. The 5-fs 350- $\mu$ J pulses are focused with a spherical mirror with a radius of curvature of -100 cm onto the harmonic gas target in a vacuum chamber, as shown in figure 3.2. A schematic of the vacuum system is shown in figure 3.8. After the harmonic generation chamber, the beam propagates through several differential pumping stages. One of the connecting vacuum tubes is modified such that any atoms of the rest gas that are ionised are detected, through which the stability of the system can be monitored. Before the entrance flange of the experimental chamber a motorised adjustable iris is centered on the beam, allowing to control the intensity in the experiment. Right after the entrance flange, an interchangeable set of filters is placed, such that the vacuum in the experimental chamber is separated from the rest of the system, forming the final differential pumping stage. In the experimental chamber a focusing double mirror is placed on a multi-axis motorised translation stage, for example allowing to move the mirror in and out of the beam. This gives the possibility to be able to look at the soft-x-ray beam directly or to look at the soft-x-ray spectrum when a transmission grating is moved into the beam.

One of the filters at the entrance of the experimental chamber (as shown in figure 3.9) is specially prepared for the experiments with the double mirror. It consists of a 5  $\mu$ m thin pellicle, with a hole in the middle. Over this hole, a 150 nm thin zirconium foil is installed. The zirconium foil transmits soft-x-ray radiation with photon energies above 70 eV, and blocks the fundamental laser beam. The pellicle is opaque for the soft-x-rays, and transparent for the fundamental laser beam.

The inner part of the double mirror (see figure 3.9) is a Mo/Si multilayer mirror, as discussed in section 3.2.1, and it can be moved with respect to the outer part. The outer part is a silver mirror. Both parts of the mirror are made out of the same substrate, and have a radius of curvature of -25 cm. The inner part can be translated with respect to the outer part of the mirror, allowing to time-delay the part reflected off the inner part of the mirror (the soft-x-ray pulse) and the part reflected off the outer part (the fundamental, 5-fs pulse).

After the focus, a re-collimating lens and a wedged uncoated plate are used to image the

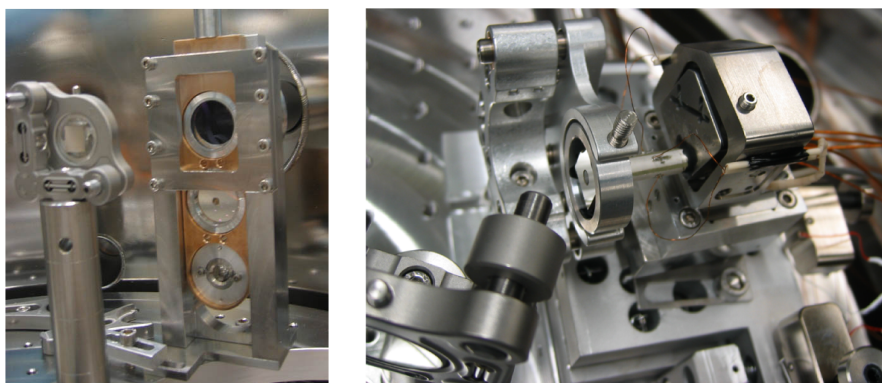


Figure 3.9: Photographs of the filter slider (left) and the double mirror (right). In the filter slider from the top to the bottom are put a plain  $5 \mu\text{m}$  thin pellicle, a specially prepared pellicle for spatially separating the soft-x-ray beam and the fundamental beam, and a stack of zirconium filters. The inner part of the double mirror is a Mo/Si multilayer mirror, the outer part a silver mirror.

focus on a CCD camera that is standing behind a window of the experimental chamber. The camera is used as well to align the inner and outer part of the double mirror with respect to each other. For this the special filter is replaced with a plain pellicle, such that the fundamental light is reflected as well from the multilayer. Since the focus is imaged on the CCD camera, it is possible to precisely overlap the focus of the inner and outer part of the double mirror. When the foci are aligned spatially, the temporal overlap of the beams reflected from the inner and outer part of the mirror can be determined. When the inner part of the mirror is translated longitudinally, in the range where the pulses reflected from both parts overlap in time, a changing fringe pattern can be observed. At the point where the contrast of the fringes is strongest, the time delay between both reflected parts is zero.

Ions created in the overlap of the two foci are detected by a reflectron-type time-of-flight ion spectrometer that combines a very high mass resolution ( $m/m = 1000$ ) with the capability to analyse particles within a small detection volume [130–132]. The measurements are performed in a vacuum system at a target pressure of approx.  $1 \times 10^{-2}$  mbar and a background pressure of  $2 \times 10^{-8}$  mbar.

### 3.3.3 Experimental results and discussion

When xenon atoms are ionised by soft-x-ray pulses with a photon energy around 90 eV, not only singly charged xenon ions are produced, but actually doubly or triply charged ions are even produced with much higher probability. The reason for this, is that electrons in the 4d shell can be resonantly ionised [123]. The creation of this 4d core hole leads with 99 percent probability to the production of higher charge states through the so called Auger decay, because of the short life time of the vacancy in the 4d orbital. 80 percent of the 4d vacancies lead to  $\text{Xe}^{2+}$  and 19 percent relaxes via a cascaded double Auger decay to  $\text{Xe}^{3+}$  [125]. This is schematically shown in figure 3.10.

The lifetimes of the  $4d_{3/2}$  ( $6.3 \pm 0.2$  fs) and  $4d_{5/2}$  ( $5.9 \pm 0.2$  fs) core holes were previously determined from the linewidth of the electron peaks in electron correlation spectroscopy [128]. There are two ways in which  $\text{Xe}^{3+}$  can be produced, the least probable is a direct dou-

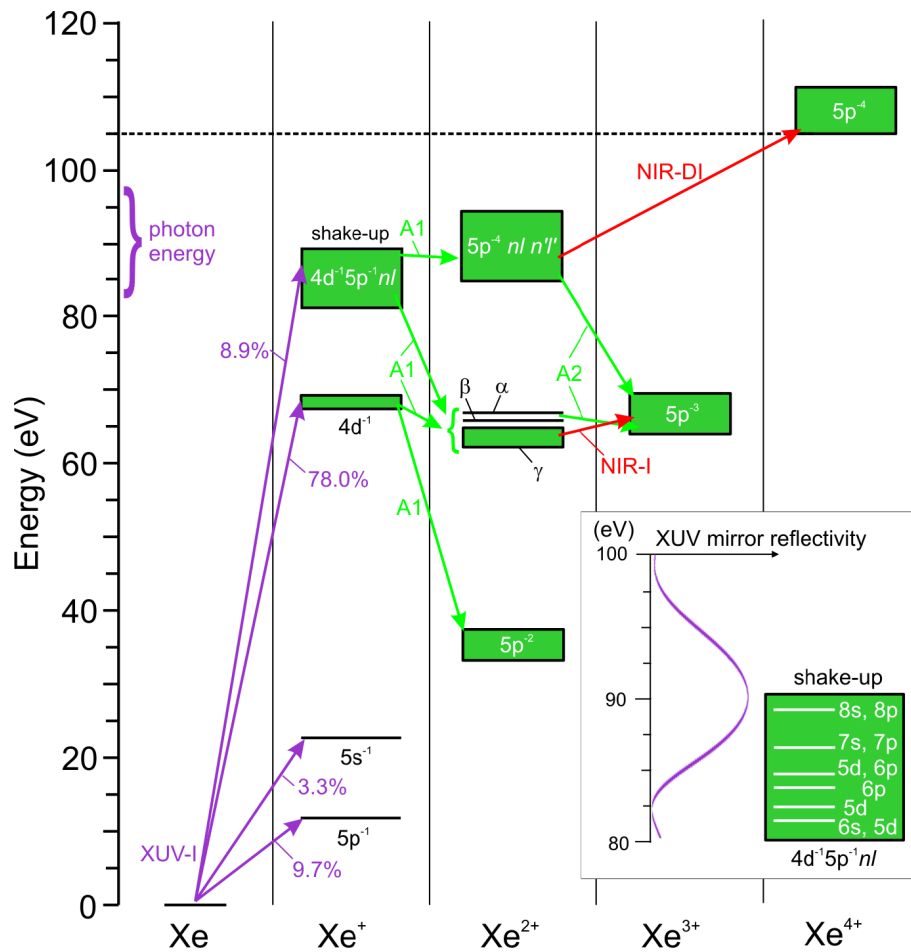


Figure 3.10: Relevant energy levels in xenon for different charge states. The relative amount of different configurations of singly charged xenon for soft-x-ray ionisation (XUV) is given for a photon-energy of 90 eV [121]. The soft-x-ray pulse preferably ionises from the  $4d^{-1}$  shell leaving an inner-shell vacancy. A subsequent Auger process (green arrows labelled A1) will follow with 99 % probability [125] and is mainly decaying to Xe<sup>2+</sup> in configuration  $5p^{-2}$ . Some final states ( $\alpha$  and  $\beta$  [126]) of A1 lie above the threshold-energy for Xe<sup>3+</sup> allowing a second Auger process (green arrow A2) leading to triply charged ions. A1 can also end up in a series of states  $\gamma$  being just below the threshold for triply charged xenon. The fundamental laser pulse (NIR) can ionise these states (red arrow NIR-I). Furthermore a series of  $4d^{-1}$  shake-up satellites is populated by the soft-x-ray pulse. The inset shows the possible configurations [124] together with the soft-x-ray multilayer mirror reflectivity corresponding to the soft-x-ray spectrum. The satellites mainly decay to lower lying states of Xe<sup>2+</sup> via A1, but also - with the emission of a near-zero energy electron - to  $5p^{-4}nl n'l'$  intermediate states. These states have such a high energy that there is a small probability for double ionisation by the fundamental pulse (red arrow NIR-DI) to Xe<sup>4+</sup> and only live for a short time until they decay via A2. Their population can be probed with the fundamental pulse.

ble Auger decay, the dominant process is a cascaded double Auger transition, through 2 intermediate states (presumably  $5s^{-1}5p^{-2}7p$  states [126, 127] labeled  $\alpha$  and  $\beta$  in figure 3.10). The first Auger process A1 also populates lower lying states (labeled  $\gamma$ , for example  $5s^{-1}5p^{-2}6p$  states, and some Rydberg states which are not shown), which are below the threshold for  $Xe^{3+}$ , such that the second process A2 is energetically not possible.

The decay time of the first Auger decay, A1, has been accurately determined, but for the decay time of the second process, A2, only a lower limit of 23 fs is reported from energy resolved measurements [128]. With the pump-probe setup described previously in this section, when carefully choosing the intensity of the infrared (fundamental) probe pulse, it is possible to trace the temporal evolution of the intermediate states transiently populated by the soft-x-ray pulses. To this end, xenon ion yields of the different charge states were measured as a function of the delay between the fundamental pulse and the soft-x-ray pulse, at the optimum intensity of the fundamental pulse.

The singly charge xenon ion yield showed no dependence on the delay between the soft-x-ray pulse and the fundamental pulse. This is to be expected, since the yield of singly ionised xenon at the laser intensity used in the experiment is much larger than the signal created by the soft-x-ray pulse. A change in the ion yield due to the soft-x-ray signal could not be resolved at the current signal to noise ratio. For doubly and triply charged xenon ions the situation is different. For positive delays a decrease in the doubly charged ion yield concurrent with an increase in the triply charged ion yield was observed, as is shown in figure 3.11a and b. The decrease in the  $Xe^{2+}$  yield and the increase in the  $Xe^{3+}$  yield can be explained with the help of figure 3.10. Doubly charged xenon ions are produced in the absence of the fundamental field either in the  $5p^{-2}$  state, or in one of the states labeled  $\gamma$ . In the latter case, the fundamental laser pulse can ionise the doubly charged xenon ions, leading to a decrease in the  $Xe^{2+}$  yield and an increase in the  $Xe^{3+}$  yield.

In the absence of the fundamental pulse no quadruply charged xenon ions are produced by the soft-x-ray pulse, and in the reversed case neither. However, in the presence of both pulses, a sharp increase is observed near zero delay, followed by a slower decrease as can be seen in figure 3.11c. For large positive or negative delays, no  $Xe^{4+}$  is produced. With the current understanding of the Auger processes and the energy levels in xenon involved, this can be explained as follows (see as well figure 3.10). The increase of the  $Xe^{4+}$  signal corresponds to the time-dependent population of the intermediate doubly-excited resonances  $5p^{-4}nl'n'l'$  and/or singly excited  $5s^{-1}5p^{-2}nl$  (the latter not shown in figure 3.10) states of  $Xe^{2+}$ . Those levels are populated by the first Auger process A1 from the satellites  $4d^{-1}5p^{-1}nl$  of the main  $4d^{-1}$  line upon emission of near-zero energy photoelectrons [124, 126]. The decrease of the  $Xe^{4+}$  signal at delays  $\tau > 0$  corresponds to the depopulation of the levels populated by the first Auger process to lower lying states, mainly to  $5p^{-3}$  states. Only a small fraction of the energy stored in the ion by the photo-ionisation of the 4d electron is needed for the first Auger process, a lot of energy can remain stored in the ion. The fundamental laser pulse can provide additional energy to further ionise the intermediate excited states of  $Xe^{2+}$  by double ionisation to produce  $Xe^{4+}$  (NIR DI in figure 3.10, and possibly to ionise some excited states of  $Xe^{3+}$  as well. When the intermediate states further decay to the  $5p^{-3}$  states, the fundamental pulse can no longer further ionise at the intensity used in the experiment.

From these observations, the time dependent behaviour of the quadruply charged xenon ion signal can be addressed to the probing of the first Auger process in the rising of the signal, and of the second Auger process in the decrease of the signal. To find the correct values for the Auger decay times, the nonlinear sampling function of the fundamental pulse has to be taken into account. From an equivalent experiment in Neon at comparable energy [70], we

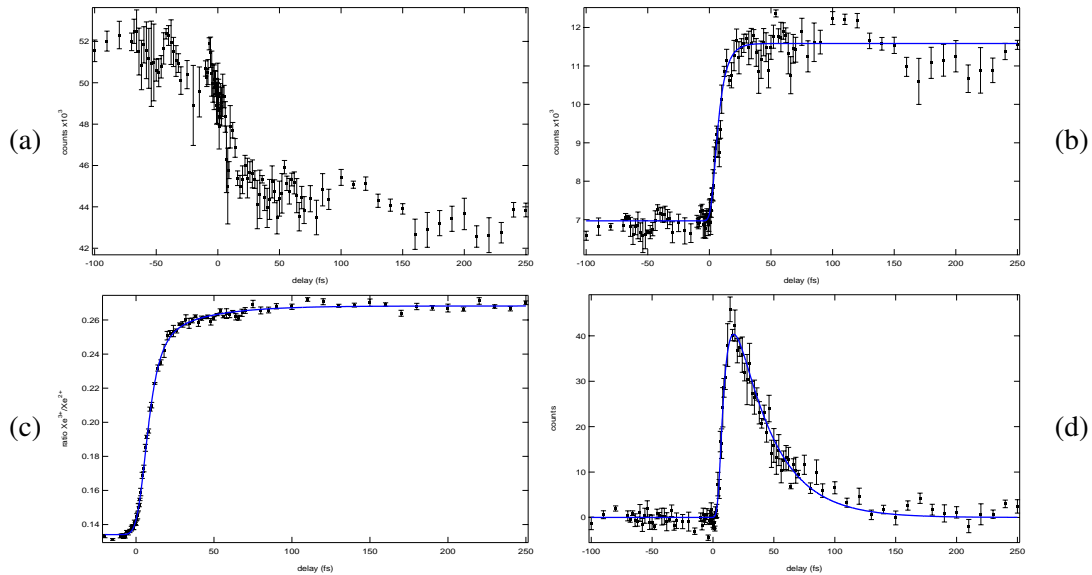


Figure 3.11: Counts of (a)  $\text{Xe}^{2+}$ , (b)  $\text{Xe}^{3+}$  and (d)  $\text{Xe}^{4+}$  ions versus delay time. The data-curves have been recorded 5 times with an integration time of 20 seconds for each data point. The average of the 5 measurements is plotted. The error-bar has been determined from the 5 runs. In (c) the ratio of  $\text{Xe}^{3+}/\text{Xe}^{2+}$  is shown, which shows much smaller error bars, since the dependence on the soft-x-ray intensity drops out. Assuming a Gaussian nonlinear probing function with a duration of  $4.3 \pm 0.4$  fs [70], the double exponential fit to the time evolution of  $\text{Xe}^{4+}$  yields the Auger decay times of  $6.0 \pm 0.7$  fs for A1 and  $30.8 \pm 1.4$  fs for A2. An exponential fit with the same Auger decay time A1 found in the fit to the  $\text{Xe}^{4+}$  data, for the data of  $\text{Xe}^{3+}$  yields the somewhat longer duration of the sampling function of  $5.8 \pm 2.5$  fs in agreement with the assumption that less energy is needed for the ionisation with the fundamental pulse here. The observation of a probing function longer than the measured pulse duration can be explained by a 10 fs background pulse with 10 percent of the intensity. The background arises from the fact that the pulse has not a Gaussian spectrum (see fig. 1.6 on page 13), and therefore has not a Gaussian temporal profile (which is clearly visible in fig. 1.7 on page 14). With the same probing function as in the fit to the  $\text{Xe}^{3+}$  data, the  $\text{Xe}^{3+}/\text{Xe}^{2+}$  data is fitted to a bi-exponential rise convoluted with the probing function, confirming the values for A1 and A2 as in the fit to the  $\text{Xe}^{4+}$  data.

assume the duration of the sampling function to be  $4.3 \pm 0.4$  fs (Correct numbers will be inserted here). The best result for the double exponential fit convoluted with the nonlinear sampling function yield an Auger decay time of  $6.0 \pm 0.7$  fs for process A1, and  $30.8 \pm 1.4$  fs for process A2, see figure 3.11. Both time constants are in good agreement with previous energy-resolved measurements [128]. The value found for A2 is the first exact measurement of this process, since previously only a lower limit could be given.

Since the value for A1 corresponding to the lifetime of the 4d core hole is now determined, this can be used to further analyse the time dependent behaviour of the  $Xe^{3+}$ . From figure 3.10 it can be seen clearly that all intermediate states, including those labeled  $\gamma$ , are populated by the first Auger process A1. The fundamental pulse will probe the population of the states labeled  $\gamma$  in the same way as the case described before. The only difference is, that the nonlinear probing function will be a different one, since the energy needed to create  $Xe^{3+}$  from the  $\gamma$  states is much less. An exponential increase, with the time constant for A1 determined from the  $Xe^{4+}$  signal, convoluted with a Gaussian probing function is fitted to the  $Xe^{3+}$  signal. The duration of the probing function is used as a fit-parameter. The best fit to the measured data is obtained for a duration of  $5.8 \pm 2.5$  fs for the probing function. As expected, this is longer than the duration of the probing function assumed in the fit to the  $Xe^{4+}$  signal. However, this duration is even longer than the pulse duration retrieved from second and third order autocorrelation traces at the time of the experiment. That the duration of the probing function is longer, is most probably due to the  $\sim 10$  fs pulse background with about 10 percent intensity compared to the 5 fs driver pulse. This background arises from the fact that the pulse spectrum is far from Gaussian, and therefore the temporal profile neither, which can be seen from figure 1.6 on page 13 and figure 1.7 on page 14. No decrease in of the enhanced  $Xe^{3+}$  yield is observed in the 250 fs time interval in this experiment, indicating a lifetime of the states labeled  $\gamma$  longer than a few picoseconds.

### 3.3.4 Conclusion

In an attosecond pump-probe setup combined with a reflectron-type ion time-of-flight spectrometer, the decay time of the second step in the cascaded Auger decay in xenon was measured to be  $30.8 \pm 1.4$  fs. The experimental data fit well with the well known delay time (6 fs) of the first step in this Auger decay. Previous energy resolved measurements could only give a lower limit of 23 fs for the second step of the Auger decay.

It is important to note that the accuracy of the measurement would decrease drastically with increasing pulse duration, especially when the pulse duration becomes longer than the measured decay time. This is mainly because a deconvolution needs to be made in order to extract the decay time from the data. Although the measured decay times did not put any constraint on the generation of the soft-x-ray pulse, a single attosecond pulse or a double attosecond pulse would produce the same curve, it is clear that intense few-cycle pulses (with a duration below 6 fs) are an absolute prerequisite for this experiment.





## Chapter 4

# Angular resolved ionisation with ultrashort pulses

Ionisation of matter with intense ultrashort pulses can give an insight to the structure of the matter under investigation, as well as an insight to the different mechanisms of ionisation itself. The experiments described in this chapter have all been carried out with the same setup [133], which will be discussed first. Then, angular resolved above threshold ionisation of rare gases with ultrashort pulses with a random phase, is discussed with the objective to provide the necessary background for the second experiment; carrier-envelope phase-resolved angular-resolved above-threshold-ionisation. Finally an experiment will be discussed in which the carrier-envelope phase of a few-cycle pulse controls the electron localisation in the dissociation of a small molecule.

## 4.1 Velocity-map imaging spectroscopy

### 4.1.1 The velocity-map imaging technique

Ion and electron imaging techniques have been developed to study atomic photoionisation [134, 135] and were adopted to study the dynamics of chemical reactions [136] soon thereafter. The early technique was improved by replacing the grid electrodes with electrostatic lenses [137]. This made velocity-map imaging possible, where all particles with the same initial velocity vector are mapped onto the same point on the detector. Three-dimensional velocity distributions of electrons or ions are projected onto a two-dimensional detector, normally consisting of a micro-channel plate and a phosphor screen. The image on the phosphor screen is recorded with a CCD camera.

In figure 4.1 the imaging and the reconstruction of the original distribution is graphically shown. Mathematically, this projection onto the detector plane of the initial 3-dimensional distribution, when it is cylindrical symmetric along an axis parallel to the detector plane, is called the Abel transform. Each slice  $f(x, y) = f(r)$  perpendicular to the symmetry ( $z$ ) axis is projected along the  $y$  axis, yielding a line  $f(x)$  in the 2-dimensional image  $f(x, z)$ .

$$f(x, z) = 2 \int_x^\infty \frac{r f(r, z)}{\sqrt{r^2 - x^2}} dr \quad (4.1)$$

The original slices  $f(r, z)$  of the distribution are obtained by an inverse Abel transform [136]:

$$f(r, z) = -\frac{1}{\pi} \frac{\partial}{\partial r} \int_r^\infty \frac{r f(x, z)}{x \sqrt{x^2 - r^2}} dx \quad (4.2)$$

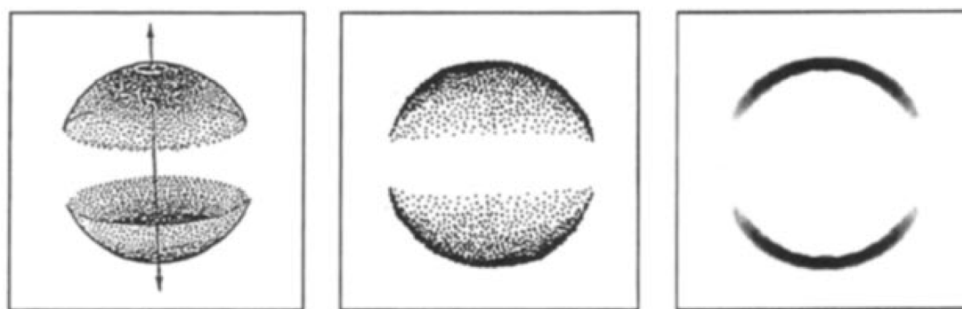


Figure 4.1: Projection of a 3-dimensional distribution (left) on a 2-dimensional plane (middle), and a slice through the reconstructed distribution (right). Image taken from Heck and Chandler [136].

Since the inversion can be done line by line, it allows reconstructing the full original 3-dimensional distribution. In practice, the inverse Abel transform is obtained by taking the inverse Hankel transform of the Fourier transform of each line of the 2-dimensional image. This method is very sensitive to the amount of noise in the 2-dimensional image, always accumulating the noise into a central noise line. In order to overcome this problem, an iterative inversion scheme was developed [138]. This method improves the quality of the reconstructed distribution since it does not accumulate the measurement noise in a central noise line.

#### 4.1.2 The velocity-map imaging spectrometer

In figure 4.2 a schematic drawing of the setup used for the experiments discussed in this chapter is shown. The pulses from the laser system as shown in figure 1.5 on page 12 are loosely focused with a spherical mirror (ROC = -80 cm) onto the atomic or molecular beam, in the center of the ion/electron optics. The intensity in the focus was controlled with a variable iris in the beam, intensities up to  $5 \times 10^{14} \text{W/cm}^2$  were realised. By tuning the pressure in the hollow fibre, the pulse duration could be tuned between 5 and 25 fs. In the studies on carrier-envelope phase effects, the wedges were used for scanning the carrier-envelope phase.

By tuning the high voltage applied to the repeller and extractor plates, it is possible to switch between ion and electron detection, and the resolution and maximum detected velocity can be tuned. The high voltage on the micro-channel plate detector (Hamamatsu, F2226-24PX) is switched on and off in a short period of time, improving the signal-to-background ratio, and in ion mode to allow selecting and measuring a certain ion species or charge state. The image on the phosphor screen was recorded with a CCD camera (Pulnix, TM-9701), and typically averaged over 1 minute of data acquisition. The atomic or molecular beam was pulsed with a 50 Hz piezo-actuated nozzle, minimising the gas load while allowing for higher gas densities in the interaction region. The gas density in the interaction region could be controlled via the backing pressure before the nozzle, and via the voltage applied to the piezo.

## 4.2 Above-threshold-ionisation with few-cycle pulses

As mentioned, with the velocity-map imaging spectrometer, it is possible to retrieve the full three-dimensional velocity distribution of electrons or ions created in the center of the ion/electron optics. For above-threshold-ionisation, no studies on the angular distribution of

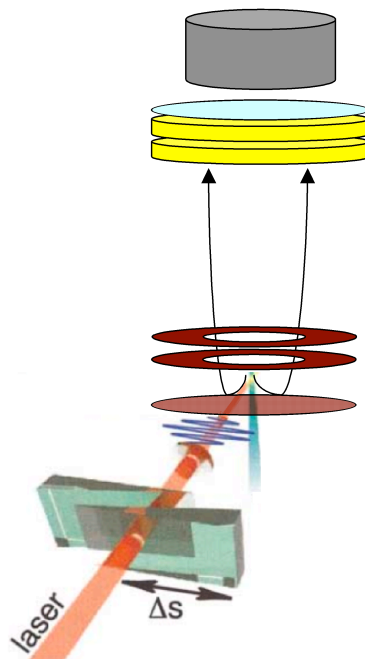


Figure 4.2: Schematic drawing of the setup used for the experiments in this chapter. The 5-fs laser beam is focused loosely onto the atomic or molecular beam in between the repeller and extractor plates. Electrons or ions with the same initial velocity are imaged on the same point on the detector. The image on the detector is recorded with a CCD camera. The wedges were used for scanning the carrier-envelope phase.

the emitted electrons with pulses shorter than 100 fs have been done. With 100 fs pulses the angular distributions of low energy electrons has been studied [139, 140]. The only study of the angular distribution of high energy ATI electrons was done with 50 ps pulses with an intensity of  $3 \times 10^{13} \text{W/cm}^2$  [141].

As already mentioned in Chapter 2.3, the process of above-threshold-ionisation (ATI) gets its name from the fact that (much) more photons are absorbed than necessary for ionisation, and the excess energy absorbed is converted in electron kinetic energy. So electrons with kinetic energies of many times the photon energy can be observed. With ultrashort pulses, the ATI process can be described as well with the simple three-step-model [89], the same model that is used to describe single attosecond pulse generation (see Chapter 3).

At a time close to the maximum optical field amplitude, the combination of the electric field of the pulse and the Coulomb potential of the atom create a barrier through which the least bound electrons can tunnel. With increasing intensity, and thus increasing field strength, this barrier gets smaller, and tunneling becomes more probable. After the electron tunneled through this barrier, it will be accelerated in the electric field of the laser, and after the field changes its sign, it can be accelerated back to its parent ion and recollision can take place. When this recollision happens as elastic scattering, the electron can be further accelerated in the electric field, and gain more energy. This process is responsible for the high-energy ATI electrons. When the recollision happens as recombination, high-harmonic radiation is emitted, and when the recollision happens as inelastic scattering, this can lead to the so called non-sequential double ionisation (NSDI) phenomenon.

The highest kinetic energies electrons will get in this process depend on the electric field strength, and is generally expressed in terms of the ponderomotive or quiver energy  $U_p$ , which is directly linked to the pulse intensity:  $U_p = e^2 E^2 / 4m\omega_0^2$ , with  $e$  and  $m$  the electron charge and mass, respectively.  $E$  is the maximum field amplitude (in V/m) and  $\omega_0$  is the driving laser frequency. Electrons that are not scattered can gain a maximum kinetic energy of  $2U_p$  and the electrons that are elastically scattered can gain a maximum kinetic energy of  $10U_p$ .

The angular distribution of the ATI electrons from argon, krypton and xenon, when excited with 25 fs pulses and 5 fs pulses, at different intensities, have been measured with the velocity map imaging spectrometer. With pulse durations as short as this, interesting features can be identified that are signatures of recollisions of the electron with its parent ion. With 25 fs pulses, more and clearer interference features are visible than with the 5 fs pulses. This is due to the larger energy bandwidth of the 5 fs pulses, and in part to the fact that high energetic electrons are created at fewer occasions, broadening the interference features.

In figure 4.3, 4.4 and 4.5 the VMI ATI electron images recorded for respectively argon, krypton and xenon are shown. The structures seen in the raw images (upper panels) are clearly enhanced in the inverse Abel-transformed images (second panel from top). Saturation of the CCD camera leads to underestimation of the signal at lower electron energies, which can be clearly seen in the images at high intensities. This has no effect on the retrieved signals at higher electron energies, and clear features of the angular distribution of the ATI electrons in the plateau region are still easily resolved. In all gases, the angular distribution of the ATI plateau electrons is broader when 25 fs pulses are used to ionise than when 5 fs pulses are used. A plausible explanation for this is that since the envelope of the pulses varies more slowly, more electrons have the chance to scatter under bigger angles. Scattering under these bigger angles with the polarisation direction occurs with increasing probability at later recollision times.

In xenon, the angular features are much more pronounced than in the case of argon and

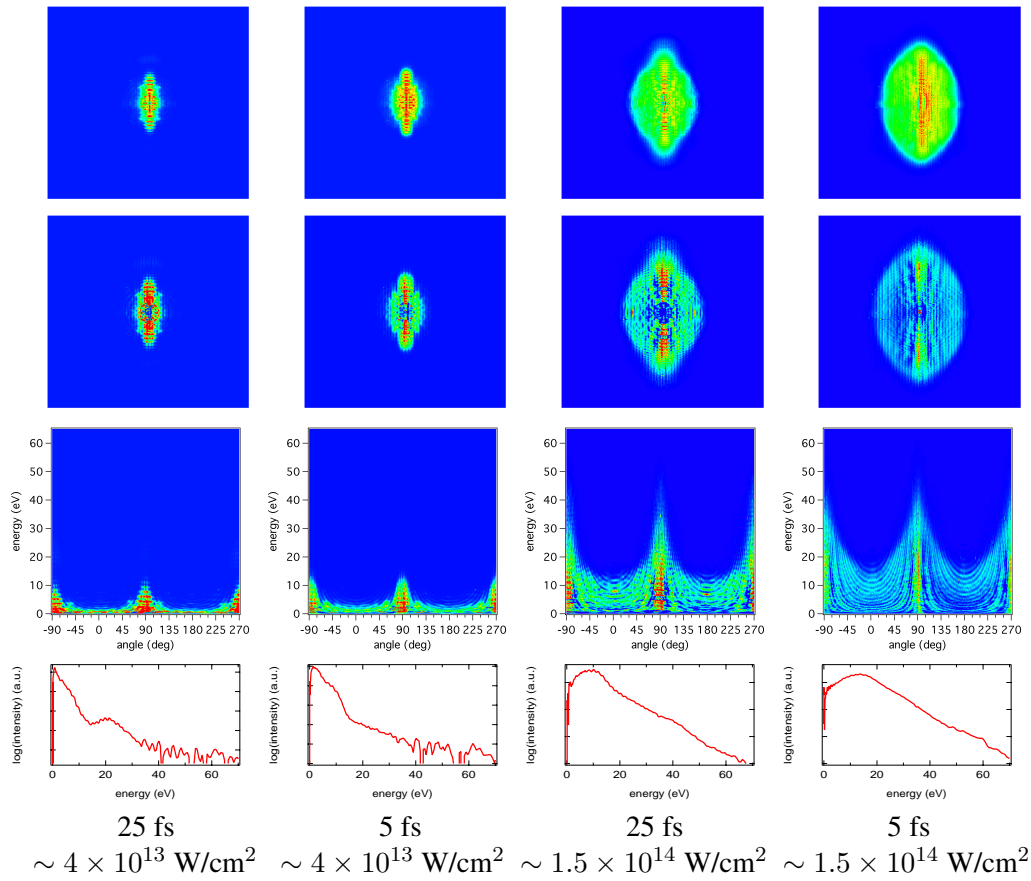


Figure 4.3: ATI electrons from argon at low intensity (left) and high intensity (right) with 25 fs pulses and 5 fs pulses. From top to bottom the raw image, the reconstructed slice through the 3-d distribution, the same plotted as a function of angle and electron energy and the photo-electron spectrum integrated over all angles.

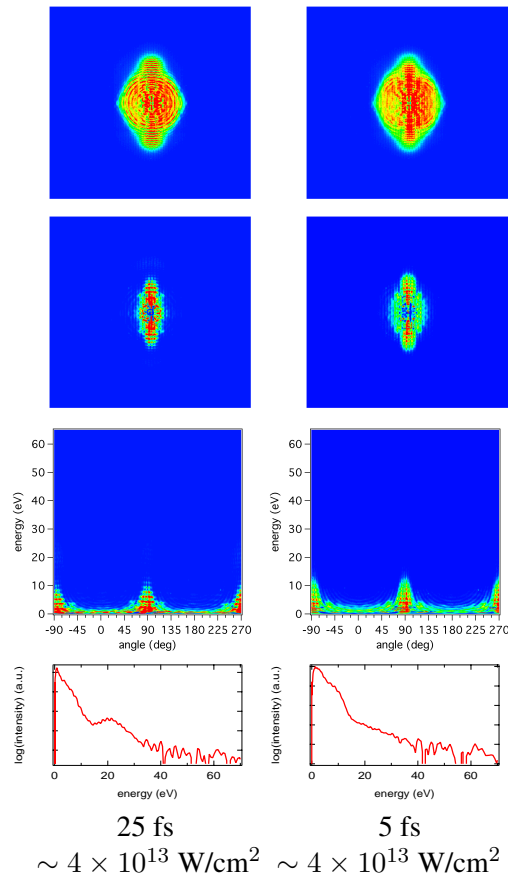


Figure 4.4: ATI electrons from krypton at low intensity with 25 fs pulses and 5 fs pulses. From top to bottom the raw image, the reconstructed slice through the 3-d distribution, the same plotted as a function of angle and electron energy and the photo-electron spectrum integrated over all angles.

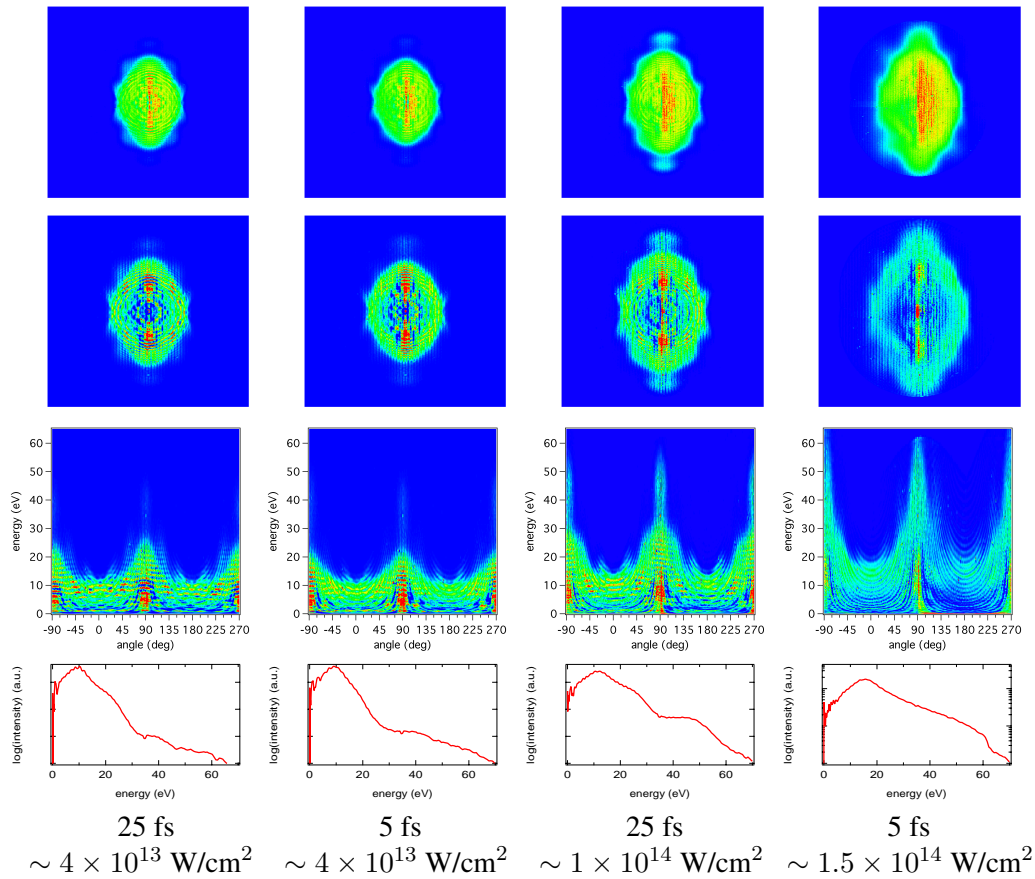


Figure 4.5: ATI electrons from xenon at low intensity (left) and high intensity (right) with 25 fs pulses and 5 fs pulses. From top to bottom the raw image, the reconstructed slice through the 3-d distribution, the same plotted as a function of angle and electron energy and the photoelectron spectrum integrated over all angles. Because of the very high intensity used for the rightmost set of figures, saturation of the detector caused a poorer quality of the images. It is as well clearly visible the measurement range of the detector was not enough to detect the highest electron kinetic energies in this case.

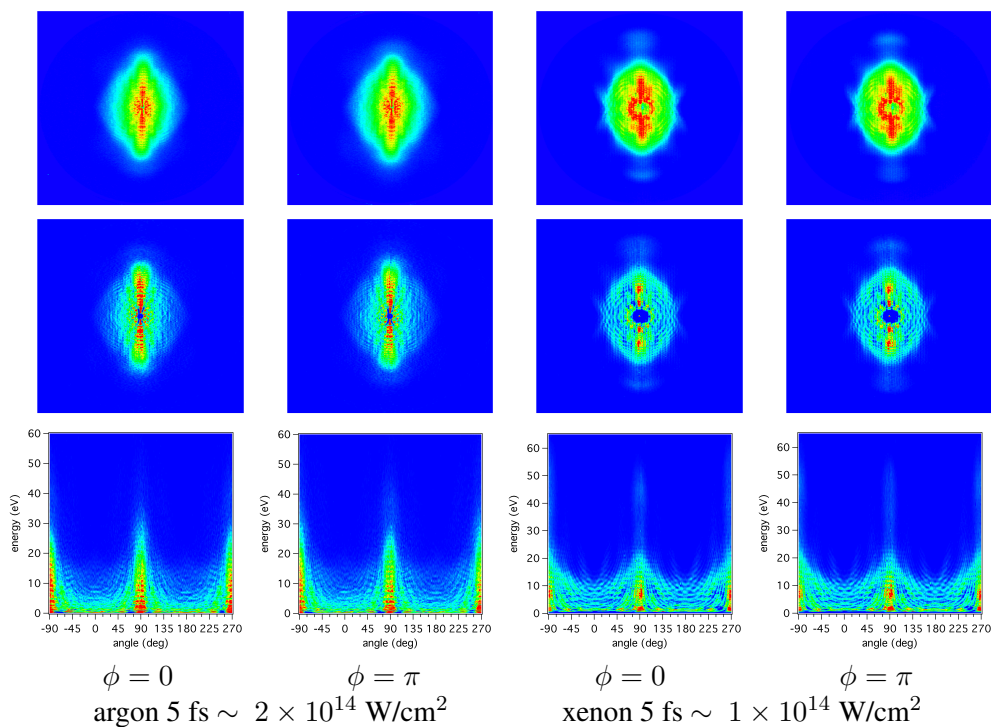


Figure 4.6: VMI ATI images in argon (left) and xenon (right), at two different phases,  $\phi = 0$  and  $\pi$ . From top to bottom the raw image, the reconstructed slice through the original 3-d distribution and the same plotted as a function of angle and electron energy. In argon interference patterns are visible at the highest electron energies either in the lower part or in the upper part of the images. As well more high energy electrons are seen in the lower or upper part of the image. In xenon the plateau gets a minimum in the lower or upper part of the images.

krypton. This is generally accounted for by the fact that the cross-section for recollision is substantially larger in the case of xenon than for argon and krypton. Another important point which should be pointed out, is that in the case of xenon, the intensity of the laser pulses was close to the value where the barrier created by the combination of the laser field and the Coulomb potential is totally suppressed, and thus xenon is far stronger ionised than argon or krypton.

### 4.3 Carrier-envelope phase-dependence of ATI

The spectral characteristics of ATI electrons from noble gases measured in a small angle range along the laser polarisation axis are well known to be dependent on the carrier-envelope phase when ionised by a few-cycle pulse [59, 87]. However, until now, no study has been carried out on the effect of the carrier-envelope phase on the angular distribution of ATI electrons. Since the carrier-envelope phase is regarded as the knob for steering the electron wave packets and thus the properties of the electrons after recollision, a strong effect of the angular distribution on the carrier-envelope phase is to be expected. The velocity map imaging spectrometer is an excellent tool to this end.

Again, measurements were done with argon, krypton and xenon, at different intensities.



The carrier-envelope phase was set to zero (modulo  $2\pi$ ) (phase zero for a cosine pulse) at the maximum of the asymmetry function at the highest electron energy, along the laser polarisation. In figure 4.6 typical images recorded at two different phases in argon and xenon are shown. While in argon an up-down asymmetry can be seen in the visibility of ‘fringes’, in xenon an extended plateau shows a clear minimum in either the lower or upper part of the image, but no interference-structure like in argon. In argon the number of high energy electrons shows a clear up-down asymmetry as well. From these images, it is not so easy to spot any differences at other than the highest electron energies along the laser polarisation direction. Further analysis, however, clearly reveals that at different electron energies and under different angles with the polarisation direction, a strong asymmetry depending on the carrier-envelope phase is present.

### 4.3.1 Asymmetry maps

There are different possibilities to systematically plot the asymmetry along different directions and over different energy ranges, as shown in figure 4.7 and 4.8 for a series of retrieved images of xenon ionised by 5 fs pulses at an intensity of  $1 \times 10^{14}$  W/cm<sup>2</sup>. Previous experiments [59] could only provide a figure like the lower right panel of figure 4.7, since the detection of electrons was restricted to a small angular range around the laser polarisation direction. The upper left and center panels in figure 4.8 however, reveal a clear phase dependent asymmetry at low energy, under very large emission angles.

In the phase-energy asymmetry maps under different angles this is much more difficult to see, because of measurement noise at higher energies and a blending effect due to strong interference in the energy domain. The interference in the energy-domain, which for few-cycle pulses is only visible for low-energy electrons arises due to the periodic emission of the electrons. This, again, is easily explained with the so called three-step-model. Since the electrons can only tunnel at times near the maximum of the electric field, electrons are emitted in a short period of time twice per optical cycle. Periodic emission in time is seen as interference in the frequency (thus also energy) domain.

With the velocity-map imaging technique, the accuracy at low energies is much more strongly dependent on the accuracy of the determination of the center of the image than for the higher energies. Therefore, at low energies, a small phase dependent asymmetry is likely to be blended by an asymmetry caused by the limited accuracy of the energy calibration in this range. When integrated over a larger energy range, this asymmetry-artefact is averaged out, and the phase-dependent asymmetry becomes visible.

In figure 4.9 and 4.10 phase-angle asymmetry maps in different electron energy ranges in argon at two different laser intensities are shown. At the low intensity of about  $3 \times 10^{13}$  W/cm<sup>2</sup>, asymmetries show up at low electron energies at large angles from the laser polarisation direction, while the asymmetry tends to restrict more along the laser polarisation at higher electron energies. The carrier-envelope phase dependent asymmetry at high kinetic energies, that are only emitted in a narrow angular range along the laser polarisation is well known and agrees well with theoretical predictions [87]. The elastic scattering of the electrons and the subsequent further acceleration in the laser field yields a strong phase-dependence of the electron kinetic energy spectra, and thus a strong asymmetry in the electron emission. Low-energy electrons that are emitted under bigger angles with the laser polarisation did clearly scatter off the parent ion. The momentum of the electron at the time it recollides strongly depends on the exact time it tunneled through the barrier, as well as the momentum it will gain or lose along the direction of the laser polarisation. With a few-cycle driver pulse, a strong

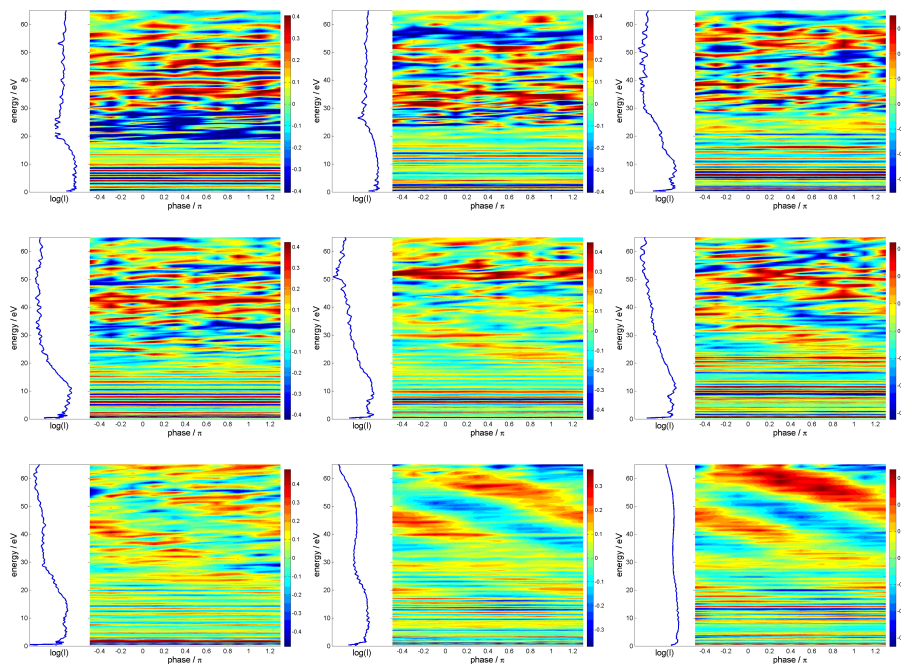


Figure 4.7: Phase-energy asymmetry maps in xenon. The intensity was about  $1 \times 10^{14}$  W/cm<sup>2</sup>. From left to right and top to bottom in 10 degree steps. The lower right panel resembles the experimental data from Paulus *et al.* [59], but with the direction in phase reversed.

dependence of the final kinetic energy of the electrons scattered under large angles on the carrier-envelope phase is thus to be expected, like for the high kinetic energy electrons.

At the high intensity of about  $2 \times 10^{14}$  W/cm<sup>2</sup>, though the signal to noise ratio is not as good as in the other case, the structures are clearly different. In this case as well, the asymmetry is clearly visible at low electron energies under large angles with the laser polarisation direction, while it tends to restrict more and more along the laser polarisation direction with increasing electron energy. In both cases, the best signal to noise together with a strong asymmetry is found in a relatively broad angle range around the laser polarisation direction, 10 to 30 eV below the cutoff electron energy. An answer to the question why the structure of the asymmetry seems much less complicated at the higher pulse energy can not be easily answered. For one thing, a slight difference in pulse duration can strongly change the asymmetry [90]. Another point is that the highest electron kinetic energies increases with intensity, and thus at a higher intensity the picture will clearly look different, since the asymmetry will be visible at higher energies as well.

In figure 4.11 phase-angle asymmetry maps in different electron energy ranges in krypton at a laser intensity of about  $1.7 \times 10^{14}$  W/cm<sup>2</sup> are shown. Although a hint of asymmetry is visible at lower electron energies at large angles from the laser polarisation direction, this is much less clear as in the case of argon. As in the case of argon, the asymmetry confines more and more around the laser polarisation direction for increasing electron energies. Here, like in the case of argon, the asymmetry is strongest and best resolved at electron energies about 10 to 30 eV below the cut-off energy. This can be simply explained by the fact that at lower electron energies, more electrons are detected, and thus the signal-to-noise ratio is expected to be better.

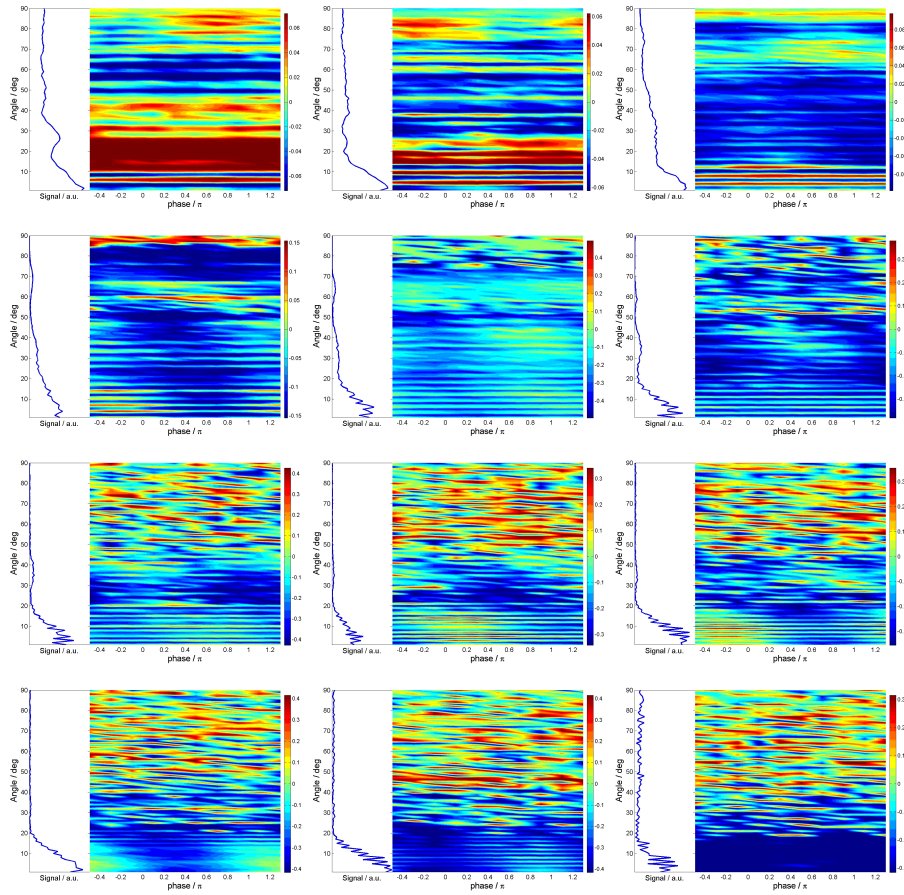


Figure 4.8: Phase-angle asymmetry maps in xenon. The intensity was about  $1 \times 10^{14}$  W/cm<sup>2</sup>. From left to right and top to bottom the energy is increasing in 5 eV steps, except for the first two images (upper left image 3-6 eV and upper centre image 6-10 eV).

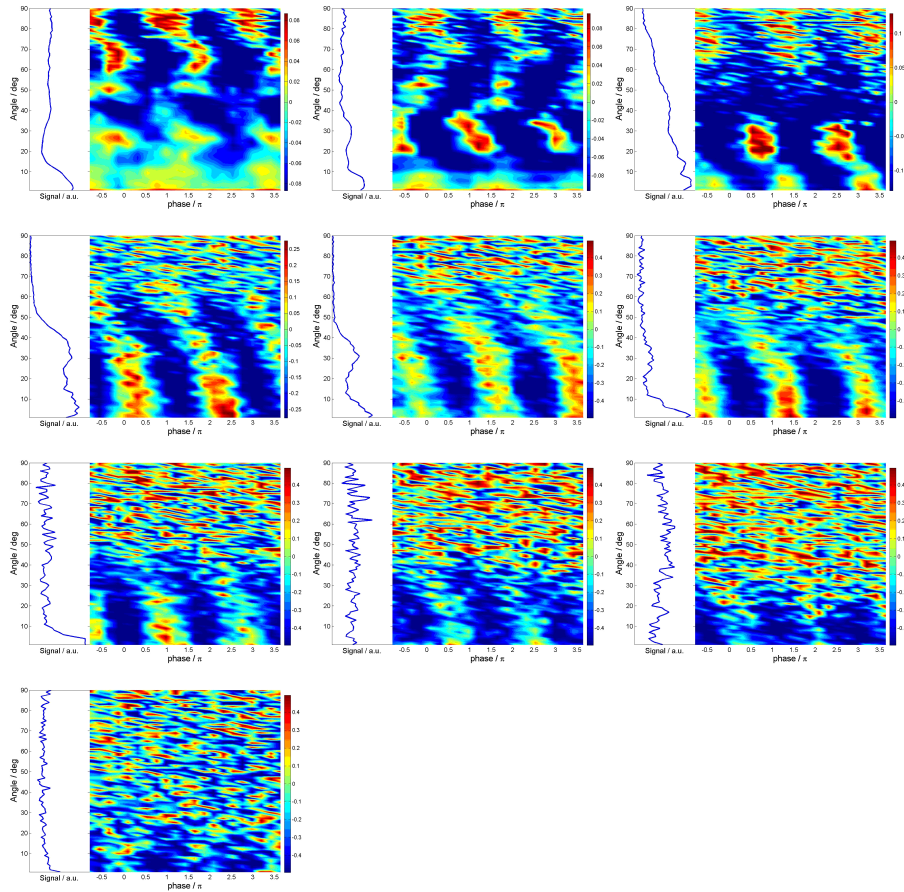


Figure 4.9: Phase-angle asymmetry maps in argon. The intensity was about  $3 \times 10^{13} \text{ W/cm}^2$ . From left to right and top to bottom the energy is increasing in 5 eV steps, except for the first two images (upper left image 3-6 eV and upper centre image 6-10 eV).

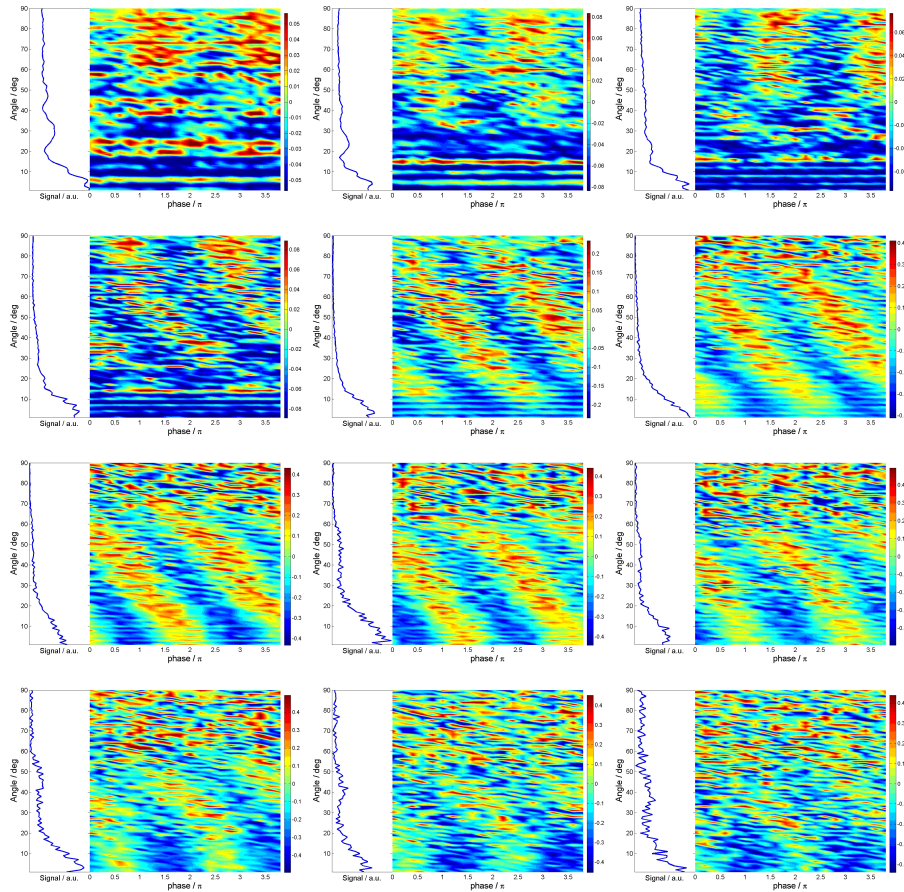


Figure 4.10: Phase-angle asymmetry maps in argon. The intensity was about  $2 \times 10^{14}$  W/cm<sup>2</sup>. From left to right and top to bottom the energy is increasing in 5 eV steps, except for the first two images (upper left image 3-6 eV and upper centre image 6-10 eV).



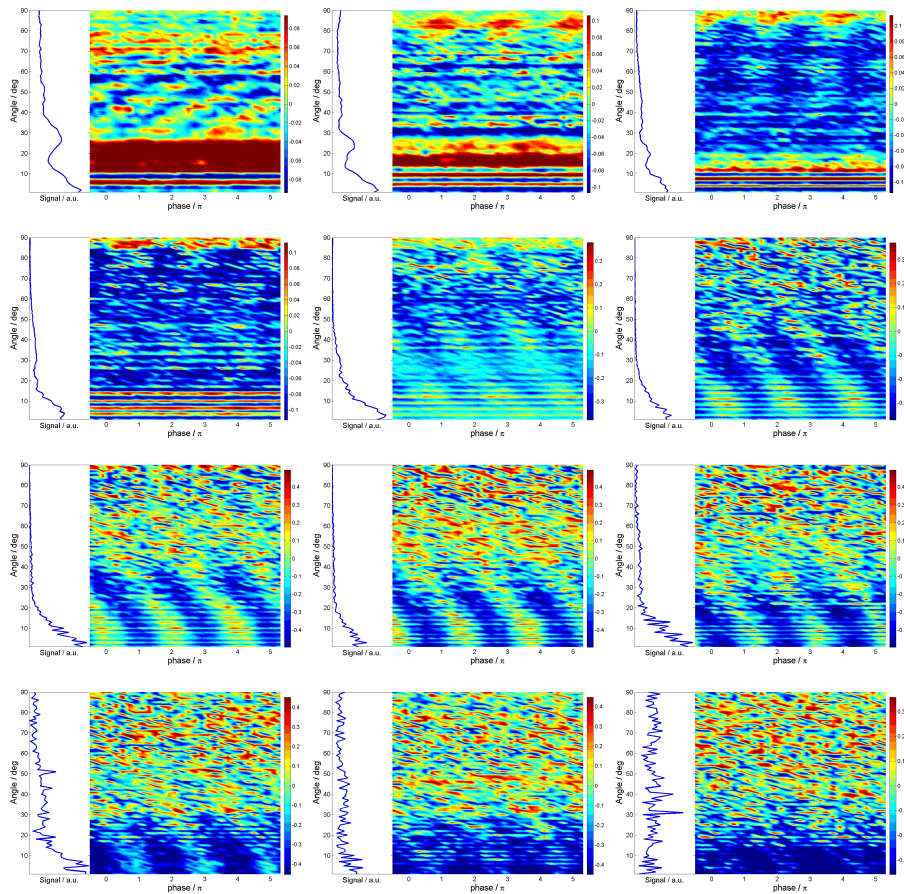


Figure 4.11: Phase-angle asymmetry maps in krypton. The intensity was about  $1.7 \times 10^{14} \text{ W/cm}^2$ . From left to right and top to bottom the energy is increasing in 5 eV steps, except for the first two images (upper left image 3-6 eV and upper centre image 6-10 eV).

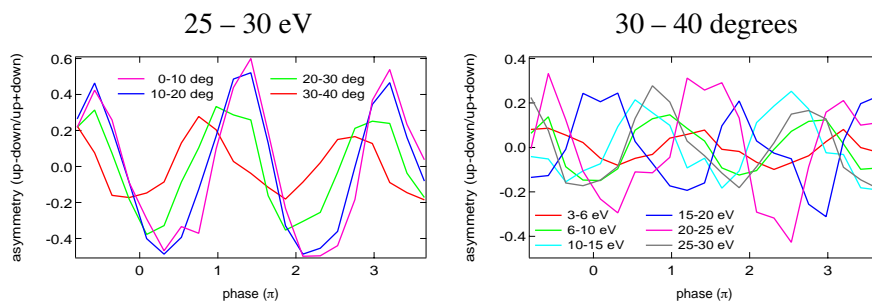


Figure 4.12: Cuts through the asymmetry maps in argon at  $3 \times 10^{13} \text{ W/cm}^2$ . A clear phase-shift of the asymmetry function in different areas is observed, which allows for a set of simple asymmetry measurements to determine the carrier-envelope phase of a pulse.

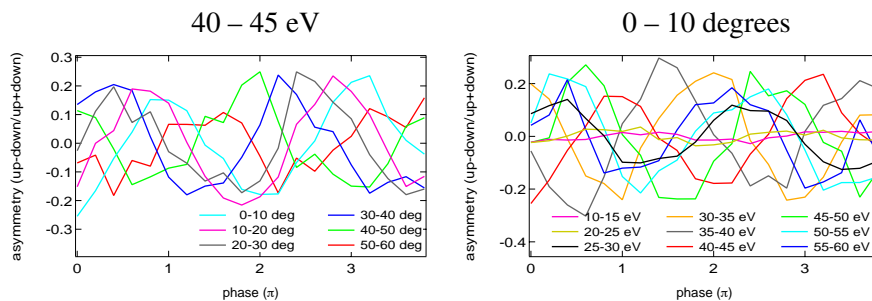


Figure 4.13: Cuts through the asymmetry maps in argon at  $2 \times 10^{14} \text{ W/cm}^2$ . A clear phase-shift of the asymmetry function in different areas is observed, which allows for a set of simple asymmetry measurements to determine the carrier-envelope phase of a pulse.

### 4.3.2 Simple asymmetry plots

Though with the asymmetry maps it is possible to retrieve the carrier-envelope phase of a pulse with a single measurement, it is still very interesting to know whether it is possible to do a more simple measurement in order to determine the carrier envelope phase of a pulse. To this end, several cuts through the asymmetry maps give an insight to achieve this. As already mentioned in chapter 2.3, more than one measurement, or for a single measurement, more than one phase dependent parameter is needed for an unambiguous measurement. If the asymmetry in two different (angle and/or energy) ranges is measured, it is important to choose these ranges appropriately, in order to maximise the accuracy.

In figure 4.12 and 4.13 several cuts through the asymmetry maps in figures 4.9 and 4.10 respectively, are shown. As can be seen clearly, there is a broad choice for a set of measurements that allow a reasonable accurate determination of the carrier-envelope phase. As an independent check for the fidelity of measurement, a measurement that should show little or no phase dependent asymmetry can be done in addition, as is indicated by a few traces in figure 4.13.

## 4.4 Control of electron localisation in molecular dissociation

The carrier-envelope phase of few-cycle pulses can be used to control the motion of bound electrons. In this section, this is demonstrated via dissociation of  $D_2$  into  $D^+ + D$ . The asymmetric ejection of the ionic fragment reveals that light-driven intra-molecular electronic motion prior to dissociation localises the electron on one of the two  $D^+$  ions in a controlled way.

Many of the processes in terms of which strong-field molecular interaction are presently interpreted (bond softening, enhanced ionisation, etc) were discovered in experimental and theoretical work on  $H_2$  and its isotopes HD and  $D_2$ , as reviewed by Posthumus [142]. The role of phase control in the dissociation of hydrogen has recently been addressed in a few theoretical studies [143–145]. In the experiment discussed in this section, a pronounced dependence of the direction of the  $D^+$  ejection on the waveform driving the reaction is observed. This directly implies a dependence of the electron localisation on the carrier-envelope phase of the laser pulse. Quantum-classical calculations were performed as well, confirming that light-field control of molecular electron dynamics is responsible for the observed phenomenon.

### 4.4.1 Experiment

Molecules normally ionise and dissociate in intense laser fields. The dissociation of  $D_2$  in such laser fields is known to happen through different pathways. The relative importance of those pathways strongly depends on the intensity and duration of the laser pulse [142]. The actual formation of fragment ions occurs via a two-step mechanism as depicted in figure 4.14. Initially the molecule is ionised by the laser field (red arrow in figure 4.14) and a vibrational wave packet is launched in the  $1s\sigma_g^+$  state. Break-up of the  $D_2^+$  ion is triggered by excitation to a repulsive state or after double ionisation.

In the single-ionisation pathways, excitation of bound  $D_2^+$  (for example to the  $2p\sigma_u^+$  state in figure 4.14) by recollision of the first electron (recollision excitation (RCE), green line) or directly by the laser field (sequential excitation (SE), blue line) leads to dissociation and the formation of a  $D^+$  ion and a D atom. This recollision excitation was exploited in recent molecular clock experiments studying the vibrational motion in  $D_2^+$  in a time-resolved manner. The consideration that molecular potentials are modified by the laser field allows for understanding of other mechanisms for dissociation. Bond-softening (BS) occurs when energy gaps open up at avoided crossings between adiabatic field-dressed potential energy curves.

In double-ionisation pathways, the formation of  $D_2^{2+}$  is followed by a second ionisation step via recollision (recollision ionisation (RCI)) or by the laser field (sequential ionisation (SI)). Enhanced ionisation (EI) takes place when the vibrational wave packet reaches a transition region where electron localisation occurs and where molecular orbitals turn into atomic orbitals. Double ionisation leads to the break-up of the molecule by Coulomb repulsion between the two  $D^+$  ions, and two momentum-matched ions are emitted symmetrically along the molecular axis, irrespective of the shape of the driving laser field. Control of the molecular electronic motion can also only possibly be observed in the BS, SE and RCE pathways, and therefore in the experiment double ionisation was kept at a minimum.

In figure 4.15 ion-kinetic-energy distributions for linear and circular polarised laser pulses with a duration between 5 and 8 fs are shown. The intensity was  $1.2 \pm 0.2 \times 10^{14}$  W/cm<sup>2</sup> in the linear polarised case, and  $2.4 \pm 0.2 \times 10^{14}$  W/cm<sup>2</sup> in the circular polarised case. Pre-



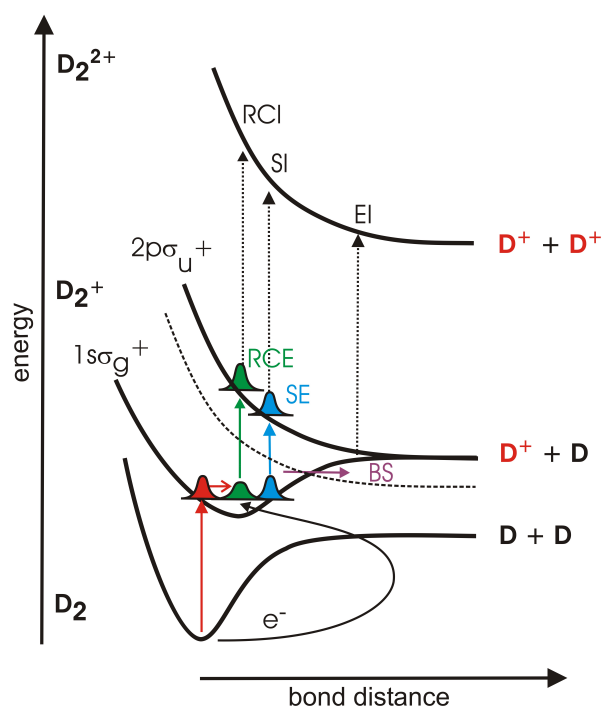


Figure 4.14: Pathways for the production of  $D^+$  ions from  $D_2$ , by dissociation of the molecular ion, (SE: Sequential excitation, RCE: Recollision), or by Coulomb explosion (RCI: Recollision, SI: Sequential ionisation, EI: Enhanced ionisation). Bond softening (BS) occurs when the avoided crossing between adiabatic potentials that are dressed by the laser field gives rise to dissociation from vibrational levels that were originally bound [146].

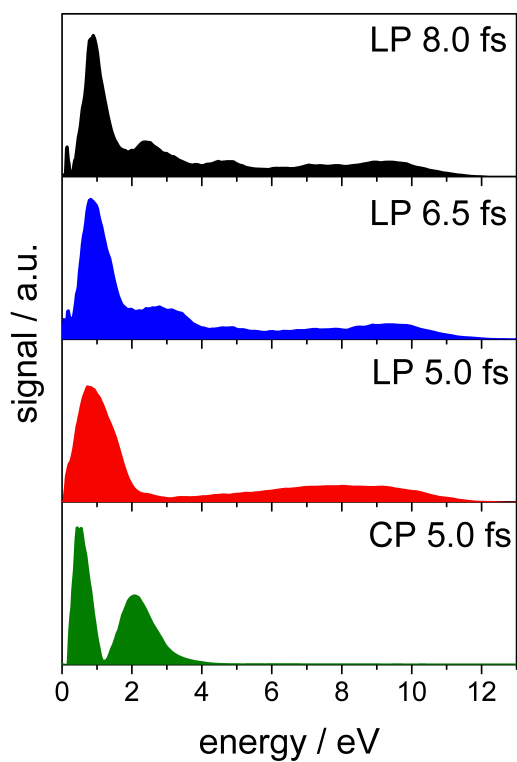


Figure 4.15: Kinetic energy spectra for dissociation of  $D_2$  by 5-8 fs linearly (LP) and 5 fs circularly (CP) polarised laser pulses without phase stabilisation, at  $I = 1.2 \pm 0.2 \times 10^{14} \text{ W/cm}^2$  and  $I = 2.4 \pm 0.2 \times 10^{14} \text{ W/cm}^2$ , respectively.

vious studies [147–149] suggest that  $D^+$  ions with low kinetic energies ( $< 3$  eV) originate from bond softening (at  $\sim 0.9$  eV) and enhanced ionisation (at  $\sim 2.5$  eV). Above 3 eV, the ionisation pathways involved are sequential excitation and/or ionisation and recollision excitation/ionisation. As can be seen in figure 4.15, the ion-kinetic-energy distribution for circular polarised pulses shows no components above 3 eV, indicating recollision is responsible for the creation of the high-energy fragments in the linear polarised case. Decreasing the pulse duration from 8 to 5 fs suppresses the spectral components that are assigned to double ionisation.

Figure 4.16 shows a cut through the reconstructed 3 dimensional momentum distribution in Cartesian coordinates  $(p_x, p_y)$  at  $p_z = 0$ , for 5-fs,  $1 \times 10^{14}$  W/cm<sup>2</sup> laser pulses. The image is averaged over 3500 laser pulses, with a randomly varying phase. The laser propagated along the x-axis, and the laser polarisation was along the y-axis. The angular distributions of the bond-softening channel (FWHM  $\sim 56^\circ$ ) and the weak enhanced ionisation channel (FWHM  $\sim 28^\circ$ ), in the center of the image, agree well with previous studies [150]. A nearly isotropic distribution is measured for higher energies (3–10 eV). This near isotropic distribution is a typical signature of recollision-induced fragmentation [148]. No difference in the emission of the ion fragments in the upward versus downward (along the laser polarisation axis) direction is observed in figure 4.16, since the image is averaged over 3500 laser pulses with randomly varying carrier envelope phase.

In figure 4.17 a phase-energy asymmetry map of the emitted ion-fragments is shown. The asymmetry is calculated with the ion signal integrated over an emission angle from  $-30$  to  $30$  degrees from the laser polarisation axis. This restriction of the angle range is chosen since the laser couples the two lowest lying electronic states only for molecules reasonably aligned along the laser polarisation. The highest degree of asymmetry, with a modulation depth of  $\sim 50\%$ , is observed between 3 and 8 eV. A very small phase dependence is seen in the bond softening and enhanced ionisation channels below 3 eV, as can be seen in the lower panel of figure 4.17. Since the asymmetric emission of  $D^+$  ions is only observed at kinetic energies that are virtually absent in the circular polarised case, electron-ion recollision has to be a vital element in the mechanism responsible for the observed carrier-envelope phase dependent asymmetry.

#### 4.4.2 Theoretical model

To gain qualitative insight into the mechanism responsible for the observed phase-controlled asymmetry in the dissociation of  $D_2^+$  the laser-driven motion of the two nuclei and the bound electron were modelled by numerically solving the time-dependent Schrödinger equation. As in previous studies [151], the process is modelled in terms of the  $1s\sigma_g^+$  and  $2p\sigma_u^+$  electronic states, and the molecule is assumed to be aligned along the laser polarisation axis.

In the model, the  $D_2^+$  molecular ion is formed in a single ionisation event that occurs at the maximum of the laser electric field. This ionisation produces a vibrational wave packet in the  $1s\sigma_g^+$  ground state that mimics the ( $v=0$ ) vibrational wave function of the  $D_2$  ground state. Population transfer from the  $1s\sigma_g^+$  ground electronic state to the  $2p\sigma_u^+$  excited electronic state is introduced at a delay of 1.7 fs after ionisation (corresponding to the first recollision time [152]). Later recollision events are efficiently suppressed with short laser pulses [148]. Due to the strongly repulsive nature of the  $2p\sigma_u^+$  state, the excited  $D_2^+$  molecular ion dissociates, and the momentum-matched D and  $D^+$  fragments acquire a large kinetic energy ( $E_k \leq 10$  eV). During the dissociation, the laser field transfers part of the  $2p\sigma_u^+$  population to the  $1s\sigma_g^+$  state, producing a dissociative wave packet with a large excess kinetic energy. The

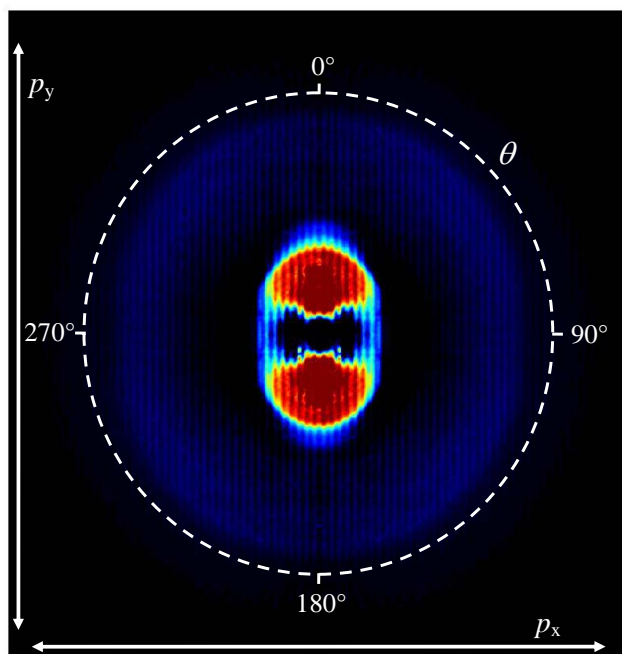


Figure 4.16: Two-dimensional momentum distribution image for  $D_2$  dissociation with  $1 \times 10^{14} \text{ W/cm}^2$  laser field, averaged over 3500 laser pulses with random phase.

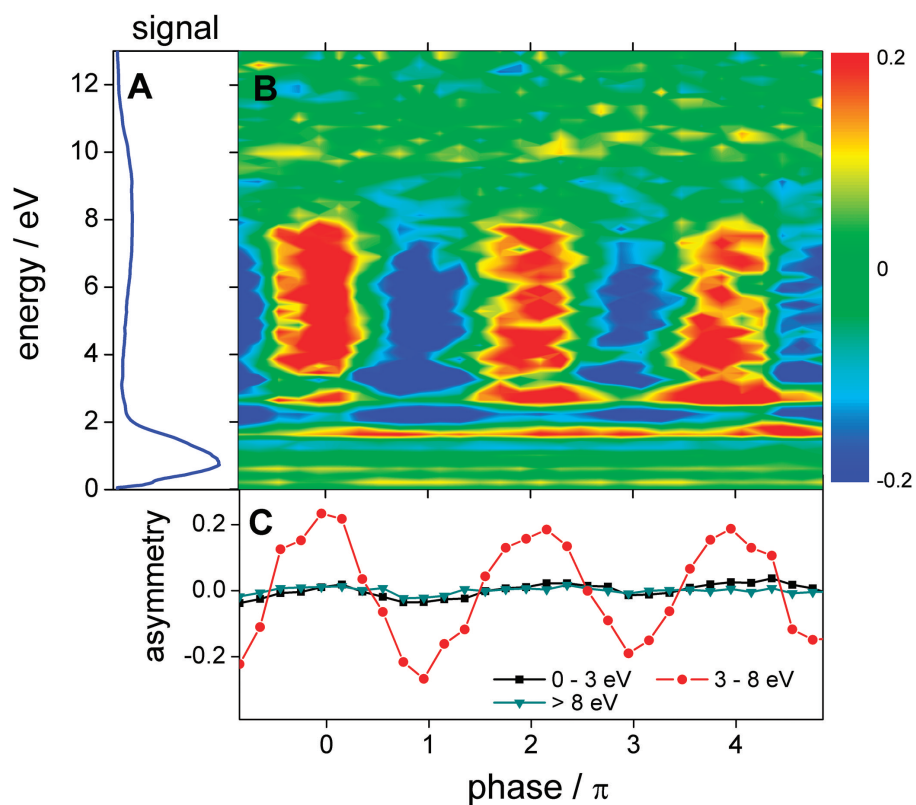


Figure 4.17: Phase-energy asymmetry map for the  $D_2$  ion fragment emission.  
 (a) Kinetic energy spectrum for  $D_2$  dissociation with 5 fs,  $1 \times 10^{14} \text{ W/cm}^2$  laser pulses without phase stabilisation.  
 (b) Phase-energy asymmetry map over a range of  $6\pi$  with a step size of  $0.1\pi$ .  
 (c) Integrated asymmetry over several energy ranges versus carrier envelope phase  $\phi$ .

emerging coherent superposition of the two electronic states results in a time-dependent localisation of the electron density on the upper or lower nucleus, due to the gerade and ungerade nature of the two states [143, 145, 153].

In figure 4.18 the temporal evolution of the laser field and the occupation of the  $1s\sigma_g^+$  and  $2p\sigma_u^+$  electronic states are depicted in panel a and b. A time-dependent electron localisation parameter quantifying the localisation on the upper/lower nucleus is displayed in panel c. By the time the molecule has dissociated (with the internuclear distance reaching  $\sim 15$  a.u.), the electron density is found to localise predominantly on the lower D atom. A simple shift of the carrier-envelope phase  $\phi$  by  $\pi$  reverses the field and turns the direction of emission of the ionic/atomic fragment opposite, in agreement with the experimental observation.

In more detail, the electron localisation dynamics can be considered as follows. Initially, the  $1s_g^+$  state is hardly populated by the laser induced coupling, and the energy gap  $\Delta W(t) = \hbar\omega(t)$  between the binding  $1s_g^+$  and repulsive  $2p_u^+$  states is much larger than the laser photon energy. Hence the electronic wave function can respond near-instantaneously to changes in the laser field, and the electron localisation parameter (see figure 4.18c) oscillates with the frequency of the light pulse. As the eigenfrequency  $\omega(t)$  of the two-level system decreases due to the increasing bond length, the laser field starts populating the lower level substantially, creating the prerequisite for electron localisation. In the calculations, the electron wave packet keeps evolving with the instantaneous eigenfrequency  $\omega(t)$  as the laser field strength approaches zero (for  $t > 7$  fs). The oscillation of the electron localisation ceases when the inter-atomic barrier that builds up between the two nuclei can no longer be overcome by the electron.

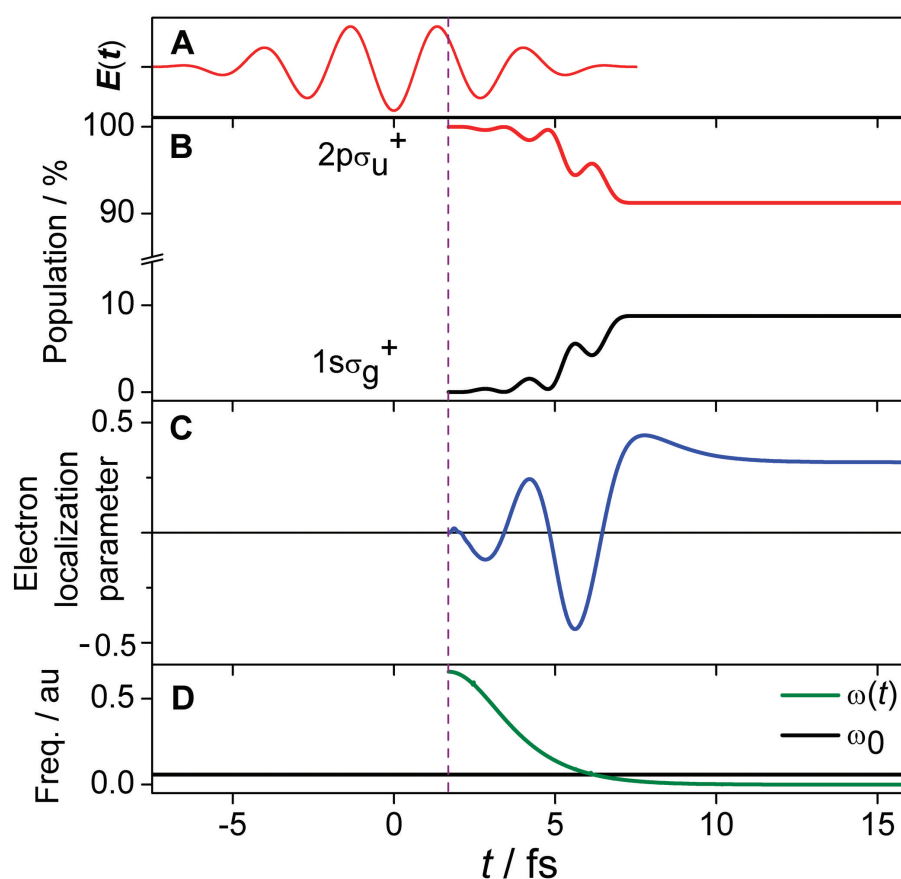


Figure 4.18: (a) Electric field of the 5 fs,  $1 \times 10^{14}$  W/cm<sup>2</sup> laser pulse used in the calculations, with carrier-envelope phase  $\phi = 0$

(b) Time-dependent populations of the  $1s\sigma_g^+$  and  $2p\sigma_u^+$  states of  $D_2^+$  after excitation through recollision.

(c) Temporal evolution of the electron localisation parameter starting from the time of recollision.

(d) Time-dependence of the eigenfrequency  $\omega(t)$  of the two-level system versus the laser frequency  $\omega_0$ . The dashed purple line marks the time of recollision in all panels.





## Conclusions and future prospects

Intense few-cycle pulses become more and more available in laser-laboratories. In this work, developments and methods to produce and characterise such pulses are presented. Because the temporal evolution of the pulse envelope is only slightly slower than the temporal evolution of the electric field, the relative phase between the electric field and the envelope, known as the carrier-envelope phase, becomes an increasingly important experimental parameter for decreasing pulse durations. Improved methods for absolute control over the carrier-envelope phase of intense few-cycle pulses are demonstrated in this work.

With the improved control over the carrier-envelope phase, more and more applications and experiments become possible. A few such experiments are presented in this work. The dynamics of ionisation processes induced by absorption of soft-x-ray radiation was time-resolved with a sub-femtosecond resolution [70]. In another experiment, the three-dimensional kinetic energy distribution of electrons as a result of above-threshold-ionisation of rare gas atoms was measured as a function of the carrier-envelope phase. The last experiment presented in this work showed the control of electron localisation in molecular dissociation with the carrier-envelope phase of the few-cycle driver pulse [66].

The improvement of the control of the carrier-envelope phase of intense few-cycle pulses was done in several ways. Not in the framework of this thesis, although still presented here, was the improvement of the carrier-envelope phase-stabilisation of femtosecond oscillators. This improvement made it possible to substantially extend the time over which a Ti:sapphire oscillator can be stabilised, as well as making the stabilisation fundamentally more reliable [49]. The second improvement, which was within the framework of this thesis, made it possible to take full advantage of the improved stabilisation of the oscillator in the case of stabilised amplified pulses. This improvement was made by decoupling the slow feedback loop needed to stabilise the carrier envelope phase at the output of the femtosecond amplifier from the oscillator stabilisation. A final improvement on the phase control of few-cycle pulses was made by combining the results presented by Schätzel *et al.* [71], O’Keeffe *et al.* [62] and Chelkowski *et al.* [90] into a simplified setup [72]. The physical process on which this control is based, above threshold ionisation, is extensively studied in the last chapter of this thesis.

The control of the carrier-envelope phase with a method based on above-threshold-ionisation still has an enormous potential for improvements. On the one hand, an even simpler and less expensive device as demonstrated in this work can be constructed, by replacing the multi-channel plates by simple current detectors. This change of the detectors allows for a dramatic reduction in the cost of the device. Apart from the cost reduction of the detection system, the vacuum system can be dramatically simplified, since restrictions on the vacuum conditions are much less strict. When the device is carefully designed, a measurement of the carrier-envelope phase in the same vacuum-chamber as the harmonic-generation-chamber is even possible, allowing for real-time, in-situ monitoring and control of the carrier-envelope phase (see figure 4.19).

On the other hand, the results presented in chapter 4.3 show the possibility for a more

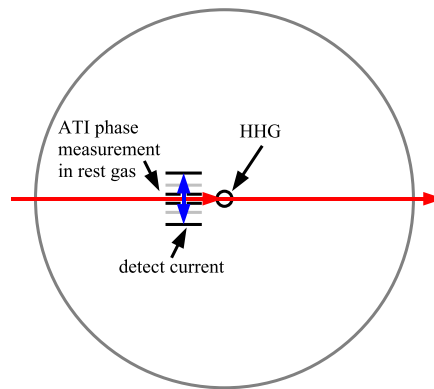


Figure 4.19: Schematic representation of the direct, in-situ measurement of the carrier envelope phase of the pulses driving the high-harmonic generation. Electrons flying through the grounded slits and with a kinetic energy large enough to overcome the blocking potential hit the detector plates and the current from both detector plates to ground is detected.

precise measurement of the carrier-envelope phase. Based on the results presented, a set of observables may be chosen that can be combined to yield a more precise phase measurement. This more precise phase measurement may for example be used to better characterise the carrier-envelope phase stability of the laser system.

## Appendix A

# How to stabilise the carrier envelope phase of a laser

### A.1 Oscillator

The carrier-envelope phase of the laser is stabilised in two steps. First the carrier-envelope phasedrift of the oscillator is stabilised. This is done such that the phasedrift between two subsequent pulses is exactly  $\pi/2$ , which implies that every 4th pulse is a replica. The oscillator is phase-stabilised using the f-to-zero technique, which is based on mixing the fundamental laser light with a signal generated by difference frequency mixing in a PPLN crystal. The DFG signal and the fundamental light overlap in a small spectral range between 1200 nm and 1500 nm. This is easily separated from the main fundamental beam, by using a 800 nm high reflector. The so called beat signal is observed on a photodiode, and monitored with an RF spectrum analyser. Since the repetition rate of the oscillator is 78.4 MHz, the beat-signal is to be stabilised at 19.6 MHz, a quarter of the repetition rate. In order to get the beat signal at the right frequency, move it there by moving the intra-cavity wedges, which are controlled with the dial on the ACU. If the dial is in neutral position the wedges are not moved, rotating it will set the speed of motion.

When the beat signal has been moved close enough to 19.6 MHz, it is possible to lock the oscillator phase drift. This is done by switching on the locking-electronics (switch on the counter, on the rack it says lockbox) and then set the black switch to Lock on. Now the signal on the oscilloscope below the RF-spectrum analyser is a flat line instead of a jittering sawtooth.

### A.2 Amplifier slow drift compensation

To ensure a stable carrier-envelope phase at the amplifier input, a pulse picker (the pockels-cell) is set to pick a pulse after every  $4n$  pulses of the oscillator pulse train. After the recompression however, a slow phase drift can be observed, so this drift needs to be compensated for. This is done by slightly moving a prism in the prism-compressor with a piezo translation stage. The phase drift is observed with a collinear f-to-2f interferometer. The feedback is controlled by the CEO Phase Lock program on the Dell computer on which the amplifier pump-laser is controlled as well.

#### A.2.1 The phase stabilisation program

The computer program that was used for phase-stabilising the laser in the experiments described in this thesis is written in LabVIEW. It reads the spectrum from the f-to-2f interfer-

ometer, and subsequently Fourier transforms a selected portion from the spectrum, where the fringes are most pronounced. The phase at the delay point of the fringes is used to compensate slow drift of the carrier envelope phase of the amplified pulses.

When the program is started, set the output channel name to *PiezoPrismsChannel* and the input channel name to *OscillatorLockMonitorandATIphase*. Then press the start button to see the fringe pattern. To lock the phase, locate the position of the fringes in the Fourier-domain (graph called Fourier transform amplitudes), and press the feedback on/off button.

The measured spectrum is displayed in the upper panel in the program. Right below the spectrum are the amplitudes (left) of the Fourier transform and its phases (right). In the amplitudes-graph, the delay position where the phase is taken is set. The lower two graphs show the phase-history and the feedback- and oscillator-stability-history. When the 'log phase' box is checked, the program writes the measured quantities and the feedback into a log-file.

### A.3 Carrier-envelope phase control with the mini stereo ATI

The mini stereo ATI can be used in three different ways. The first is to only monitor (and log) the carrier-envelope phase of the few-cycle pulses. The second is to further stabilise (or control) the carrier envelope phase of the input few-cycle pulses with the pair of wedges that is right after the hollow fibre output. The third way to use the mini stereo ATI is to use it as a replacement for the f-to-2f interferometer of the slow feedback loop. Therefore, there are two versions of the LabVIEW program of the mini stereo ATI on the computer. One can be used for monitoring and control of the phase with the wedges, the other for monitoring and control of the phase as a replacement of the f-to-2f interferometer in the slow loop.

How the carrier-envelope phase is measured with the mini stereo ATI apparatus is described in Chapter 2.3. From the signals measured at both MCPs, the carrier envelope phase is calculated with the following formula:

$$\phi - \phi_0 = A \arcsin \left( \frac{V_{\text{left}} - V_{\text{right}}}{V_{\text{left}} + V_{\text{right}}} \right) \quad (\text{A.1})$$

Here  $V_{\text{left}}$  and  $V_{\text{right}}$  are the signals of the left and right detector and  $\phi_0 \approx -0.3\pi$ . In the LabVIEW program, only the value  $\phi - \phi_0$  is calculated and displayed. Compared to equation (2.5) in Chapter 2.3, the factor  $A$  is moved out of the argument of the arcsin-function, to prevent the argument of growing out of the valid range. This implies that the phase displayed in the mini stereo ATI program is not exactly the  $\phi - \phi_0$ , but it is a quantity which is monotonically dependent on it.

**Mini stereo ATI – phase log** The program has a feature to write all measured data points to a text-file. In this file, time, the measured MCP signals and a photodiode signal are written, together with monitor-signals from the carrier-envelope phase locking electronics, and eventually the measured phase of the f-to-2f interferometer.

In addition to this, the program can provide via the DAC-card two output voltages which can be used to monitor and log the program output on another measurement computer. The first output provides a voltage proportional to the signal of the pulse energy monitoring photodiode, the second provides a signal proportional to the arcsin of the asymmetry function. This latter signal can thus be used to give an impression of the phase evolution, but it is not the exact value of the carrier-envelope phase. However, when logged on an external computer,

and afterwards compared with the log-file written on the mini stereo ATI computer itself, the exact value of the carrier envelope phase can be determined.

**Phase control with wedges** With the ‘wedges-version’ of the LabVIEW program, a feedback can be applied to the position controller of the wedges. The displacement of the wedges from the current position is in this mode proportional to the asymmetry function, stabilising the carrier-envelope phase in the mini stereo ATI to be  $\sim -0.3\pi$  or  $0.7\pi$ , depending on the polarity of the feedback (the proportionality factor positive or negative). In this mode, both the calculated phase and the pulse intensity can be monitored on an external computer as well.

**Replacement of the f-to-2f interferometer** With the ‘prism-version’ of the LabVIEW program, a feedback can be applied to the slow loop of the amplifier stabilisation directly. Again, the feedback is proportional to the asymmetry function, and so the polarity of the feedback determines the value to which the phase is stabilised.



## Appendix B

# Short manual of a Femtopower Compact Pro

### B.1 Switch on procedure

#### B.1.1 First warm-up phase

The oscillator chiller and pump-laser chiller should be on. The set temperatures are 17 degrees for the oscillator chiller (located directly under the laser table) and 18 degrees for the pump-laser chiller (located on the other side of the laser table close to the optics-cupboard). When this is checked, the pump lasers can be switched on. The Verdi pump-laser for the oscillator is switched on by turning the key to 'on', opening the shutter (press button shutter open) and setting the output to 5.5 W (press button power level 2). The Verdi controller is located on top of the shelf, you may need a chair or small ladder to reach it.

Then the amplifier (photonics) pump-laser is to be switched on. Check that the controller is on (located on top of the shelf, left of the Verdi controller), that is, the orange switch lights. The key must be in 'on' position. The laser output is controlled from the Dell-computer which is on the shelf right above the hollow fibre (right side of the laser). Here the program Laser Controller is found on the desktop, start this if it is not already running. When you start it, it asks for a username and password, both are *pii*. Check that the diode-current setting is set to a value just below 10 Ampere. Then press the button 'Diodes on', switch the shutter to open (click the switch). The program asks for a confirmation to open the shutter, answer yes. Then increase the current to 16 Ampere, by either rotating the dial, or entering the number right to the dial. Set the trigger mode to 'internal'. Check that the pump laser goes through the amplifier crystal correctly, then block it with one of the big black aluminium blocks. Now increase the diode current to 27.5 Amperes.

#### B.1.2 Second warm-up phase

After 10 to 15 minutes, the photonics pump laser is warmed up and the block in the beam needs to be removed. After removing this block, switch on the cooling of the crystal. The chiller is located below the photonics laser head under the table. It is switched on with the green button. After switching it on, immediately switch on the counter-heating of the crystal pot. For this switch on the power supply that is standing below the ACU box (on the laser table right below the Verdi power supply), the voltage should be about 19 V. The chiller will cool the crystal down to -90 degrees Celcius, the ACU will show a final temperature of about 185 K.

Again after about 15 minutes, the mode-locking of the oscillator needs to be started, which

is done by pressing the silver button at the back of the laser (behind the ACU-box). When the oscillator is mode-locked, the amplifier pump-laser trigger mode should be set to 'external' with the Laser Controller software. Now make sure the beam right before the hollow fibre is blocked, that is, that the black block is standing right before the fibre entrance window. After all this, set the pockels-cell voltage to 8 kV. The pockels-cell is the brownish box left of the laser, right above the entrance window of the hollow fibre. After this, the laser needs about 2 to 3 hours to warm up and stabilise completely.

## **B.2 Shut-down procedure**

To shut down the laser, proceed as follows: Place the black beam block right before the entrance window of the hollow fibre. Reduce the high-voltage of the pockels-cell completely. Close the shutter of the amplifier pump-laser with the Laser Controller software, reduce the diode current to right below 10 Ampere, switch of the diode current by pressing the 'Diodes on' button, and set the trigger mode to 'internal'. Switch of the amplifier chiller by pressing the red button. Switch off the Verdi, by pressing the power level 2 button, then the shutter open button and finally turning the key to stand-by. Switch off the counter heating of the crystal pot by turning off the power supply. That's all.



# Acknowledgements

At this point, I would like to thank all persons who helped to achieve the results presented in this thesis. First of all, I thank Prof. Ferenc Krausz, for giving me the chance to work in his group, and for providing the motivation and ideal conditions for this research.

Many thanks to the people with whom I worked together directly, for their support and nice collaboration, in chronological order: Gabriel Tempea, for introducing me to the everyday life in ultrafast science and teaching me the invaluable basics; Jozsef Seres, for providing the working laser system for the experiments on the high power pulse compression; Catherine Teisset, with whom I worked together on the sidetracks of pulse characterisation, assisting her on her diploma work; Eleftherios Goulielmakis, together with whom I was working in the then almost empty lab in the first days in Garching; Jens Rauschenberger, Matthias Uiberacker, Martin Schultze and Thorsten Uphues, the LWS-0.1-pro crew, making life in the lab just that little bit more exciting; Mark Vrakking, Matthias Kling, Yongfeng Ni and Jafar Khan, who brought the VMI to Garching, and with that a lot of exciting science; Matthias Lezius, who developed the mini stereo ATI apparatus, it was really nice working together on this presently most straightforward way of stabilizing the phase of few-cycle pulses.

I am indebted to Olga Smirnova, who made me understand a lot of the underlying physics of ATI and harmonic generation better, such that writing the text in this thesis became a bit less difficult. At this point, a second thank you to Eleftherios Goulielmakis and Matthias Kling is in order, for their efforts in giving helpful comments on earlier versions of this thesis. And I want to express my gratitude to Kevin O’Keeffe, for giving his suggestions on improving the English text of this thesis.

I would like to thank the people at Femtolasers for their help in getting started with the laser system, particularly Wolfgang Köhler and Mike Hentschel. As well I wish to thank Andreas Assion for showing so much interest in the work on the phase stabilisation that it even lead to a patent application.

I wish to thank all members of the group who were not mentioned before for the nice and friendly climate in the group, in Vienna and in Garching.

Many thanks to Eva Sturm, Elfriede Lohwasser, Dietlinde Egger, Monika Wild and Bettina Schütz for their support during the period of my work in Vienna and Garching, without their help life would have been never as easy as it was.

Last but not least many thanks to my wife Alma Fernández and my parents and sisters and friends, for being there for me night and day.



# Bibliography

- [1] A. Einstein, “Zur Quantentheorie der Strahlung”, *Physikalische Zeitschrift*, **18**, 121 (1917).
- [2] T. H. Maiman, “Stimulated Optical Radiation in Ruby”, *Nature*, **187**, 493 (1960).
- [3] T. Brabec and F. Krausz, “Intense few-cycle laser fields: Frontiers of nonlinear optics”, *Rev. Mod. Phys.*, **72**, 545 (2000).
- [4] D. Strickland and G. Mourou, “Compression of amplified chirped optical pulses”, *Opt. Commun.*, **56**, 219 (1985).
- [5] “Laser – Wikipedia, the free encyclopedia”, (), URL <http://en.wikipedia.org/wiki/Laser>.
- [6] P. Maine, D. Strickland, P. Bado, M. Pessot and G. Mourou, “Generation of ultrahigh peak power pulses by chirped pulse amplification”, *IEEE J. QE.*, **24**, 398 (1988).
- [7] C. Rolland and P. B. Corkum, “Compression of high-power optical pulses”, *J. Opt. Soc. Am. B*, **5**, 641 (1988).
- [8] S. Sartania, Z. Cheng, M. Lenzner, G. Tempea, C. Spielmann, F. Krausz and K. Ferencz, “Generation of 0.1-TW5-fs optical pulses at a 1-kHz repetition rate”, *Opt. Lett.*, **22**, 1562 (1997).
- [9] S. Backus, C. G. Durfee III, G. Mourou, H. C. Kapteyn and M. M. Murnane, “0.2-TW laser system at 1kHz”, *Opt. Lett.*, **22**, 1256 (1997).
- [10] Y. Nabekawa, Y. Kuramoto, T. Togashi, T. Sekikawa and S. Watanabe, “Generation of 0.66-TW pulses at 1 kHz by a Ti:sapphire laser”, *Opt. Lett.*, **23**, 1384 (1998).
- [11] Y. Nabekawa, T. Togashi, T. Sekikawa, S. Watanabe, S. Konno, T. Kojima, S. Fujikawa and K. Yasui, “All-solid-state 5-kHz 0.2-TW Ti:sapphire laser system”, *Opt. Express*, **5**, 318 (1999).
- [12] E. Zeek, R. Bartels, M. M. Murnane, H. C. Kapteyn, S. Backus and G. Vdovin, “Adaptive pulse compression for transform-limited 15-fs high-energy pulse generation”, *Opt. Lett.*, **25**, 587 (2000).
- [13] M. Hentschel, Z. Cheng, F. Krausz and C. Spielmann, “Generation of 0.1-TW optical pulses with a single-stage Ti:sapphire amplifier at a 1-kHz repetition rate”, *Appl. Phys. B*, **70**, 161 (2000).
- [14] V. Bagnoud and F. Salin, “Amplifying laser pulses to the terawatt level at a 1-kilohertz repetition rate”, *Appl. Phys. B*, **70**, 165 (2000).

- [15] S. Backus, R. Bartels, S. Thompson, R. Dollinger, H. C. Kapteyn and M. M. Murnane, "High-efficiency, single-stage 7-kHz high-average-power ultrafast laser system", *Opt. Lett.*, **26**, 465 (2001).
- [16] Y. Jiang, T. Lee, G. K. W. Li and C. G. Rose-Petruck, "High-average-power 2-kHz laser for generation of ultrashort x-ray pulses", *Opt. Lett.*, **27**, 963 (2002).
- [17] Z. Cheng, F. Krausz and C. Spielmann, "Compression of 2 mJ kilohertz laser pulses to 17.5 fs by pairing double-prism compressor: analysis and performance", *Opt. Commun.*, **201**, 145 (2002).
- [18] J. Seres, A. Müller, E. Seres, R. Herzog, K. O'Keeffe, M. Lenner, D. Kaplan, C. Spielmann and F. Krausz, "Sub-10-fs, terawatt-scale Ti:sapphire laser system", *Opt. Lett.*, **28**, 1832 (2003).
- [19] E. Seres, R. Herzog, J. Seres, D. Kaplan and C. Spielmann, "Generation of intense 8 fs laser pulses", *Opt. Express*, **11**, 240 (2003).
- [20] K. H. Hong, B. Hou, J. A. Nees, E. Power and G. A. Mourou, "Generation and measurement of  $> 10^8$  intensity contrast ratio in a relativistic kHz chirped-pulse amplified laser", *Appl. Phys. B*, **81**, 447 (2005).
- [21] A. J. Verhoef, J. Seres, K. Schmid, Y. Nomura, G. Tempea, L. Veisz and F. Krausz, "Compression of the pulses of a Ti:sapphire laser system to 5 femtoseconds at 0.2 terawatt level", *Appl. Phys. B*, **82**, 513 (2006).
- [22] A. Antonetti, F. Blasco, J. P. Chambaret, G. Cheriaux, G. Darpentigny, C. L. Blanc, P. Rousseau, S. Ranc, G. Rey and F. Salin, "A laser system producing  $5 \times 10^{19}$  W/cm<sup>2</sup> at 10 Hz", *Appl. Phys. B*, **65**, 197 (1997).
- [23] K. Yamakawa, M. Aoyama, S. Matsuoka, H. Takuma, C. P. J. Barty and D. Fittinghoff, "Generation of 16-fs, 10-TW pulses at a 10-Hz repetition rate with efficient Ti:sapphire amplifiers", *Opt. Lett.*, **23**, 525 (1998).
- [24] M. Pittman, S. Ferré, J. Rousseau, L. Notebeart, J. Chambaret and G. Chériaux, "Design and characterization of a near-diffraction-limited femtosecond 100-TW 10-Hz high-intensity laser system", *Appl. Phys. B*, **74**, 529 (2002).
- [25] A. Suda, M. Hatayama, K. Nagasaka and K. Midorkawa, "Generation of sub-10-fs, 5-mJ-optical pulses using a hollow fiber with a pressure gradient", *Appl. Phys. Lett.*, **86**, 111116 (2005).
- [26] R. T. Zinkstok, S. Witte, W. Hogervorst and K. S. E. Eikema, "High-power parametric amplification of 11.8-fs laser pulses with carrier-envelope phase control", *Opt. Lett.*, **30**, 78 (2005).
- [27] F. Tavella, K. Schmid, N. Ishii, A. Marcinkevicius, L. Veisz and F. Krausz, "High-dynamic range pulse-contrast measurements of a broadband optical parametric chirped-pulse amplifier", *Appl. Phys. B*, **81**, 753 (2005).
- [28] N. Ishii, L. Turi, V. S. Yakovlev, T. Fuji, F. Krausz, A. Baltuška, R. Butkus, G. Veitas, V. Smilgevičius, R. Danielius and A. Piskarskas, "Multimillijoule chirped parametric amplification of few-cycle pulses", *Opt. Lett.*, **30**, 567 (2005).

- [29] S. Witte, R. T. Zinkstok, W. Hogervorst and K. S. E. Eikema, "Generation of few-cycle terawatt light pulses using optical parametric pulse amplification", *Opt. Express*, **13**, 4903 (2005).
- [30] V. V. Lozhkarev, S. G. Garanin, R. R. Gerke, V. N. Ginzburg, E. V. Katin, A. V. Kirisanov, G. A. Luchinin, A. N. Mal'shakov, M. A. Mart'yanov, O. V. Palashov, A. K. Poteomkin, N. N. Rukavishnikov, A. M. Sergeev, S. A. Sukharev, G. I. Freidman, E. A. Khazanov, A. V. Charukhchev, A. A. Shaikin and I. V. Yakovlev, "100-TW Femtosecond Laser Based on Parametric Amplification", *JETP Lett.*, **82**, 178 (2005).
- [31] C. Y. Teisset, N. Ishii, T. Fuji, T. Metzger, S. Köhler, R. Holzwarth, A. Baltuška, A. M. Zheltikov and F. Krausz, "Soliton-based pump-seed synchronisation for few-cycle OPCPA", *Opt. Express*, **13**, 6550 (2005).
- [32] N. Ishii, C. Y. Teisset, T. Fuji, S. Köhler, K. Schmid, L. Veisz, A. Baltuška and F. Krausz, "Seeding of an Eleven Femtosecond Optical Parametric Chirped Pulse Amplifier and Its  $\text{Nd}^{3+}$  Picosecond Pump Laser From a Single Broadband Ti:Sapphire Oscillator", *IEEE J. QE.*, **12**, 173 (2006).
- [33] T. Fuji, N. Ishii, C. Y. Teisset, X. Gu, T. Metzger, A. Baltuška, N. Forget, D. Káplán, A. Galvanauskas and F. Krausz, "Parametric amplification of few-cycle carrier-envelope phase-stable pulses at  $2.1 \mu\text{m}$ ", *Opt. Lett.*, **31**, 1103 (2006).
- [34] A. Fernández, T. Fuji, A. Poppe, A. Fürbach, F. Krausz and A. Apolonski, "Chirped-pulse oscillators: a route to high-power femtosecond pulses without external amplification", *Opt. Lett.*, **29**, 1366 (2004).
- [35] S. Naumov, A. Fernández, R. Graf and P. D. an A. Apolonski, "Approaching the microjoule frontier with femtosecond laser oscillators.", *New. J. Phys.*, **7**, 216 (2005).
- [36] C. Gohle, T. Udem, M. Herrmann, J. Rauschenberger, R. Holzwarth, H. A. Schuessler, F. Krausz and T. W. Hänsch, "A frequency comb in the extreme ultraviolet", *Nature*, **436**, 234 (2005).
- [37] R. J. Jones, K. D. Moll, M. J. Thorpe and J. Ye, "Phase-coherent frequency combs in the EUV via high-harmonic generation inside a femtosecond enhancement cavity", *Phys. Rev. Lett.*, **94**, 193201 (2005).
- [38] A. Fernández, Chirped Pulse Oscillators: generation of microjoule femtosecond pulses at megahertz repetition rate, Ph.D. thesis, LMU München (2007).
- [39] M. Nisoli, S. D. Silvestri and O. Svelto, "Generation of high energy 10 fs pulses by a new pulse compression technique", *Appl. Phys. Lett.*, **68**, 2793 (1996).
- [40] G. Tempea and T. Brabec, "Theory of self-focusing in a hollow waveguide", *Opt. Lett.*, **23**, 762 (1998).
- [41] G. Tempea and T. Brabec, "Nonlinear source for the generation of high-energy few-cycle optical pulses", *Opt. Lett.*, **23**, 1286 (1998).
- [42] E. Mével, O. Tcherbakoff, F. Salin and E. Constant, "Extracavity compression technique for high-energy femtosecond pulses", *J. Opt. Soc. Am. B*, **20**, 105 (2003).

- [43] C. P. Hauri, W. Kornelis, F. W. Helbing, A. Heinrich, A. Couairon, A. Mysyrowicz, J. Biegert and U. Keller, "Generation of intense, carrier-envelope phase-locked few-cycle pulses through filamentation", *Appl. Phys. B.*, **79**, 673 (2004).
- [44] A. Couairon, M. Franco, A. Mysyrowicz, J. Biegert and U. Keller, "Pulse self-compression to the single-cycle limit by filamentation in a gas with a pressure gradient", *Opt. Lett.*, **30**, 2657 (2005).
- [45] D. J. Jones, S. A. Diddams, J. K. Ranka, A. Stentz, R. S. Windeler, J. L. Hall and S. T. Cundiff, "Carrier-Envelope Phase Control of Femtosecond Mode-Locked Lasers and Direct Optical Frequency Synthesis", *Science*, **288**, 635 (2000).
- [46] A. Apolonski, A. Poppe, G. Tempea, C. Spielmann, T. Udem, R. Holzwarth, T. W. Hänsch and F. Krausz, "Controlling the Phase Evolution of Few-Cycle Light Pulses", *Phys. Rev. Lett.*, **85**, 740 (2000).
- [47] R. Holzwarth, T. Udem, T. W. Hänsch, J. C. Knight, W. J. Wadsworth and P. S. J. Russell, "Optical Frequency Synthesizer for Precision Spectroscopy", *Phys. Rev. Lett.*, **85**, 2264 (2000).
- [48] S. Witte, R. T. Zinkstok, W. Hogervorst and K. S. E. Eikema, "Control and precise measurement of carrier-envelope phase dynamics", *Appl. Phys. B*, **78**, 5 (2004).
- [49] T. Fuji, J. Rauschenberger, A. Apolonski, V. S. Yakovlev, G. Tempea, T. Udem, C. Gohle, T. W. Hänsch, W. Lehnert, M. Scherer and F. Krausz, "Monolithic carrier-envelope phase-stabilization scheme", *Opt. Lett.*, **30**, 332 (2005).
- [50] T. Fuji, J. Rauschenberger, C. Gohle, A. Apolonski, T. Udem, V. S. Yakovlev, G. Tempea, T. W. Hänsch and F. Krausz, "Attosecond control of optical waveforms", *New J. Phys.*, **7**, 116 (2005).
- [51] A. Apolonski, P. Dombi, G. G. Paulus, M. Kakehata, R. Holzwarth, T. Udem, C. Lemell, K. Torizuka, J. Burgdörfer, T. W. Hänsch and F. Krausz, "Observation of Light-Phase-Sensitive Photoemission from a Metal", *Phys. Rev. Lett.*, **92**, 073902 (2004).
- [52] P. Dombi, A. Apolonski, C. Lemell, G. G. Paulus, M. Kakehata, R. Holzwarth, T. Udem, K. Torizuka, J. Burgdörfer, T. W. Hänsch and F. Krausz, "Direct measurement and analysis of the carrier-envelope phase in light pulses approaching the single-cycle regime", *New J. Phys.*, **6**, 39 (2004).
- [53] T. M. Fortier, P. A. Roos, D. J. Jones, S. T. Cundiff, R. D. R. Bhat and J. E. Sipe, "Carrier-Envelope Phase-Controlled Quantum Interference of Injected Photocurrents in Semiconductors", *Phys. Rev. Lett.*, **92**, 147403 (2004).
- [54] A. Baltuška, T. Udem, M. Uiberacker, M. Hentschel, E. Goulielmakis, C. Gohle, R. Holzwarth, V. S. Yakovlev, A. Scrinzi, T. W. Hänsch and F. Krausz, "Attosecond control of electronic processes by intense light fields", *Nature*, **421**, 611 (2003).
- [55] A. Baltuška, M. Uiberacker, E. Goulielmakis, R. Kienberger, V. S. Yakovlev, T. Udem, T. W. Hänsch and F. Krausz, "Phase-Controlled Amplification of Few-Cycle Laser Pulses", *IEEE J. QE.*, **9**, 972 (2003).

- [56] M. Kakehata, H. Takada, Y. Kobayashi, K. Torizuka, H. Takamiya, K. Nishijima, T. Homma, H. Takahashi, K. Okubo, S. Nakamura and Y. Koyamada, "Carrier-envelope-phase stabilized chirped-pulse amplification system scalable to higher pulse energies", *Opt. Express*, **12**, 2070 (2004).
- [57] E. Gagnon, I. Thomann, A. Paul, A. L. Lytle, S. Backus, M. M. Murnane, H. C. Kapteyn and A. S. Sandhu, "Long-term carrier-envelope phase stability from a grating-based, chirped pulse amplifier", *Opt. Lett.*, **31**, 1866 (2006).
- [58] G. G. Paulus, F. Grasbon, H. Walther, P. Villorresi, M. Nisoli, S. Stagira, E. Priori and S. D. Silvestri, "Absolute-phase phenomena in photoionization with few-cycle laser pulses", *Nature*, **414**, 182 (2001).
- [59] G. G. Paulus, F. Lindner, H. Walther, A. Baltuška, E. Goulielmakis, M. Lezius and F. Krausz, "Measurement of the Phase of Few-Cycle Laser Pulses", *Phys. Rev. Lett.*, **91**, 253004 (2003).
- [60] F. Lindner, G. G. Paulus, H. Walther, A. Baltuška, E. Goulielmakis, M. Lezius and F. Krausz, "Gouy Phase Shift for Few-Cycle Laser Pulses", *Phys. Rev. Lett.*, **92**, 113001 (2004).
- [61] X. Liu, H. Rottke, E. Eremina, W. Sandner, E. Goulielmakis, K. O'Keeffe, M. Lezius, F. Krausz, F. Lindner, M. G. Schätzel, G. G. Paulus and H. Walther, "Nonsequential Double Ionization at the Single-Optical-Cycle Limit", *Phys. Rev. Lett.*, **93**, 263001 (2004).
- [62] K. O'Keeffe, P. Jöchl, H. Drexel, V. Grill, F. Krausz and M. Lezius, "Carrier-envelope phase measurement using a non phase stable laser", *Appl. Phys. B*, **78**, 583 (2004).
- [63] K. O'Keeffe and M. Lezius, "Negligible carrier envelope phase dependence of total single and double ionization yields of xenon", *Eur. Phys. J. D.*, **37**, 305 (2006).
- [64] F. Lindner, M. G. Schätzel, H. Walther, A. Baltuška, E. Goulielmakis, F. Krausz, D. B. Milošević, D. Bauer, W. Becker and G. G. Paulus, "Attosecond Double-Slit Experiment", *Phys. Rev. Lett.*, **95**, 040401 (2005).
- [65] M. Kreß, T. Löffler, M. D. Thomson, R. Dörner, H. Gimpel, K. Zrost, T. Ergler, R. Moshhammer, U. Morgner, J. Ullrich and H. Roskos, "Determination of the carrier-envelope phase of few-cycle laser pulses with terahertz-emission spectroscopy", *Nature physics*, **2**, 327 (2006).
- [66] M. F. Kling, C. Siedschlag, A. J. Verhoef, J. I. Khan, M. Schultze, T. Uphues, Y. Ni, M. Uiberacker, M. Drescher, F. Krausz and M. J. J. Vrakking, "Control of Electron Localization in Molecular Dissociation", *Science*, **312**, 246 (2006).
- [67] E. Goulielmakis, Complete Characterization of Light Waves using Attosecond Pulses, Ph.D. thesis, LMU München (2005).
- [68] R. Kienberger, E. Goulielmakis, M. Uiberacker, A. Baltuska, V. Yakovlev, F. Bammer, A. Scrinzi, T. Westerwalbesloh, U. Kleineberg, U. Heinzmann, M. Drescher and F. Krausz, "Atomic transient recorder", *Nature*, **427**, 817 (2004).

- [69] E. Goulielmakis, M. Uiberacker, R. Kienberger, A. Baltuška, V. Yakovlev, A. Scrinzi, T. Westerwalbesloh, U. Kleineberg, U. Heinzmann, M. Drescher and F. Krausz, “Direct Measurement of Light Waves”, *Science*, **305**, 1267 (2004).
- [70] M. Uiberacker, T. Uphues, M. Schultze, A. J. Verhoef, V. Yakovlev, M. Kling, J. Rauschenberger, N. M. Kabachnik, H. Schröder, M. Lezius, M. Vrakking, S. Hendel, U. Kleineberg, U. Heinzmann, M. Drescher and F. Krausz, “Attosecond real-time observation of electron tunneling and multi-electron dynamics in atoms”, *Nature* (to appear on april 5, 2007).
- [71] M. Schätzel, F. Lindner, G. G. Paulus, H. Walther, E. Goulielmakis, A. Baltuška, M. Lezius and F. Krausz, “Long-term stabilization of the carrier-envelope phase of few-cycle laser pulses”, *Appl. Phys. B*, **79**, 1021 (2004).
- [72] A. J. Verhoef, A. Fernández, M. Lezius, K. O’Keeffe, M. Uiberacker and F. Krausz, “Few-cycle carrier envelope phase dependent stereo detection of electrons”, *Opt. Lett.*, **31**, 3520 (2006).
- [73] F. Verluise, V. Laude, Z. Cheng, C. Spielmann and P. Tournois, “Amplitude and phase control of ultrashort pulses by use of an acousto-optic programmable dispersive filter: pulse compression and shaping”, *Opt. Lett.*, **25**, 575 (2000).
- [74] R. Szipöcs, K. Ferencz, C. Spielmann and F. Krausz, “Chirped multilayer coatings for broadband dispersion control in femtosecond lasers”, *Opt. Lett.*, **19**, 201 (1994).
- [75] C. Rullière (editor), *Femtosecond Laser Pulses: Principles and Experiments* (Springer, New York, USA, 2005), second edition.
- [76] J. A. Squier, D. N. Fittinghoff, C. P. J. Barty, K. R. Wilson, M. Müller and G. J. Brakenhoff, “Characterization of femtosecond pulses focused with high numerical aperture optics using interferometric surface-third-harmonic generation”, *Opt. Commun.*, **147**, 153 (1998).
- [77] D. Meshulach, Y. Barad and Y. Silberberg, “Measurement of ultrashort optical pulses by third-harmonic generation”, *J. Opt. Soc. Am. B*, **14**, 2122 (1997).
- [78] S. Luan, M. H. R. Hutchinson, R. A. Smith and F. Zhou, “High dynamic range third-order correlation measurement of picosecond laser pulse shapes”, *Meas. Sci. Technol.*, **4**, 1426 (1993).
- [79] C. Iaconis and I. A. Walmsley, “Self-Referencing Spectral Interferometry for Measuring Ultrashort Optical Pulses”, *IEEE J. QE.*, **35**, 501 (1999).
- [80] R. Trebino, “FROG”, (), URL <http://www.physics.gatech.edu/gcuo/Tutorial/FROG.pdf>.
- [81] D. Kane and R. Trebino, “Characterization of Arbitrary Femtosecond Pulses Using Frequency-Resolved Optical Gating”, *IEEE J. QE.*, **29**, 571 (1993).
- [82] A. Baltuška, M. S. Pshenichnikov and D. A. Wiersma, “Amplitude and phase characterization of 4.5-fs pulses by frequency-resolved optical gating”, *Opt. Lett.*, **23**, 1474 (1998).



- [83] L. Veisz, Y. Nomura, K. Schmid, T. Wittmann and F. Krausz, "Plasma mirror with few-cycle laser pulses", in "CLEO/Europe-EQEC 2005", (2005), CG4-5-WED.
- [84] T. Udem, J. Reichert, R. Holzwarth and T. W. Hänsch, "Accurate measurement of large optical frequency differences with a mode-locked laser", *Opt. Lett.*, **24**, 881 (1999).
- [85] M. Zimmermann, C. Gohle, R. Holzwarth, T. Udem and T. W. Hänsch, "Optical clockwork with an offset-free difference-frequency comb: accuracy of sum- and difference-frequency generation", *Opt. Lett.*, **29**, 310 (2004).
- [86] C. Li, E. Moon and Z. Chang, "Carrier-envelope phase shift caused by variation of grating separation", *Opt. Lett.*, **31**, 3113 (2006).
- [87] D. B. Milošević, G. G. Paulus and W. Becker, "High-order above-threshold ionization with few-cycle pulse: a meter of the absolute phase", *Opt. Express*, **11**, 1418 (2003).
- [88] P. A. ad F. Fabre, G. Mainfray, G. Petite and N. K. Rahman, "Free-Free Transition Following Six-Photon Ionization of Xenon Atoms", *Phys. Rev. Lett.*, **42**, 1127 (1979).
- [89] P. B. Corkum, "Plasma Perspective on Strong-Field Multiphoton Ionization", *Phys. Rev. Lett.*, **71**, 1994 (1993).
- [90] S. Chelkowski, A. D. Bandrauk and A. Apolonski, "Measurement of the carrier-envelope phase of few-cycle laser pulses by use of asymmetric photoionisation", *Opt. Lett.*, **29**, 1557 (2004).
- [91] E. Seres, Ultraschnelle Zeitaufgelöste Absorptionsspektroskopie im Weichen Röntgenbereich, Ph.D. thesis, Universität Würzburg (2005).
- [92] T. Uphues, Assembly and Application of an Instrument for Attosecond-Time-Resolved Ionization Chronoscopy, Ph.D. thesis, Universität Bielefeld (2006).
- [93] C. Spielmann, N. H. Burnett, S. Sartania, R. Koppitsch, M. Schnürer, C. Kan, M. Lenzner, P. Wobrauschek and F. Krausz, "Generation of Coherent X-rays in the Water Window Using 5-Femtosecond Laser Pulses", *Science*, **278**, 661 (1997).
- [94] Z. Chang, A. Rundquist, H. Wang, M. M. Murnane and H. C. Kapteyn, "Generation of Coherent Soft X Rays at 2.7 nm Using High Harmonics", *Phys. Rev. Lett.*, **79**, 2967 (1997).
- [95] E. Seres, J. Seres, F. Krausz and C. Spielmann, "Generation of Coherent Soft-X-Ray Radiation Extending Far Beyond the Titanium L Edge", *Phys. Rev. Lett.*, **92**, 163002 (2004).
- [96] J. Seres, E. Seres, A. J. Verhoef, P. Wobrauschek, C. Streli, V. Yakovlev, C. Spielmann and F. Krausz, "Source of coherent kiloelectronvolt X-rays", *Nature*, **433**, 596 (2005).
- [97] F. Lindner, W. Stremme, M. G. Schätzel, F. Grasbon, G. G. Paulus, H. Walther, R. Hartmann and L. Strüder, "High-order harmonic generation at a repetition rate of 100 kHz", *Phys. Rev. A*, **68**, 013814 (2003).
- [98] R. J. Jones and J. Ye, "High-repetition-rate coherent femtosecond pulse amplification with an external passive optical cavity", *Opt. Lett.*, **29**, 2812 (2004).

- [99] K. D. Moll, R. J. Jones and J. Ye, “Nonlinear dynamics inside femtosecond enhancement cavities”, *Opt. Express*, **13**, 1672 (2005).
- [100] A. McPherson, G. Gibson, H. Jara, U. Johann, T. S. Luk, I. A. McIntyre, K. Boyer and C. K. Rhodes, “Studies of multiphoton production of vacuum-ultraviolet radiation in the rare gases”, *J. Opt. Soc. Am. B*, **4**, 595 (1987).
- [101] M. Lewenstein, P. Balcou, M. Y. Ivanov, A. L’Huillier and P. B. Corkum, “Theory of high harmonic generation by low-frequency laser fields”, *Phys. Rev. A*, **49**, 2117 (1994).
- [102] P. Salières, A. L’Huillier and M. Lewenstein, “Coherence Control of High-Order Harmonics”, *Phys. Rev. Lett.*, **74**, 3776 (1995).
- [103] E. Constant, D. Garzella, P. Breger, E. Mével, C. Dorrer, C. L. Blanc, F. Salin and P. Agostini, “Optimizing High Harmonic Generation in Absorbing Gases: Model and Experiment”, *Phys. Rev. Lett.*, **82**, 1668 (1999).
- [104] P. Balcou, A. S. Dederichs, M. B. Gaarde and A. L’Huillier, “Quantum-path analysis and phase matching of high-order harmonic generation and high-order frequency mixing processes in strong laser fields”, *J. Phys. B*, **32**, 2973 (1999).
- [105] G. Tempea, M. Geissler and T. Brabec, “Phase sensitivity of high-order harmonic generation with few-cycle laser pulses”, *J. Opt. Soc. Am. B*, **16**, 669 (1999).
- [106] A. Scrinzi, M. Geissler and T. Brabec, “Ionization Above the Coulomb Barrier”, *Phys. Rev. Lett.*, **83**, 706 (1999).
- [107] A. Gordon and F. X. Kärtner, “Scaling of keV HHG photon yield with drive wavelength”, *Opt. Express*, **13**, 2941 (2005).
- [108] M. Schnürer, Z. Cheng, M. Hentschel, G. Tempea, P. Kálmán, T. Brabec and F. Krausz, “Absorption-Limited Generation of Coherent Ultrashort Soft-X-Ray Pulses”, *Phys. Rev. Lett.*, **83**, 722 (1999).
- [109] P. Salières, T. Ditmire, M. D. Perry, A. L’Huillier and M. Lewenstein, “Angular distributions of high-order harmonics generated by a femtosecond laser”, *J. Phys. B*, **29**, 4771 (1996).
- [110] P. Salières, T. Ditmire, K. S. Budil, M. D. Perry and A. L’Huillier, “Spatial profiles of high-order harmonics generated by a femtosecond Cr:LiSAF laser”, *J. Phys. B*, **27**, L217 (1994).
- [111] “Center for x-ray optics – Filter transmission”, (), URL [http://www-cxro.lbl.gov/optical\\_constants/filter2.html](http://www-cxro.lbl.gov/optical_constants/filter2.html).
- [112] M. Drescher, M. Hentschel, R. Kienberger, G. Tempea, C. Spielmann, G. A. Reider, P. B. Corkum and F. Krausz, “X-ray Pulses Approaching the Attosecond Frontier”, *Science*, **291**, 1923 (2001).
- [113] M. Hentschel, R. Kienberger, C. Spielmann, G. A. Reider, N. Milosevic, T. Brabec, P. B. Corkum, U. Heinzmann, M. Drescher and F. Krausz, “Attosecond metrology”, *Nature*, **414**, 509 (2001).

- [114] J. J. Macklin, J. D. Kmetec and C. L. Gordon III, “High-Order Harmonic Generation Using Intense Femtosecond Pulses”, *Phys. Rev. Lett.*, **70**, 766 (1993).
- [115] A. L’Huillier and P. Balcou, “High-Order Harmonic Generation in Rare Gases with a 1-ps 1053-nm Laser”, *Phys. Rev. Lett.*, **70**, 774 (1993).
- [116] “Center for x-ray optics – Multilayer coatings – a mini-tutorial”, (), URL <http://www-cxro.lbl.gov/multilayer/mltutor.html>.
- [117] L. Dreeskornfeld, G. Haindl, U. Kleineberg, U. Heinzmann, F. Shi, B. Volland, I. Rangelow, E. Majkova, S. Luby, Kostic, L. Matay, P. Hrkut, P. Hudek and H. Lee, “Nanostructuring of mo/si multilayers by means of reactive ion etching using a three-level mask”, *thin solid films*, **458**, 227 (2004).
- [118] S. Bajt, J. A. Folta, E. A. Spiller, R. Grabner, J. B. Alameda and B. B. Kaufmann, “Improved reflectance and stability of Mo/Si multilayers”, in “SPIE’s 46th Annual Meeting – International Symposium on Optical Science and Technology”, (2001), 4506-12.
- [119] “Center for x-ray optics – Multilayer reflectivity”, (), URL [http://www-cxro.lbl.gov/optical\\_constants/multi2.html](http://www-cxro.lbl.gov/optical_constants/multi2.html).
- [120] S. P. Shannon, K. Codling and J. B. West, “The absolute photoionization cross sections of the spin-orbit components of the xenon 4d electron from 70–130 eV”, *J. Phys. B*, **10**, 825 (1977).
- [121] U. Becker, D. Szotak, H. G. Kerkhoff, M. Kupsch, B. Langer, R. Wehlitz, A. Yagishita and T. Hayaishi, “Subshell photoionization of Xe between 40 and 1000 eV”, *Phys. Rev. A*, **39**, 3902 (1989).
- [122] A. Kikas, S. J. Osborne, A. Ausmees, S. Svensson, O. P. Sairanen and S. Aksela, “High-resolution study of the correlation satellites in photoelectron spectra of the rare gases”, *J. El. Spec. Rel. Phen.*, **77**, 241 (1996).
- [123] D. M. P. Holland, K. Codling, J. B. West and G. V. Marr, “Multiple photoionisation in the rare gases from threshold to 280 eV”, *J. Phys. B*, **12**, 2465 (1979).
- [124] T. Hayaishi, E. Murakami, Y. Morioka, H. Aksela, S. Aksela, E. Shigemasa and A. Yagishita, “Manifestation of Kr 3d and Xe 4d conjugate shake-up satellites in threshold-electron spectra”, *Phys. Rev. A*, **44**, R2771 (1991).
- [125] B. Kämmerling, B. Krässig and V. Schmidt, “Direct measurement for the decay probabilities of 4d<sub>j</sub> hole states in xenon by means of photoelectron-ion coincidences”, *J. Phys. B*, **25**, 3621 (1992).
- [126] P. Lablanquie, S. Sheinerman, F. Penent, R. I. Hall, M. Ahmad, T. Aoto, Y. Hikosaka and K. Ito, “Photoemission of threshold electrons in the vicinity of the xenon 4d hole: dynamics of Auger decay”, *J. Phys. B*, **35**, 3265 (2002).
- [127] J. Viefhaus, M. Braune, S. Korica, A. Reinköster, D. Rolles and U. Becker, “Auger cascades versus direct double Auger: relaxation processes following photoionization of the Kr 3d and Xe 4d, 3d inner shells”, *J. Phys. B*, **38**, 3885 (2005).

- [128] F. Penent, J. Palaudoux, P. Lablanquie, L. Andric, R. Feifel and J. H. D. Eland, "Multielectron Spectroscopy: The Xenon  $4d$  Hole Double Auger Decay", *Phys. Rev. Lett.*, **95**, 083002 (2005).
- [129] M. Drescher, M. Hentschel, R. Kienberger, M. Uiberacker, V. Yakovlev, A. Scrinzi, T. Westerwalbesloh, U. Kleineberg, U. Heinzmann and F. Krausz, "Time-resolved atomic inner-shell spectroscopy", *Nature*, **419**, 803 (2002).
- [130] H. Schröder, M. Wagner, S. Kaesdorf and K. L. Kompa, "Surface-analysis by laser ionization", *Ber. Bunsen. Phys. Chem.*, **97**, 1688 (1993).
- [131] M. Wagner and H. Schröder, "A novel 4 grid ion reflector for saturation of laser multiphoton ionization yields in a time-of-flight mass-spectrometer", *Int. J. Mass Spectrom.*, **128**, 31 (1993).
- [132] B. Witzel, H. Schröder, S. Kaesdorf and K. L. Kompa, "Exact determination of spatially resolved ion concentrations in focused laser beams", *Int. J. Mass Spectrom. Ion Proc.*, **172**, 229 (1998).
- [133] Y. Ni, From Strong Field Ionization to the Generation of Attosecond Laser Pulses, Ph.D. thesis, Radboud Universiteit Nijmegen (2006).
- [134] H. Helm, N. Bjerre, M. J. Dyer, D. L. Huestis and M. Saeed, "Images of Photoelectrons Formed in Intense Laser Fields", *Phys. Rev. Lett.*, **70**, 3221 (1993).
- [135] H. Helm and M. J. Dyer, "Resonant and nonresonant multiphoton ionization of helium", *Phys. Rev. A*, **49**, 2726 (1994).
- [136] A. J. R. Heck and D. W. Chandler, "Imaging techniques for the study of chemical reaction dynamics", *Annu. Rev. Phys. Chem.*, **46**, 335 (1995).
- [137] A. T. J. B. Eppink and D. H. Parker, "Velocity map imaging of ions and electrons using electrostatic lenses: Application in photoelectron and photofragment ion imaging of molecular oxygen", *Rev. Sci. Instr.*, **68**, 3477 (1997).
- [138] M. J. J. Vrakking, "An iterative procedure for the inversion of two-dimensional ion/photoelectron imaging experiments", *Rev. Sci. Instr.*, **72**, 4084 (2001).
- [139] V. Schyja, T. Lang and H. Helm, "Channel switching in above-threshold ionization of xenon", *Phys. Rev. A*, **57**, 3692 (1998).
- [140] M. J. Nandor, M. A. Walker and L. D. van Woerkom, "Angular distributions of high-intensity ATI and the onset of the plateau", *J. Phys. B*, **31**, 4617 (1998).
- [141] B. Yang, K. J. Schafer, B. Walker, K. C. Kulander, P. Agostini and L. F. DiMauro, "Intensity-Dependent Scattering Rings in High Order Above-Threshold Ionization", *Phys. Rev. Lett.*, **71**, 3770 (1993).
- [142] J. H. Posthumus, "The dynamics of small molecules in intense laser fields", *Rep. Prog. Phys.*, **67**, 623 (2004).
- [143] A. D. Bandrauk, S. Chelkowski and H. S. Nguyen, "Attosecond Localization of Electrons in Molecules", *Int. J. Quant. Chem.*, **100**, 834 (2004).

- [144] V. Roudnev, B. D. Esry and I. Ben-Itzhak, "Controlling  $\text{HD}^+$  and  $\text{H}_2^+$  Dissociation with the Carrier-Envelope Phase Difference of an Intense Ultrashort Laser Pulse", *Phys. Rev. Lett.*, **93**, 163601 (2004).
- [145] H. Niikura, D. M. Villeneuve and P. B. Corkum, "Controlling vibrational wave packets with intense, few-cycle laser pulses", *Phys. Rev. A*, **73**, 021402 (2006).
- [146] P. H. Bucksbaum, A. Zavriyev, H. G. Muller and D. W. Schumacher, "Softening of the  $\text{H}_2^+$  Molecular Bond in Intense Laser Fields", *Phys. Rev. Lett.*, **64**, 1883 (1990).
- [147] A. S. Alnaser, T. Osipov, E. P. Benis, A. Wech, B. Shan, C. L. Cocke, X. M. Tong and C. D. Lin, "Rescattering Double Ionization of  $\text{D}_2$  and  $\text{H}_2$  by intense Laser Pulses", *Phys. Rev. Lett.*, **91**, 163002 (2003).
- [148] A. S. Alnaser, X. M. Tong, T. Osipov, S. Voss, C. M. Maharjan, P. Ranitovic, B. Ulrich, B. Shan, Z. Chang, C. D. Lin and C. L. Cocke, "Routes to Control of  $\text{H}_2$  Coulomb Explosion in Few-Cycle Laser Pulses", *Phys. Rev. Lett.*, **93**, 183202 (2004).
- [149] H. Sakai, J. J. Larsen, I. Wendt-Larsen, J. Olesen, P. B. Corkum and H. Stapelfeldt, "Nonsequential double ionization of  $\text{D}_2$  molecules with intense 20-fs pulses", *Phys. Rev. A*, **67**, 063404 (2003).
- [150] K. Sändig, H. Figger and T. W. Hänsch, "Dissociation Dynamics of  $\text{H}_2^+$  in Intense Laser Fields: Investigation of Photofragments from Single Vibrational Levels", *Phys. Rev. Lett.*, **85**, 4876 (2000).
- [151] I. Kawata, H. Kono and Y. Fujimura, "Adiabatic and diabatic responses of  $\text{H}_2^+$  to an intense femtosecond laser pulse: Dynamics of the electronic and nuclear wave packet", *J. Chem. Phys.*, **110**, 11152 (1999).
- [152] H. Niikura, F. Légaré, R. Hasbani, A. D. Bandrauk, M. Y. Ivanov, D. M. Villeneuve and P. B. Corkum, "Sub-laser-cycle electron pulses for probing molecular dynamics", *Nature*, **417**, 917 (2002).
- [153] G. L. Yudin, S. Chelkowski, J. Itatani, A. D. Bandrauk and P. B. Corkum, "Attosecond photoionization of coherently coupled electronic states", *Phys. Rev. A*, **72**, 051401 (2005).
- [154] F. H. M. Faisal, "Multiple absorption of laser photons by atoms", *J. Phys. B*, **6**, L89 (1973).
- [155] F. Grasbon, G. G. Paulus, H. Walther, P. Villoresi, G. Sansone, S. Stagira, M. Nisoli and S. D. Silvestri, "Above-Threshold Ionization at the Few-Cycle Limit", *Phys. Rev. Lett.*, **91**, 173003 (2003).
- [156] P. Krause, T. Klamroth and P. Saalfrank, "Time-dependent configuration-interaction calculations of laser-pulse-driven many-electron dynamics: Controlled dipole switching in lithium cyanide", *J. Chem. Phys.*, **123**, 074105 (2005).
- [157] F. P. Larkins, "Charge state dependence of x-ray and Auger electron emission spectra for rare-gas atoms; II. The neon atom", *J. Phys. B*, **4**, 14 (1971).

- [158] Y. Mairesse, A. de Bohan, L. J. Frasinski, H. Herdji, L. C. Dinu, P. Monchicourt, P. Breger, M. Kovačev, R. Taïeb, B. Carré, H. G. Muller, P. Agostini and P. Salières, “Attosecond Synchronisation of High-Harmonic Soft X-rays”, *Science*, **302**, 1540 (2003).
- [159] H. Niikura, F. Légaré, R. Hasbani, M. Y. Ivanov, D. M. Villeneuve and P. B. Corkum, “Probing molecular dynamics with attosecond resolution using correlated wave packet pairs”, *Nature*, **421**, 826 (2003).
- [160] H. Niikura, D. M. Villeneuve and P. B. Corkum, “Mapping Attosecond Electron Wave Packet Motion”, *Phys. Rev. Lett.*, **94**, 083003 (2005).
- [161] P. M. Paul, E. S. Toma, P. Breger, G. Mullot, F. Augé, P. Balcou, H. G. Muller and P. Agostini, “Observation of a Train of Attosecond Pulses from High Harmonic Generation”, *Science*, **292**, 1689 (2001).
- [162] T. Shimizu, T. Sekikawa, T. Kanai, S. Watanabe and M. Itoh, “Time-resolved Auger Decay in CsBr Using High Harmonics”, *Phys. Rev. Lett.*, **91**, 017401 (2003).
- [163] O. Smirnova, M. Spanner and M. Ivanov, “Coulomb and polarization effects in sub-cycle dynamics of strong-field ionization”, *J. Phys. B*, **39**, S307 (2006).
- [164] S. Svensson, B. Eriksson, N. Mørtensson, G. Wendin and U. Gelius, “Electron shake-up and correlation satellites and continuum shake-off distributions in x-ray photoelectron spectra of the rare gas atoms”, *J. El. Spec. Rel. Phen.*, **47**, 327 (1988).
- [165] B. Walker, B. Sheehy, L. F. DiMauro, P. Agostini, K. J. Schafer and K. C. Kulander, “Precision Measurement of Strong Field Double Ionization of Helium”, *Phys. Rev. Lett.*, **73**, 1227 (1994).

# Curriculum Vitae

November 27, 2006

## Current address

Institut für Photonik,  
Technische Universität Wien  
Gußhausstraße 27/387  
1040 Wien  
Austria  
tel: +43 1 58801 38778  
fax: +43 1 58801 38799

## Personalialia

Full name	Aart Johannes Verhoef
Date of birth	December 9, 1979
Place of birth	Amsterdam, the Netherlands
Nationality	Nederlands (Dutch)
Gender	Male
Civil status	Married to Alma Fernández

## Degree

M.Sc. degree received from Vrije Universiteit Amsterdam in 2002.  
Diploma thesis entitled 'Speccs Software Documentation', written at the section for Atomic Physics at the Laser Centre at the Vrije Universiteit Amsterdam.

## Education

2004–now	Continuation of Ph.D. Studies at MPQ Garching Expected thesis defense July 2006
2002–2004	Ph.D. Studies at TU Vienna, Photonics Institute
1998–2002	Study Physics and Astronomy at VU Amsterdam
1992–1998	Secondary school

## **Scientific interests**

Generation and amplification of ultrashort pulses  
Measurement and control of the absolute phase of few-cycle pulses  
Attosecond pulse generation  
Sub-femtosecond time resolved spectroscopy  
High resolution frequency resolved spectroscopy  
Single atom/ion spectroscopy  
Molecular dynamics

## **Hobbies**

Football, biking, sailing, cooking.

## **Language knowledge**

Dutch (native); English, German (fluent); French (basic).